FACULTÉ DES ÉTUDES SUPÉRIEURES ET POSTOCTORALES

uOttawa

L'Université canadienne
Canada's university

FACULTY OF GRADUATE AND POSDOCTORAL STUDIES

Tan Quach

AUTEUR DE LA THÈSE / AUTHOR OF THESIS

M.A.Sc. (Electrical Engineering)

GRADE / DEGREE

School of Information Technology and Engineering

FACULTÉ, ÉCOLE, DÉPARTEMENT / FACULTY, SCHOOL, DEPARTMENT

Holographic Antennas Realized From Interference Patterns Determined in the Presence of the Dielectric Substrate

TITRE DE LA THÈSE / TITLE OF THESIS

D. McNamara

DIRECTEUR (DIRECTRICE) DE LA THÈSE / THESIS SUPERVISOR

A. Petosa

CO-DIRECTEUR (CO-DIRECTRICE) DE LA THÈSE / THESIS CO-SUPERVISOR

EXAMINATEURS (EXAMINATRICES) DE LA THÈSE / THESIS EXAMINERS

Jafar Shaker

Mustapha Yagoub

Gary W. Slater

LE DOYEN DE LA FACULTÉ DES ÉTUDES SUPÉRIEURES ET POSTDOCTORALES /
DEAN OF THE FACULTY OF GRADUATE AND POSTDOCORAL STUDIES

Holographic Antennas Realized From Interference Patterns Determined in the Presence of the Dielectric Substrate

Tan Quach

A thesis submitted to the
Faculty of Graduate and Postdoctoral Studies
in partial fulfillment of the requirements for the degree of

Master of Applied Science
in Electrical Engineering

Ottawa-Carleton Institute for Electrical and Computer Engineering
School of Information Technology and Engineering
University of Ottawa

Your file Votre référence
ISBN: 0-494-14941-8
Our file Notre référence
ISBN: 0-494-14941-8

In loving memory of my mother

Abstract

Holographic antennas are attractive due to their low-profile and potentially high gain. These antennas are synthesized from the interference pattern of a reference wave and a plane wave. The reference wave is generated by the feed antenna and the plane wave is used to represent an ideal antenna's wavefront in the far-zone. At millimeter-wave frequencies, using printed circuit technology to fabricate the hologram requires the use of an approximated form of the interference pattern. The hologram is realized by etching metallic strips at the pattern's minima on a dielectric substrate. The strips are used to "record" the minima of the interference pattern since the tangential electric field is forced to zero there.

Previous works have addressed other issues while using the free-space interference pattern to realize the binary hologram. The objective of this thesis is to investigate the effects of the realistic source and the presence of the dielectric substrate on the interference pattern. The new patterns could provide insights as to where the strips should be placed with respect to the feed, and the required curvature of the strips.

Since the hologram is electrically large, it was first studied in two-dimensions (2-D) and then in three-dimensions (3-D) where the true large substrate was approximated with a substrate that is infinite in the lateral plane. In 2-D, it was possible to study the effect of the finite length substrate on the interference pattern along with the realistic feed horn source. The presence of the finite substrate caused a double-minima behaviour in the interference pattern and was utilized to achieve high directivity. Applying this approach to synthesize the double-sided hologram showed significant improvements compared to the double-sided holograms in previous works. The true 3-D interference pattern involving the large finite substrate cannot be computed due to current computational limitations. A prototype hologram was fabricated based on the approximate 3-D interference pattern of an infinite substrate. Experimental validation confirmed the design procedure and showed a 1dB improvement compared to the printed-dipole-fed hologram. Additionally, the new hologram has more leftover power which will enable the use of larger holograms to increase the gain.

Acknowledgements

I am very grateful for the enthusiastic guidance and support of my supervisors Dr. Derek McNamara and Dr. Aldo Petosa throughout the course of this study. I have enjoyed working with them and their insights have been invaluable.

I would like to thank Mr. Michel Cuhaci and the Communications Research Centre (CRC) for the use of the CRC fabrication & measurement facilities, and partial financial support. Partial financial support was also obtained through my supervisor's NSERC grant. Thanks to Mr. Soulideth Thirakoune for his help with the measurement process. And finally, I am thankful to my family and friends, particularly my brother Le and his wife Lan, for their support and encouragement.

Publications

T. Quach, D.A. McNamara, and A. Petosa, 2005, "Holographic Antenna Realised Using Interference Patterns Determined in Presence of Dielectric Substrate", *IEE Electronic Letters*, Volume 41, pp. 724-725

T. Quach, D.A. McNamara, and A. Petosa, 2005, "Improved Holographic Antenna Using Interference Patterns Determined in the Presence Of the Intended Substrate", presented at *IEEE Antennas and Propagation Symposium*, Washington, D.C, July 2005

Contents

List of Figures

List of Tables

List of Symbols & Acronyms

α	Attenuation constant
$\alpha(x)$	Leakage rate or radiation rate
β_d	Phase constant in the dielectric substrate
β_n	Phase constant of n-th element in antenna array
β_o	Phase constant in the free-space
Γ_{in}	Input reflection coefficient
Γ_L	Reflection coefficient at the load
ε_o	Relative permittivity of free-space
ε_r	Relative permittivity or dielectric constant
η	Intrinsic impedance of the dielectric substrate
η_o	Intrinsic impedance of free-space
λ_o	Free-space wavelength
λ_g	Guided wavelength
μ_o	Permeability of free-space
ρ	Observation point in cylindrical coordinates
$\underline{\rho}_{LS}$	Location of line source in cylindrical coordinates
$\underline{\rho}'$	Segment coordinates on the substrate and horn surfaces
ω	Angular frequency
A	Amplitude of the reference wave
A_n	Amplitude of the n-th element in antenna array
A(x)	Aperture distribution
AF	Array Factor
Area	Area of antenna aperture
arg	Argument

B	Amplitude of the object wave or plane wave
c	Speed of light
D	Directivity
$D_{endfire}$	Directivity in the endfire direction
$D_{uniform}$	Directivity of uniformly illuminated aperture
E_z	z-component of electric field
E_z^{ap}	Electric field over aperture region (z-component)
$\underline{E}_{obj}$	Total electric field due to object wave
$\underline{E}_{ref}$	Total electric field due to reference wave
E_z^{ext}	Electric field external to dielectric substrate (z-component)
E_z^{inc}	Incident electric field (z-component)
E_z^{int}	Electric field internal to dielectric substrate (z-component)
$\underline{E}_{tot}^{PW}$	Total electric field due to plane wave source (z-component)
E_z^{scat}	Scattered electric field (z-component)
e_{ap}	Aperture efficiency
e_{rad}	Radiation efficiency
e_{tot}	Total efficiency
F	2-D angular spectrum
f	Frequency
f_c	Cutoff frequency
f_o	Design frequency
f_p	Leftover power ratio
$\hat{f}$	Internal equivalent current
G	Gain
$\hat{g}$	External equivalent current
H_y	Total magnetic field (y-component)

H_y^{ext}	Magnetic field external to dielectric substrate (y-component)
H_y^{inc}	Incident magnetic field (y-component)
H_y^{int}	Magnetic field internal to dielectric substrate (y-component)
$H_o^{(2)}(\ )$	Hankel function of second kind and zero order
$H_1^{(2)}(\ )$	Hankel function of second kind and first order
I	Interference pattern
k_o	Free-space wavenumber
L	Length of dielectric substrate
O	Offset distance between the strip on top and bottom side of the substrate
P_{in}	Input power
P_{load}	Power at the load
P_{rad}	Radiated power
R	Observation point
RL	Return loss
$\underline{S}_{ave}$	Power density
$S_{ave,x}$	x-component of power density
SWR	Standing Wave Ratio
s	Separation distance between the strips
TM_z	Transverse Magnetic with respect to z-axis
t	Thickness of dielectric substrate
w	Width of conducting strip
x_{LS}	x coordinate of line source
y_{LS}	y coordinate of line source
Z_d	Characteristic impedance of the dielectric substrate
Z_{in}	Input impedance
Z_o	Characteristic impedance
z_n	Distance of n-th element in antenna array

Chapter 1 - Introduction

1.1 Introduction to Holographic Antennas

Holography is a process of recording and reconstructing monochromatic wavefronts. As illustrated in Figure 1.1, a hologram is a recording of the interference pattern of a reference wave with an object wave on a surface [1]. The object wave can be reconstructed by illuminating the hologram with the reference wave, and vice versa.

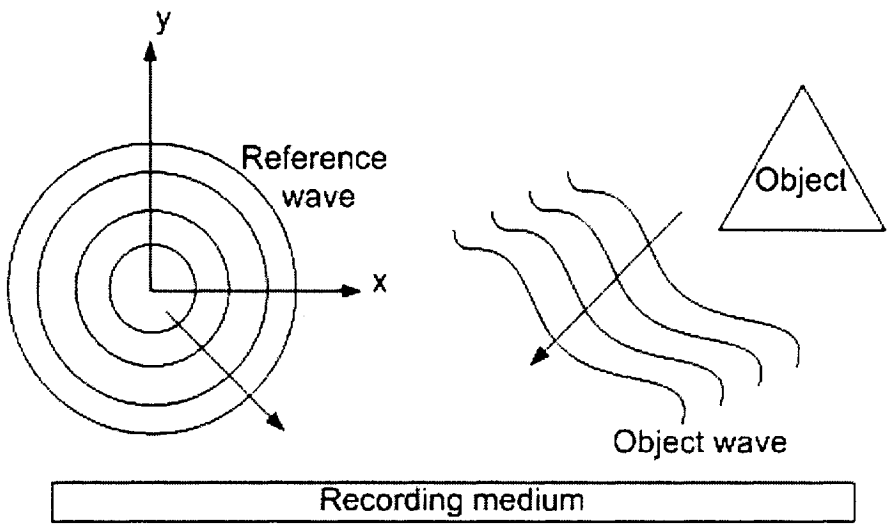

Figure 1.1- Recording stage in holography

In an idealized antenna model, the wavefront near the antenna source is assumed to be spherical and planar in the far-zone. Applying holographic principles to synthesize an antenna involves constructing the interference pattern of a spherical reference wave with a planar object wave. Then a planar wavefront, i.e. radiation pattern, is formed by illuminating the hologram with the reference source. The interference pattern is the magnitude of the phasor sum of the reference wave and object wave, and is given by

$$I(x, y_o, z) = \left|\underline{E}_{total}(x, y_o, z)\right| = \left|\underline{E}_{reference}(x, y_o, z) + \underline{E}_{object}(x, y_o, z)\right| \quad (1.1)$$

In this thesis we will only consider broadside radiation since it is commonly used in practice, so the plane wave will be normally incident on the recording surface. The interference

pattern of a spherical reference wave, designated at the origin, with a normally incident planar object wave in free-space observed at y_o is

$$I(x, y_o, z) = \left| \frac{A}{R} e^{-jk_o R} + B e^{jk_o y_o} \right| \tag{1.2}$$

where $k_o = \omega\sqrt{\mu_o \varepsilon_o}$, $R = \sqrt{x^2 + y_o^2 + z^2}$, and $B = A$. This interference pattern (or fringe pattern) is shown in Figure 1.2, where the light circular concentric rings are the maxima of the fringe pattern, and the dark concentric rings are the minima. At optical frequencies the continuous variation in the fringe pattern can be captured by photographic films, but at millimeter-wave frequencies we have to use a quantized and approximated form of the interference pattern if we wish to use printed circuit technology that consists of conducting strips etched on a dielectric substrate. The conducting strips are used to "record" the minima of the pattern since the tangential electric field is forced to zero at a conducting surface, while the regions that do not contain the conducting strips represent the rest of the variation in the pattern. Thus the millimeter-wave hologram is a binary hologram.

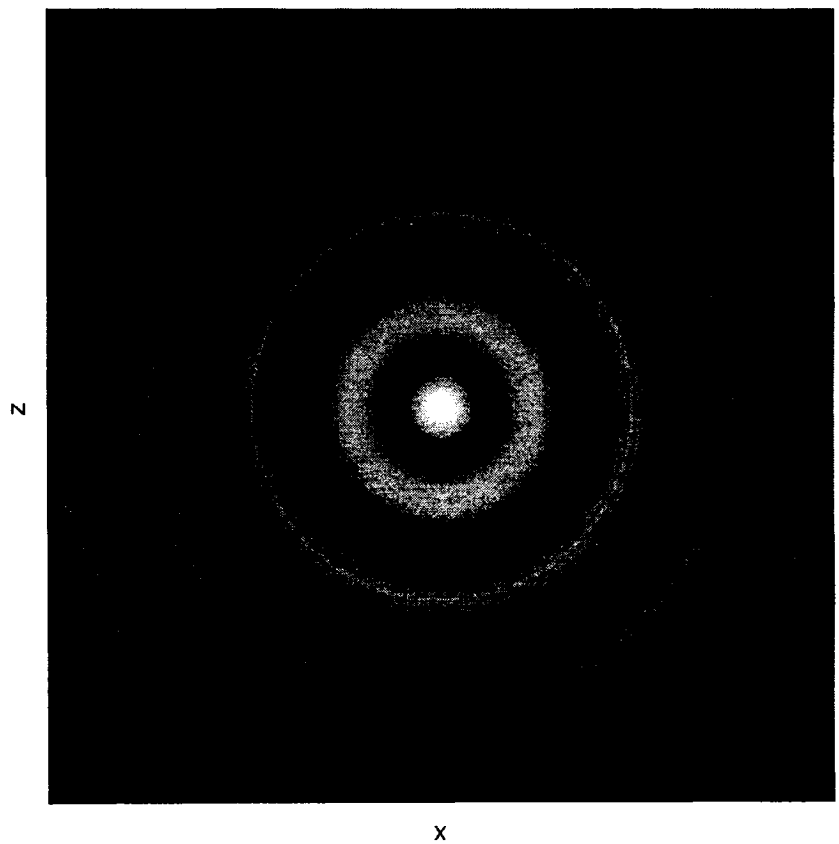

Figure 1.2 - Interference pattern of spherical wave with normally incident plane wave in free-space

The distance between the minima in the free-space interference pattern is not exactly periodic, but as a first approximation in the previous works of [2-7] it was set to be periodic with a period of one free-space wavelength, λ_o. To fabricate the binary hologram, circular metallic strips are printed periodically on a dielectric substrate, as illustrated in Figure 1.3. The hologram is fed by a horn antenna and will be referred to as the "free-space hologram" for its use of the periodic spacing distance between the strips. The inherent nature of the circular strips will support both horizontal and vertical components as depicted in Figure 1.4. Therefore to excite mainly the horizontal component and improve the cross-polarization level the dielectric substrate was selected to be a diamond shape substrate [2, 3].

With the feed horn positioned in the same plane as the hologram, the whole antenna has a low-profile compared to electrically large antennas such as reflectors, reflectarrays, and lens antennas. Furthermore, a flat-profile can be achieved by using a printed-source to feed the hologram [7]. Recent interests in holographic antennas have risen owing to the antennas' potential high gain, simpler design procedure, and low-profile. The low-profile provides aesthetics appeal while facilitating covert operations and other applications that require a low-profile in the millimeter-wave region. And the use of printed circuit technology will enable low-cost mass production of the light-weight holograms. Although microstrip phased arrays have low-profiles, they suffer from high feed losses in the millimeter-wave region and in large arrays [3, 21]. The study in [21] demonstrated that the performance of microstrip arrays will start to be worse than that of a reflector for the same aperture size and with an aperture efficiency of 50% when the array size increases from roughly $10\lambda_o$ x $10\lambda_o$. The degradation is due to the increasing spurious radiation loss, surface wave loss, dielectric loss, and conductor loss with the increasing array size. Although the binary hologram consists of long metallic strips printed on a dielectric substrate we conjecture that its conductive loss is less than that of the microstrip array since the hologram only uses strips instead of microstrip lines (which have the strips and large ground plane). Also, the radiating aperture is fed spatially instead of by constrained microstrip feed lines. Hence, one of the interests in holographic antennas is to produce comparable or better gain to microstrip arrays of the same aperture size.

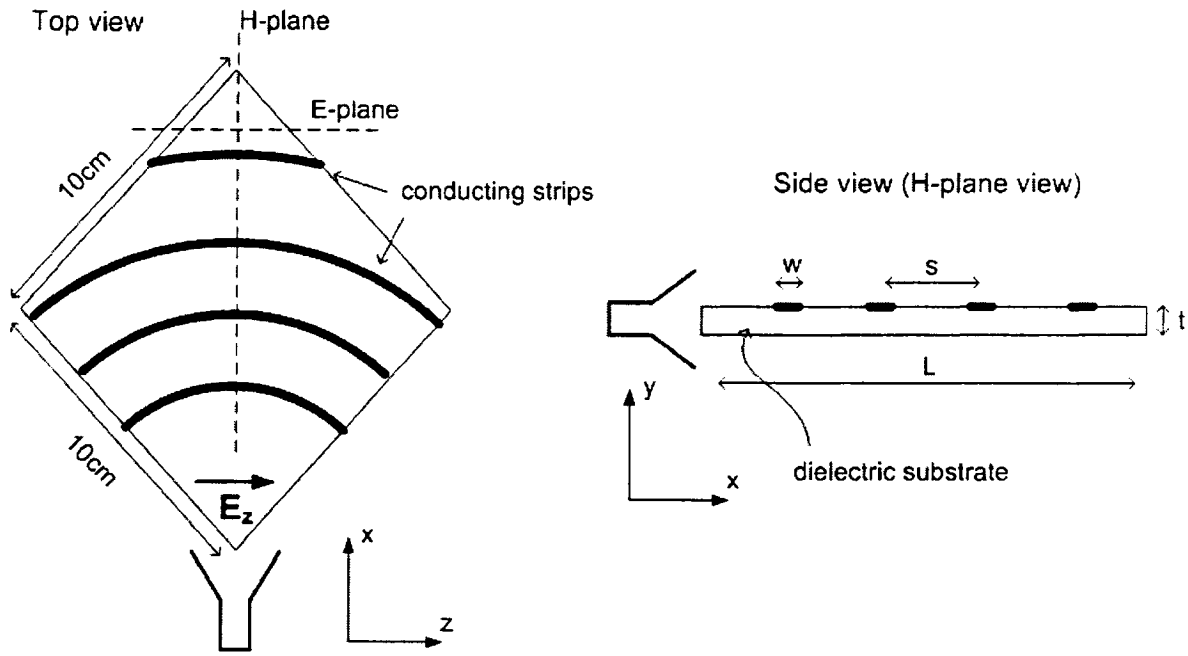

Figure 1.3 - Top view and side view of the holographic antenna

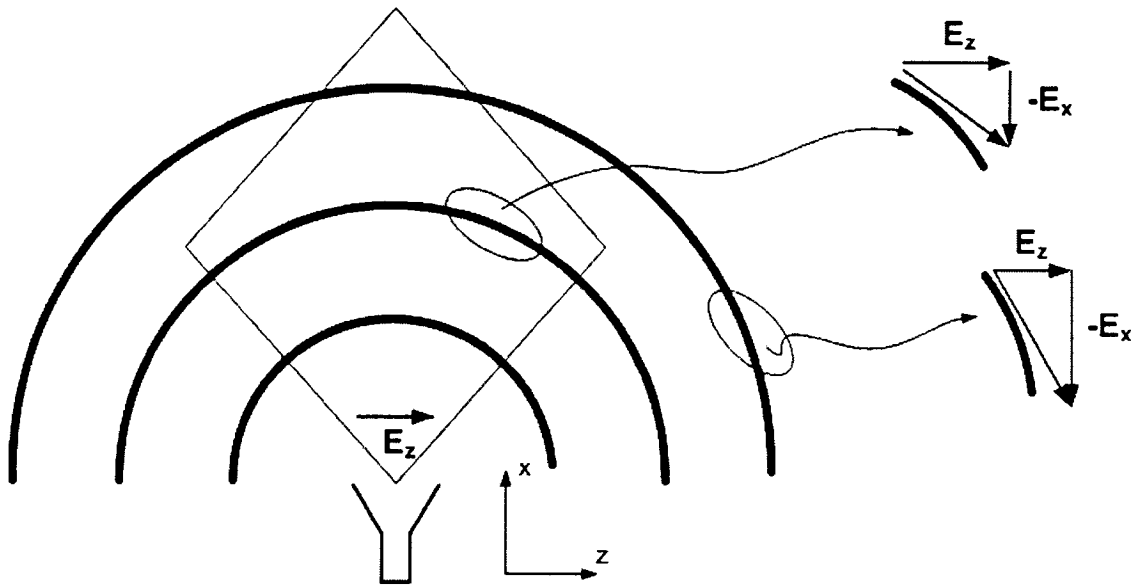

Figure 1.4 - Polarization decomposition of field components supported the circular strips

A disadvantage with the single-sided hologram in Figure 1.3 is that undesired beams will form along with the desired broadside beam. The beam formation upon reconstruction is illustrated in Figure 1.5 where the top and bottom broadside beams are the real and virtual images of the object formed upon reconstruction in optical holography. The undesired beams are due to the inherent nature of thin holograms [1]. Single beam operation is required in

most applications and we cannot simply place a ground plane on the bottom side of the free-space hologram to suppress the bottom broadside beam because the free-space interference pattern cannot account for the effect of the ground plane.

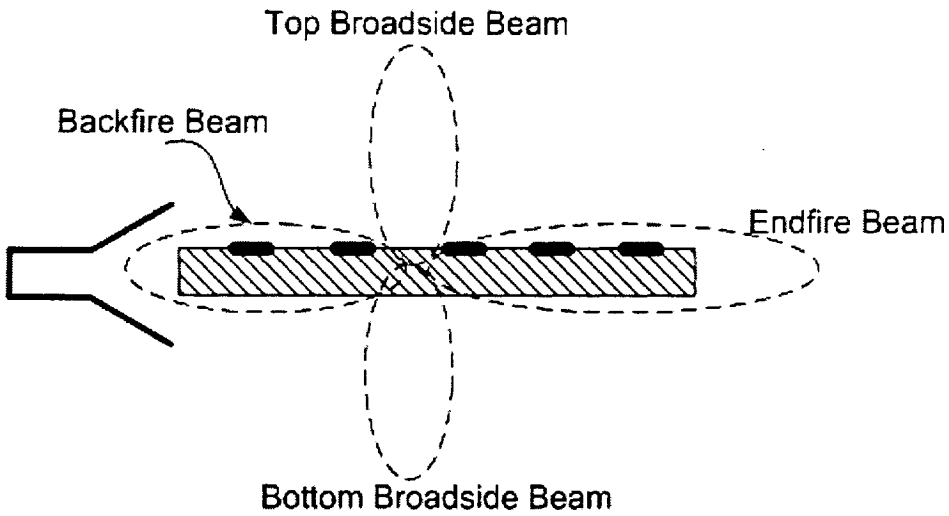

Figure 1.5 - Beams formation upon reconstruction in broadside hologram

1.1.1 Double-Sided Hologram and Double-Layer Hologram

To produce a single beam antenna we use the double-sided and double-layer holograms. As illustrated in Figure 1.6, both holograms are arrays of single-sided holograms with the top set of strips spaced at one quarter guided wavelength, $\lambda_g/4$, from the bottom strips in the vertical and horizontal directions. This will create a 180° phase difference in the bottom broadside and backfire directions to cancel out the unwanted beams. Meanwhile, the beams in the top broadside and endfire directions will be in-phase and add constructively to increase the directivity [2-4]. The double-layer hologram is more flexible than the double-sided hologram as it allows manual fine tuning to achieve the correct phase shift. However, we will only consider the double-sided hologram because it is more compact and easier to fabricate. Previous studies in [3, 5] have demonstrated comparable efficiency of the double-sided holograms to microstrip arrays.

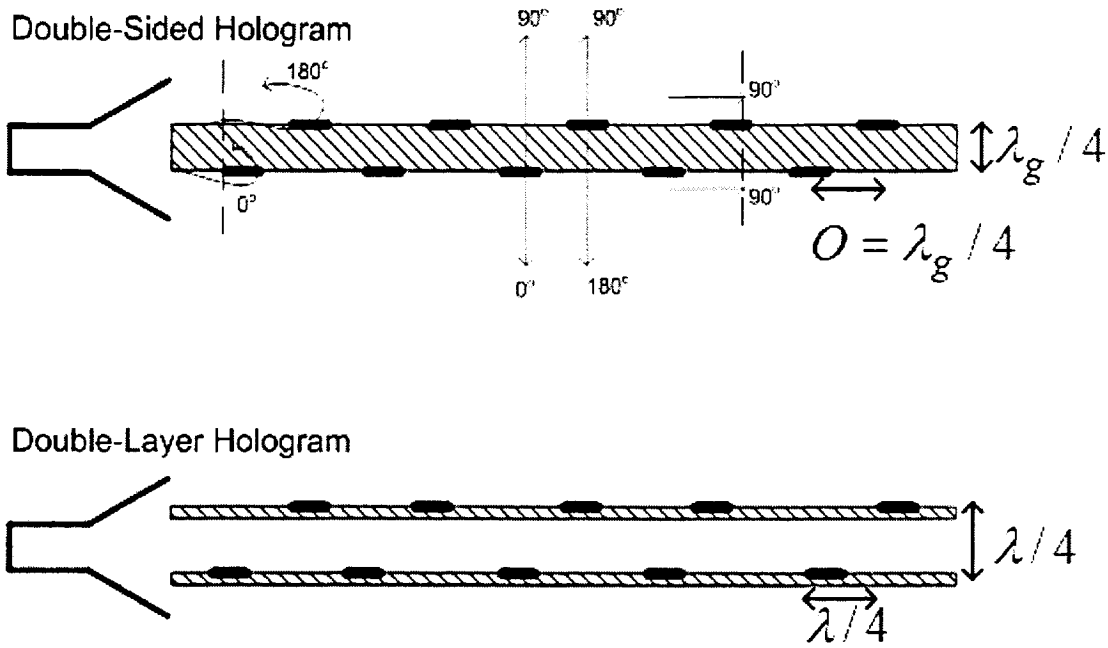

Figure 1.6 - Double-sided hologram and double-layer hologram

1.1.2 Dipole Hologram

The continuous strips in the holograms in Figures 1.3 and 1.6 will always support both horizontal and vertical field components. Better cross-polarization level can be achieved by etching $\lambda/2$ dipoles along the circular arc of the strips, as depicted in Figure 1.7, instead of the continuous strips because the dipoles will only support polarized waves that are parallel to their lengths [2-4]. Therefore the substrate does not have to be in a diamond shape slab but a diamond shape was used to have direct comparisons with the continuous-strip hologram [3, 4]. The dipole hologram achieved better cross-polarization performance but had a decrease in gain due to phase errors since the dipoles were etched along the curves of the interference pattern minima instead being exactly on those curves [3, 4].

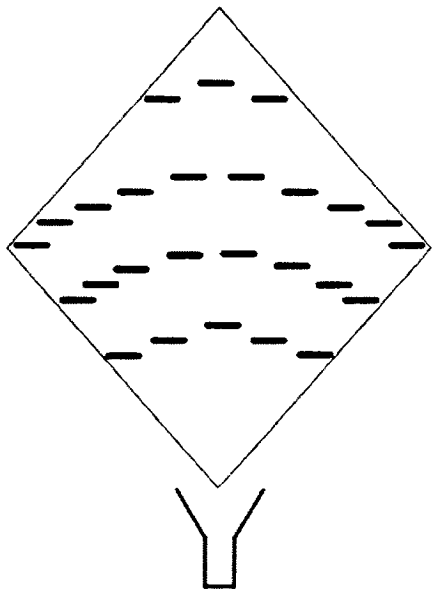

Figure 1.7 - Dipole hologram

1.1.3 Other Holographic Antenna Configurations

Recently two other types of holographic antennas were introduced [8, 9]. The hologram in [8] is based on the binary dipole hologram with shorter dipoles ($0.175\,\lambda_o$) printed on one side of a two layer dielectric substrate. Higher dielectric constants were used to reduce the guided wavelength which enabled more dipoles to be etched on the substrate. And, absorbing materials were lined around the edges of the substrate to reduce the feed's radiation onto the total radiation pattern. These extra considerations enabled the use of a ground plane placed at $\lambda/4$ below the bottom side of the hologram to suppress the undesired bottom lobe. However, no details were mentioned on whether the interference pattern was recorded in free-space or in the presence of the dielectric substrate.

Up to now, all of the holograms were based on a binary quantization scheme where conducting strips were placed at every wavelength. A higher-order quantization scheme was demonstrated in [9] where the hologram consisted of a lattice of sub-wavelength metal patches on a grounded dielectric substrate. The non-uniform lattice pattern based on holographic principles and modulated impedance surface theory produced radiation at an angle in the shadowed region of the feed antenna, i.e. the feed was mounted on a cylinder and the main beam was formed on the other side of the cylinder.

1.2 Thesis Objective and Outline

The free-space hologram was based on a first approximation [2-7] of the free-space interference pattern. Although this has led to good results, the minima positions with respect to the feed is not known and manual adjustments are needed to get the circular strips to coincide with the minima positions. The λ_o strip spacings worked for the single-sided antenna because the substrate is electrically thin ($\approx \lambda_o / 20$) so $\lambda_g \approx \lambda_o$. However, this approach does not work at the design frequency for the double-sided antenna where the substrate is a $\lambda_g / 4$ thick. The thick substrate causes λ_g to decrease considerably resulting in large grating lobes to appear. Another setback with the free-space hologram is the limit on the maximum achievable directivity of the hologram. As a result, the directivity does not increase proportionally with the hologram size once the size limit has been exceeded.

Previous works in [3-7] have addressed other issues while using the free-space interference pattern to realize the binary hologram. The free-space interference pattern used ideal simple sources (spherical reference wave and planar object wave), hence it produced a simple fringe pattern. More complicated patterns could appear when we consider more accurate interference patterns. The objective of this thesis is therefore to:

(a) Investigate the influence of the dielectric substrate on the interference pattern.
(b) Determine the effect of the realistic source on the interference pattern.
(c) Use (a) and (b) to obtain insight into the conducting strip locations with respect to the source and into the required curvature of the strips.

The free-space hologram is a 10cm by 10cm dielectric slab, and at an operating frequency of 30GHz ($\lambda_o = 1cm$), the hologram covers an aperture area of $100\lambda_o^2$. It is electrically large, and is thus challenging to model the full three-dimensional (3-D) hologram even with modern-day computers. Consequently, we will first study the interference patterns using a two-dimensional (2-D) electromagnetic code developed in [5], and extended here, to model the feed horn, dielectric slab, conducting strips, and plane wave source. The 2-D model corresponds to the H-plane plane view of the antenna that was illustrated in Figure 1.3. Using

the 2-D models will reduce the computational load and simulation time while providing insights on the effects of the substrate before using the 3-D models. Chapter 2 will discuss results from the 2-D study of the more accurate interference patterns.

Using the knowledge from the 2-D analyses we will form design "guidelines" that can be carried over to the 3-D study, which will be the subject of Chapter 3. A prototype antenna will be designed and tested to validate concepts in this thesis. The antenna will use a printed-source to eliminate feed alignment problems incurred in using a feed horn, and to eliminate the need for a specialized fixture to hold the hologram since the fixture reduces the low-profile feature of the hologram [7].

Chapter 4 provides some general conclusions as well as suggestions for future work.

Chapter 2 - Two-Dimensional Investigations of Holographic Antennas

To reduce the complexity in studying the effect of the presence of the dielectric substrate on the interference pattern, we will first conduct the study in two-dimensions. The 2-D model is a slight extension of a TM_z integral-equation moment method formulation described in [5, 10] and implemented in [5]. Figure 2.1 illustrates the model where all objects are infinite along the z-axis where we can use two possible sources: an electric line source and/or a plane wave source. The line source has a z-directed current density that produces an $\underline{E}(x,y) = \hat{z}E_z(x,y)$ field to induce currents on other objects. Given that all objects are infinite along the z-axis, all other current densities will be polarized in the z-direction as well. The line source is chosen to be at the origin in the 2-D model. The output of model is the total electric field $E_z^{total} = E_z^{incident} + E_z^{scattered}$. The interference pattern is then the magnitude of the phasor sum of $E_{z,reference}^{total}$ and $E_{z,object}^{total}$ observed at the surface of the substrate. To compare the performance between various antennas we will use a 2-D directivity defined as

$$D(\phi) = \frac{|E_z(\phi)|^2}{\frac{1}{2\pi}\int_0^{2\pi} |E_z(\phi)|^2 \, d\phi} \tag{2.1}$$

where $E_z(\phi)$ is the angle-dependent portion of the total electric field $E_z(\rho,\phi) = \frac{E_z(\phi)}{\sqrt{\rho}} e^{-jk_0\rho}$ in the far-zone [5]. Also, the line source will be the only active source during the computation of the radiation pattern.

A substrate length, L, of 140mm corresponds to the diagonal length of the 10cm by 10cm three-dimensional hologram. We will use L = 140mm and 280mm in this chapter to show the advantage of using the true interference pattern to synthesize the hologram. In the 2-D model, the substrate will exist from x = 110 to 250mm, and x = 110mm to 390mm for L = 140mm

and 280mm, respectively. Other parameters for the model are given in Table 2.1 and changes to these parameters will be noted.

Table 2. 1 - Parameters for 2-D model

f	30GHz
t	0.508mm
w	0.254mm
ε_r	3.38

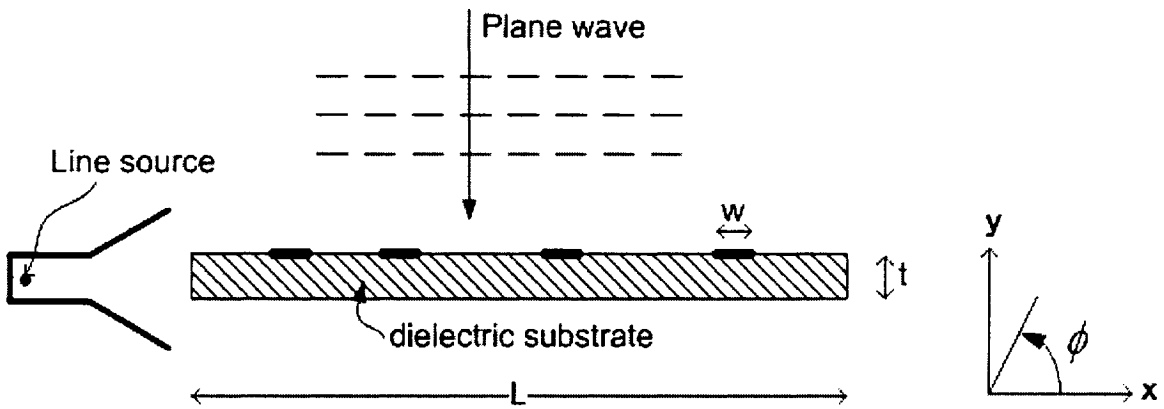

Figure 2.1 - Two-dimensional electromagnetic model of the holographic antenna and planar object wave

In Section 2.1 we study the effect of the presence of the substrate on the interference pattern and the directivity of the antennas realized from these patterns. Section 2.2 considers the effect of the substrate thickness on the interference patterns and directivities. The double-sided hologram is discussed in Section 2.3, where the performance of the antenna realized from the more accurate fringe pattern is compared with the free-space double-sided antenna. A holographic antenna with a grounded substrate is introduced in Section 2.4, where a ground plane is used to suppress the bottom beam. The 2-D model allows us to examine the power density at any point in the xy-plane, and is used to increase our understanding of the physics of holographic antennas in Section 2.5. In Section 2.6 the operation of the holographic antenna is interpreted in terms of leaky-wave antenna principles. Finally, Section 2.7 summarizes Chapter 2.

2.1 Progressive Considerations of the True 2-D Interference Pattern

We will use three cases to show the effects of the substrate and realistic source on the interference pattern and the antennas synthesized from these patterns. First, we will describe the three cases then compare their interference patterns and directivities in Section 2.2.4.

2.1.1 Case 1: Free-Space Interference Pattern of the Line Source and Plane Wave

The simplest fringe pattern is the interference pattern of a cylindrical reference wave, $\underline{E}_{ref}(x,y) = \hat{z}\frac{A}{\sqrt{\rho}}e^{-jk_n\rho}$, with a planar object wave, $\underline{E}_{obj}(x,y) = \hat{z}Be^{jk_{n}y}$, in free-space observed at the surface of the substrate even though it does not exist in this case. This configuration is illustrated in Figure 2.2. For this case, it is intuitive to set B = A to have equal contribution from both sources in the interference pattern. The hologram is realized by placing strips at the minima positions on the dielectric substrate and fed by the horn antenna to compute the directivity of the hologram.

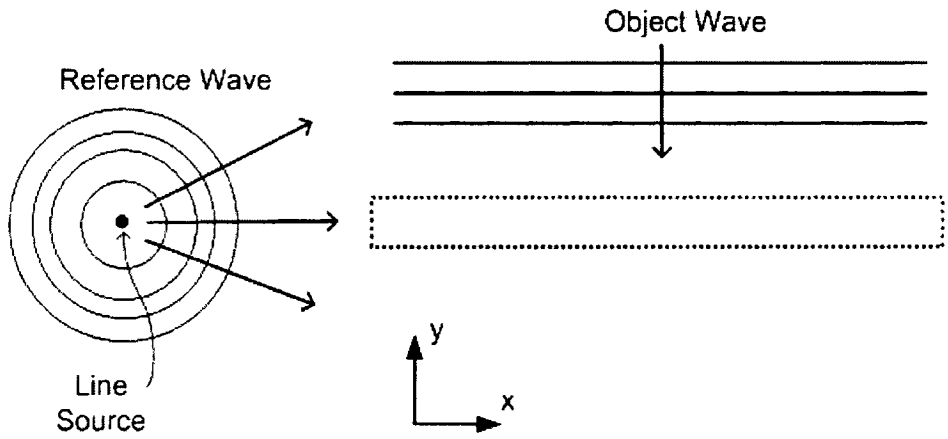

Figure 2.2 - Free-space interference pattern

2.1.2 Case 2: Interference Pattern of the Line Source and Plane Wave Determined in the Presence of the Dielectric Substrate

This case uses the same ideal sources as case 1 but includes the presence of the substrate to observe its effect on the interference pattern. Figure 2.3 illustrates the geometry where the

fringe pattern is observed along the substrate's surface. The amplitude of the incident plane wave, B, is now set to be the magnitude of the incident field, $\left|\underline{E}_{ref}^{inc}(x_o, y_o)\right|$, due to the line source at the top edge of the substrate denoted by the point (x_o, y_o) in Figure 2.3. This value was chosen because we are interested in the field interactions in the substrate region and it produced high directivity for case 3 (the true interference pattern). Also, we cannot set the amplitude of the incident plane wave to be the amplitude of the incident field due to the line source at the source, denoted by the point (x_A, y_A) in Figure 2.3, because it is singular at the source, where the incident field of the line source is given by

$$E_z^{inc}(\rho) = \frac{-k_o^2}{4\omega\varepsilon_o} H_o^{(2)}(k_o|\rho|) \tag{2.2}$$

where $H_o^{(2)}(k_o|\rho|)$ is the Hankel function of second kind and zero order, and $\rho = \sqrt{x^2 + y^2}$ is the observation point [11].

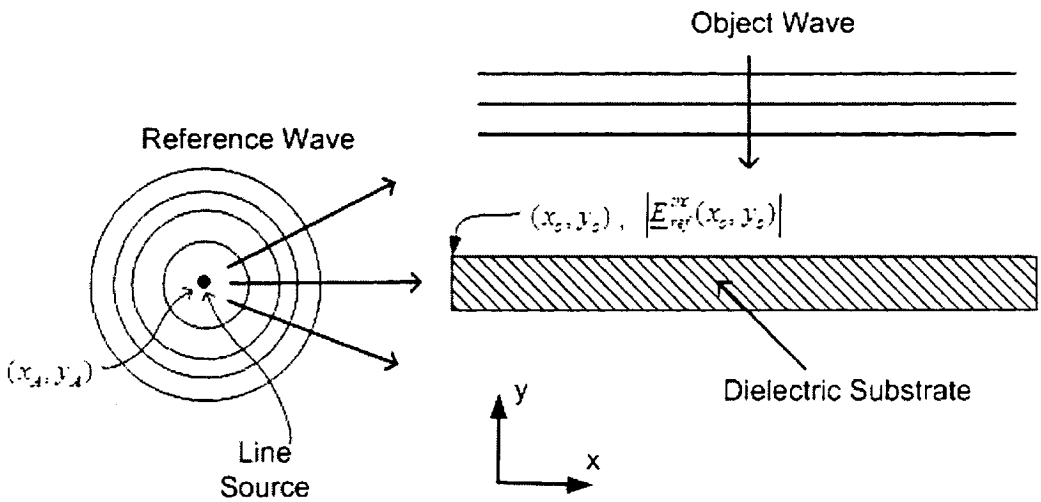

Figure 2.3 - Interference of line source and plane wave with the presence of the substrate

2.1.3 Case 3: True Interference Pattern of the Feed Horn and Plane Wave Determined in the Presence of the Dielectric Substrate

To compute the true 2-D interference pattern, the horn antenna modelled by the line source and horn walls is used to generate the reference wavefront to interfere with the plane wave. The pattern is observed along the surface of the substrate as illustrated in Figure 2.4. The

amplitude of the incident plane wave is also set to be the amplitude of the incident field due to the line source at the top edge of the substrate.

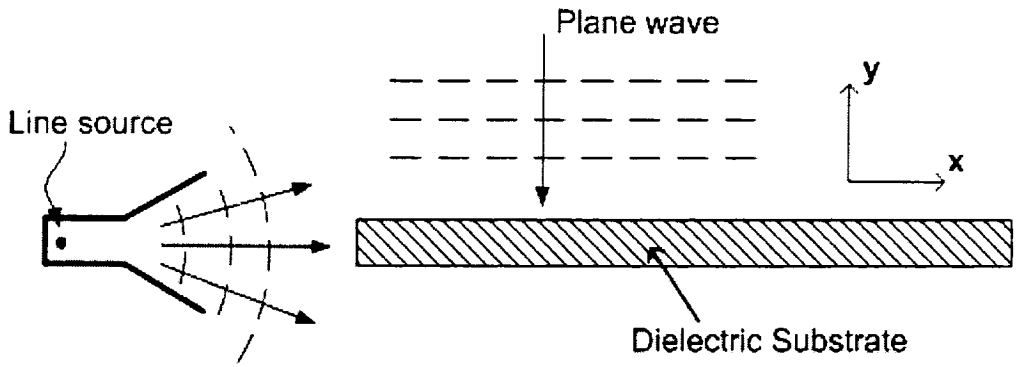

Figure 2.4 - True 2-D interference pattern

2.1.4 Comparison of Antenna Parameters for Case 1 to 3

The interference patterns for case 1-3 (using a substrate length of 140mm) are shown in Figure 2.5. The amplitude of the interference pattern is unimportant here since in the binary quantization scheme we are only interested in the locations of the minima. Case 1 is the free-space interference pattern so the distance between its minima is λ_o = 10mm. Although the strict spacing between the minima is not exactly λ_o, we will use the average distance in the substrate region when we discuss it for brevity, the antennas' strip locations will use the minima coordinates from their corresponding interference patterns. For the observation points far from the source the free-space fringe spacing converges to λ_o, just as the distance between Fresnel zones converges to $\lambda/2$ in binary Fresnel lenses [13]. Case 2 uses the same ideal sources as case 1 but has the presence of the substrate so its fringe spacing is λ_g = 9.4mm. Case 3 has double-minima instead of distinct single-minima in the substrate region like case 1 and 2. Its effect will be discussed after we compare the radiation patterns of case 1 and 2. It is free-space beyond the substrate region for all three cases so the spacing between the minima is λ_o for all cases.

The interference patterns for case 1-3 with L = 140 and 280mm have the same behaviours. For brevity, radiation patterns of case 1-3 are shown for the holograms using L = 280mm.

The directivity of each case for both L = 280mm and 140mm are shown in Table 2.2 and 2.3, respectively.

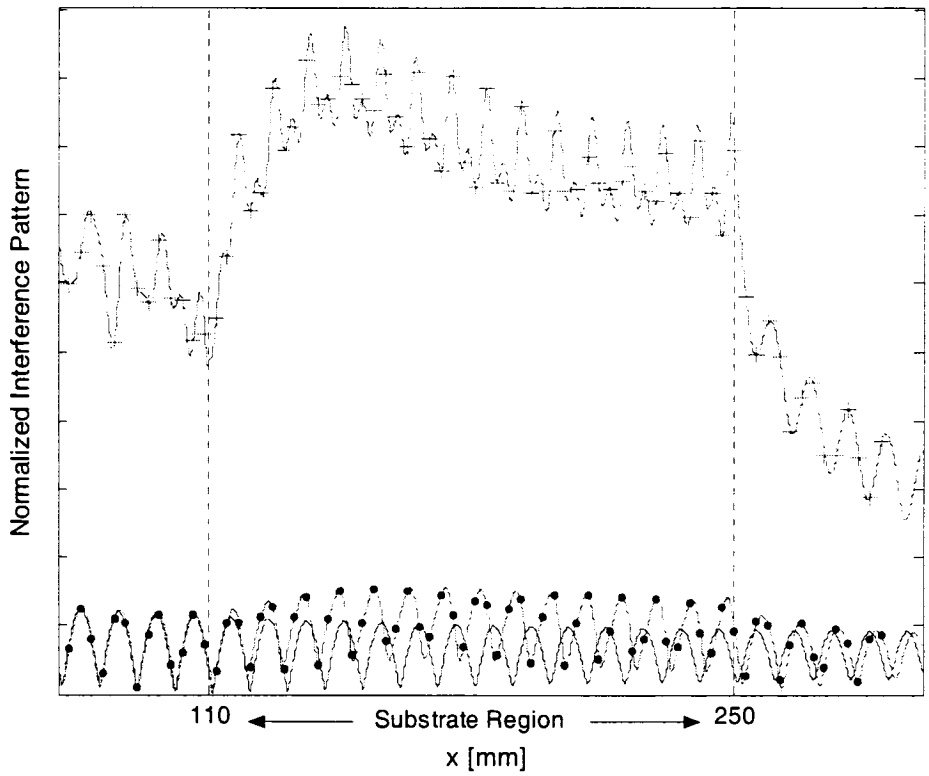

Figure 2.5 - Interference patterns for case 1 (————), case 2 (— • — • — • —), and case 3 (— + – – + — + —) with L = 140mm, f=30GHz

The radiation pattern of case 1 and the free-space holograms are shown in Figure 2.6. Case 1 is similar to the free-space hologram where the strip spacings are nearly periodic instead of periodic. However, they produced different radiation patterns due to different strip locations with respect to the feed. The free-space hologram worked well for electrically thin substrates such as case 1 because $\lambda_o \approx \lambda_g$. The beam peak is slightly off broadside because the strips are spaced at every λ_o instead of λ_g. Figure 2.7 compares the directivity of case 2 and the free-space hologram, where case 2 is worse because with broadside radiation the backfire lobe is radiating directly toward the feed horn and the two interfere with each other which result in a decrease in directivity. The interference in the feed can also be observed by comparing the Standing Wave Ratio of the two cases in Table 2.2. Note that a description of all the cases used in this chapter is also given Appendix A.

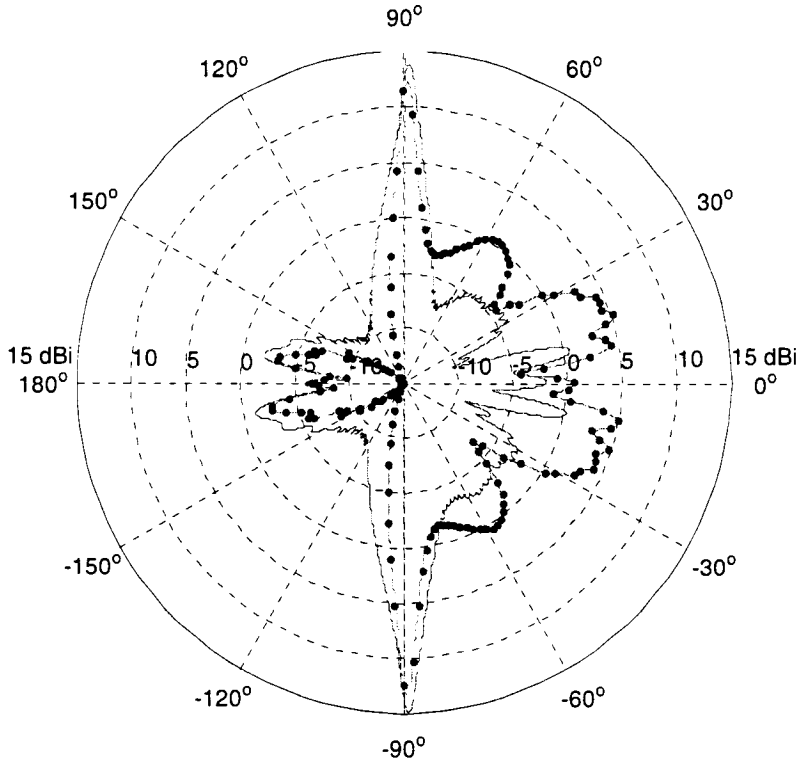

Figure 2.6 - Directivity of free-space (— • — • — • —) and case 1 holograms (————————), f=30GHz

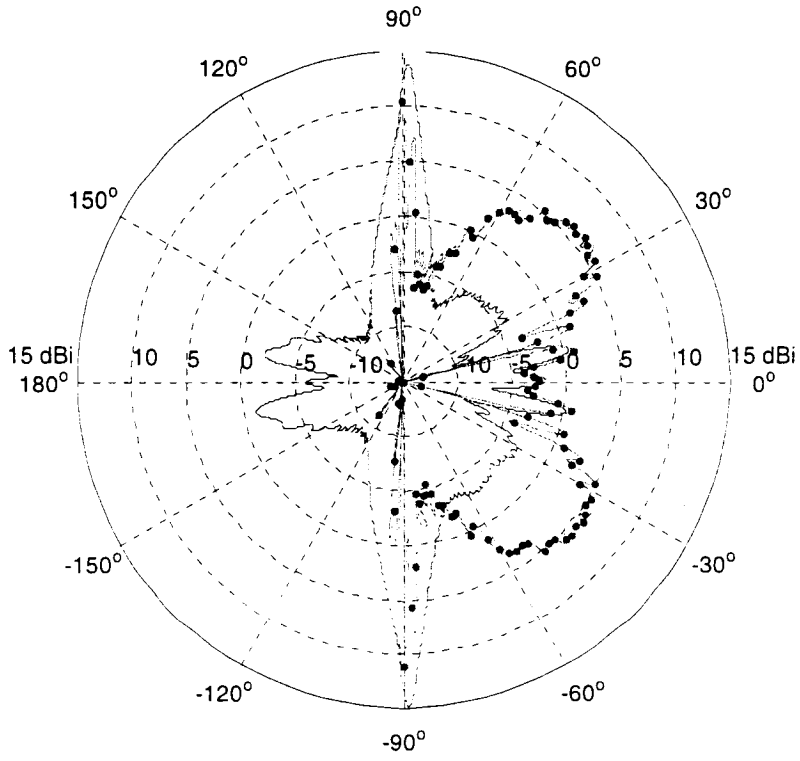

Figure 2.7 - Directivity of free-space (————————) and case 2 holograms (— • — • — • —), f=30GHz

For case 3, the true interference pattern exhibits pairs of minima with a higher minimum and lower minimum in each pair. The distance between just the higher minima is λ_g. The distance between just the lower minima is also λ_g. The distance between the higher and lower minimum in each pair is 3.75mm. We can realize a broadside antenna by placing strips at every λ_g, i.e. placing strips just at the higher minima or just at the lower minima. The first intuitive attempt is to place strips at only the lower minima to quantize the interference pattern, but we will try both cases where placing strips at only the higher minima is case 3a and case 3b denotes placing strips at only the lower minima. Their radiation patterns are shown in Figure 2.8. Their directivities are low because of the same feed interference problem in the broadside hologram of case 2. And, it is counter-intuitive that the directivity of case 3b is worse than that of case 3a since case 3b used strips placed at only the lower minima. It was expected that placing strips at the lower minima would be a better quantization choice and give higher directivity than placing strips at only the higher minima.

To observe how the higher and lower minima behave as a function of substrate length we compared the interference patterns of case 2, 3 for various substrate lengths. Figure 2.9 and 2.10 show the interference patterns of case 2, 3 for L = 140mm and 160mm, respectively. For L = 140, 280mm, or multiples of 140mm, the higher minima occur before the lower minima and the higher minima position is close to the minima position of case 2. But for L = 160mm, or multiples of 160mm, the occurrence of the higher minima and lower minima switch around with the lower minima occurring before the higher minima. It is a coincidence that the case 3a antenna (with strips placed at only higher minima) has higher directivity than the case 3b antenna (with strips placed at only lower minima) for L = 280, and 140mm. The situation reverses for L = 160, 320mm where the antenna with strips placed at just the lower minima give better directivity compared to that using strips placed just at the higher minima. Therefore, we cannot quantize the double-minima behaviour with the usual single strip approach because it cannot produce consistent results.

Although the occurrence of the higher and lower minima changes with the length of the substrate, the relative distance between the higher and lower minima stay the same. This behaviour can be related to standing wave patterns on a transmission line with the reference source and plane wave source being the sources of the transmission line. Varying the substrate length corresponds to varying the line length and cause the standing wave pattern to change with the line length. Therefore the occurrence of the higher and lower minima varied with the length of the line but the relative distance between the minima did not change because we did not change the operating frequency.

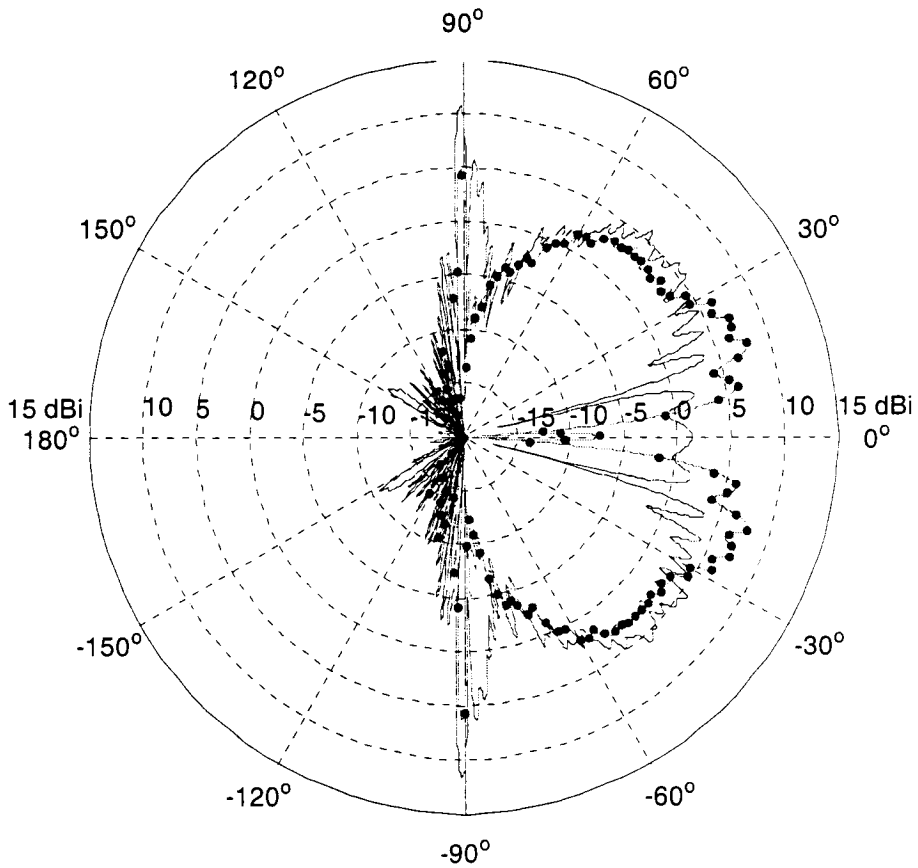

Figure 2.8 - Directivity of case 3a (————) and case 3b holograms (— • — • — • —), f=30GHz

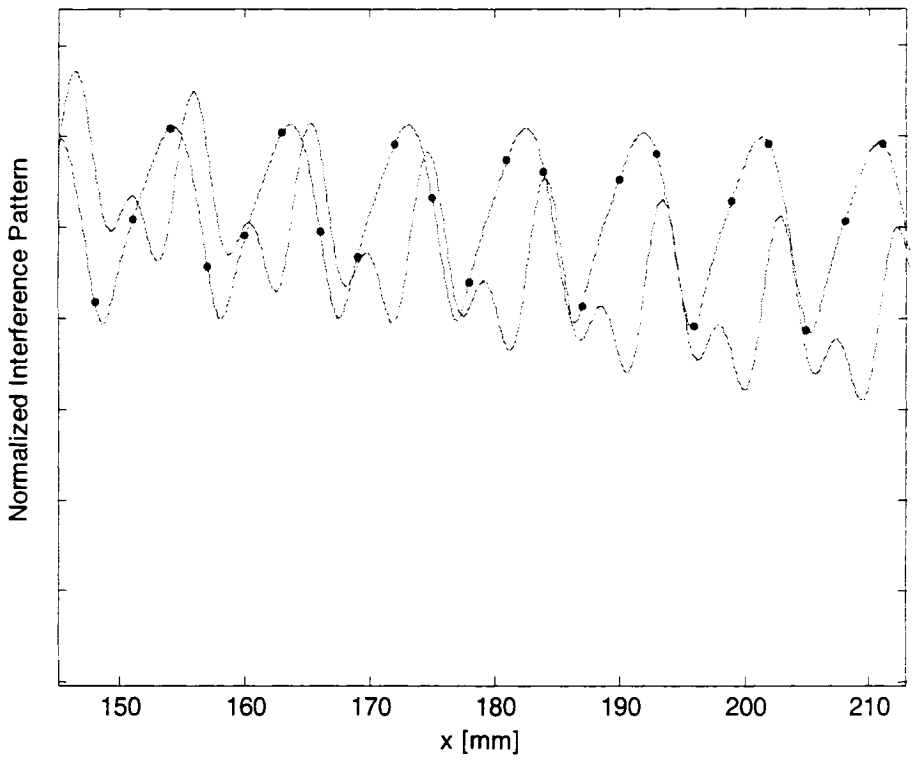

Figure 2.9 - Interference patterns for case 2 (— • — • —) and case 3 (———) with L = 140mm, f=30GHz

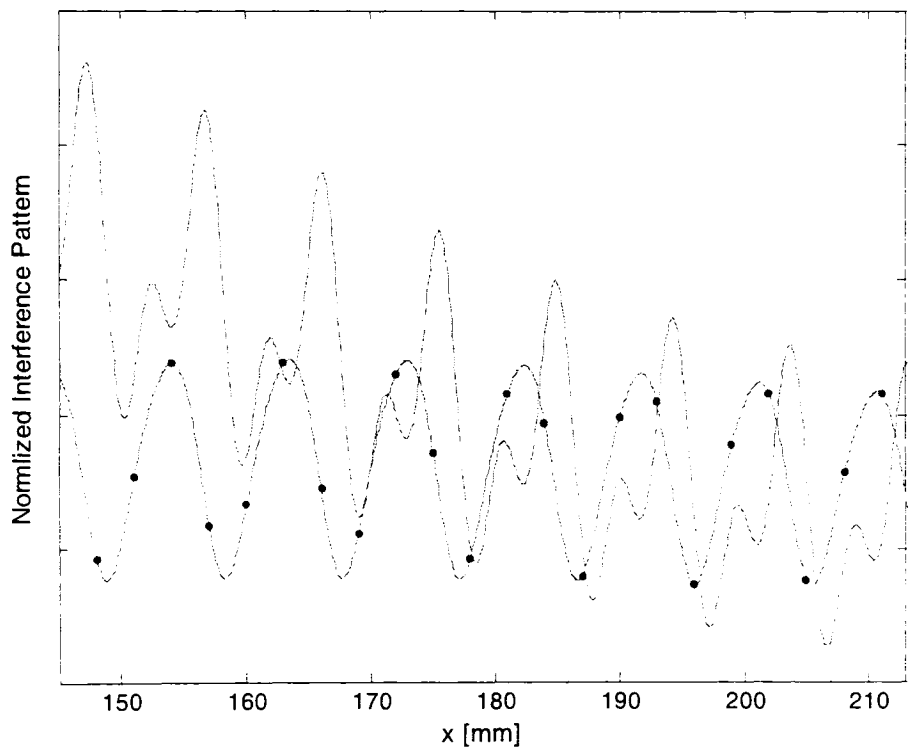

Figure 2.10 - Interference patterns for case 2 (— • — • —) and case 3 (———) with L = 160mm, f=30GHz

In the binary hologram quantization scheme, we use conducting strips to mimic the minima behaviour by forcing the electric field to zero at the strip locations. Placing a single strip at only the higher or lower minimum will confine the field to zero in a region smaller than the double-minimum region. Therefore, we need to place pairs of strips at the double-minima to force the field to zero over a larger area to mimic the double-minima behaviour. Placing single strips at only lower minima or only higher minima can be viewed as under-quantizing or under-sampling the double-minima behaviour.

We tried two quantization schemes with the double-strips approach where strips of equal width (of 0.254mm) were placed at all minima, referred to as the case 3 antenna in Figure 2.11 and Table 2.2, and the second quantization scheme, referred to as case 3d in Table 2.2, using a strip width, w, of 0.254mm for strips placed at the higher minima and w = 0.508mm for strips placed at the lower minima in an attempt to differentiate and quantize between the higher and lower minima. Both case 3 and 3d produced similar behaviours because the field are simply forced to zero at the strip positions and the binary quantization scheme does not have enough "resolution" to force the field to different amplitude levels to correspond with the amplitude of the minima. Case 3 was then fine tuned by optimizing its strip locations (where each strip was allowed to move +/- 2mm or $2\lambda_o/10$) since the binary hologram is an approximation to the interference pattern. The optimal strip locations gave a 3.7dB improvement in directivity compared to the free-space hologram. As shown in Figure 2.12, we also optimized the free-space hologram to compare it with the new optimized hologram. Comparison of the directivities of the antennas using L = 140, 280mm in Table 2.2, and 2.2 show that the new hologram is more efficient than the free-space hologram where the aperture efficiency, e_{ap}, of the free-space antenna decreases as L increases, whereas the new hologram has the same or better e_{ap} for increasing L. The ideal 2-D directivity, $D_{uniform}$, used in the aperture efficiency was computed numerically since the ideal 3-D directivity of a uniform aperture distribution given by $D_{\text{uniform}} = \frac{4\pi \ \ Area}{\lambda_o^2}$ [13] cannot be applied to 2-D antennas. A procedure using a plane wave angular spectrum representation to compute the 2-D D_{uniform} is described in Appendix B [12].

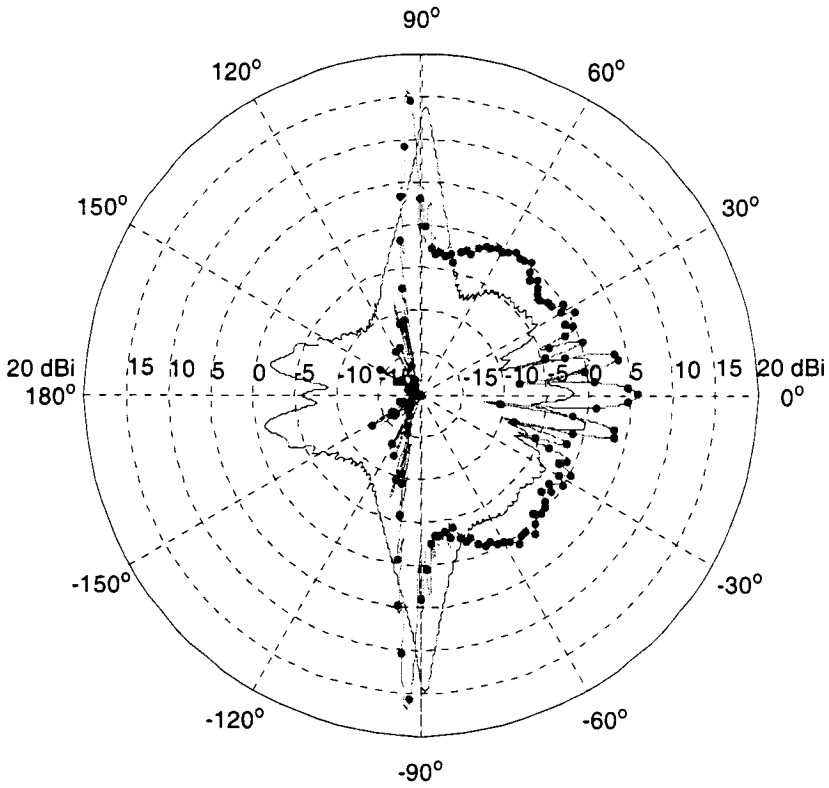

Figure 2.11 - Directivity of case 3 (— • — • —) and free-space holograms (————), f=30GHz

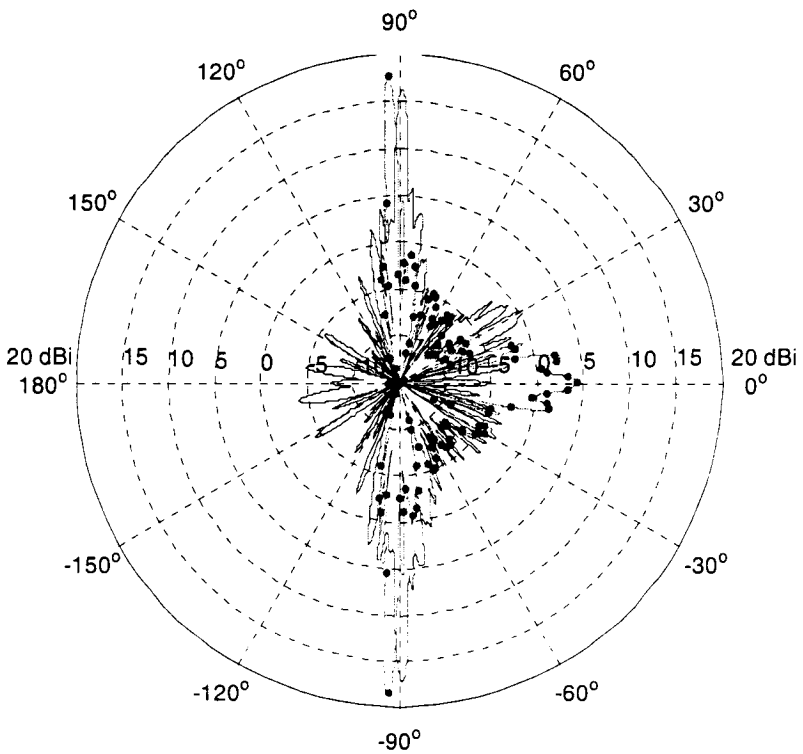

Figure 2.12 - Directivity of optimized case 3 (— • — • —) and optimized free-space holograms (———— ————), f=30GHz

Table 2.2 - Directivity of case 1-3 holograms, L = 280mm

Type of hologram	D [dBi]	Angle of D_{max} [degrees]	e_{ap} [%] with $D_{uniform}$ = 19.48dBi	SWR [dB]
Just the horn antenna	Not Applicable	Not Applicable	Not Applicable	0.4
Case 1	13.26	-89.3	23.9	11.3
Free-space	**14.89**	**-89.1**	**34.8**	**13.9**
Optimized free-space	**17.31**	**-89.4**	**60.7**	**13.6**
Case 2	11.29	-90.2	15.2	15.7
Case 3a, strips placed at only higher minima	11.61	-90.4	16.3	13.4
Case 3b, strips placed at only lower minima	6.24	-90.4	4.7	12.1
Case 3, w = 0.254mm for all strips	**16.84**	**-92.6**	**54.5**	**6.9**
Optimized case 3	**18.6**	**-92.1**	**81.7**	**7.8**
Case 3d, w = 0.254mm for strips at the higher minima location and w 0.508mm for strips at the lower minima	16.66	-92.9	52.2	5.8

Table 2.3 - Directivity of case 1-3 holograms, L = 140mm

Type of hologram	D [dBi]	Angle of D_{max} [degrees]	e_{ap} [%] with $D_{uniform}$ = 16.48dBi	SWR [dB]
Just the horn antenna	Not Applicable	Not Applicable	Not Applicable	0.4
Case 1	11.13	-88.9	29.16	11.2
Free-space	**13.34**	**-88.7**	**48.9**	**14.3**
Case 2	10.18	-89.8	23.5	17.4
Case 3a, strips placed at only higher minima	9.94	-90.1	22.2	15.9
Case 3b antenna, strips placed at only lower minima	6.65	-90.5	10.4	15
Case 3, w = 0.254mm for all strips	**13.46**	**-92.7**	**49.9**	**4.7**
Optimized case 3	**14.7**	**-91**	**66.4**	**3.5**
Case 3d, w = 0.254mm for strips at the higher minima location and w 0.508mm for strips at the lower minima	13.64	-92.9	52	4.6

Inspections of Tables 2.2 and 2.3 also show lower SWR for the off-broadside antennas compared to the broadside antennas. This will translate to a lower return loss for 3-D antennas that operate away from broadside because the backfire lobe will not be radiating directly back toward the feed antenna.

Although the new hologram showed higher directivity than the free-space hologram, the beam shifted off broadside by about 2-3°. We conjecture that the beam shift is due to the presence of the reflected (and hence standing) wave in the substrate, as well as mutual coupling between the strip pairs. The beam shift is not due to the strip locations and can be verified by using the array factor to compute the pattern due to the strip positions and phase distribution. Coupling effects are ignored in the array factor since the strips are modelled as isotropic point sources. The array factor [13] for the geometry considered in Figure 2.13 is

$$AF(\theta) = \sum_{n=1}^{N} A_n e^{j(k_o z_n \cos\theta + \beta_n)} \tag{2.3}$$

where $k_o = 2\pi/\lambda_o$, z_n is the distance of the n-th strip from the first strip using the actual minima position from the interference pattern, $\beta_n = -z_n \dfrac{2\pi}{\lambda_g}$ is the phase of the n-th strip in this space-fed configuration, A_n is the amplitude of the n-th strip. λ_g was used instead of λ_o in β_n to account for the effect of the dielectric slab. The normalized array factor using the actual strip positions is shown in Figure 2.14 for an idealized uniform amplitude distribution (with $A_n = 1$). We also tried a tapered amplitude distribution with $A_n = e^{-\alpha z_n}$, $\alpha = 1/10$ to confirm that the beam peak is determined by the phase distribution of the antenna.

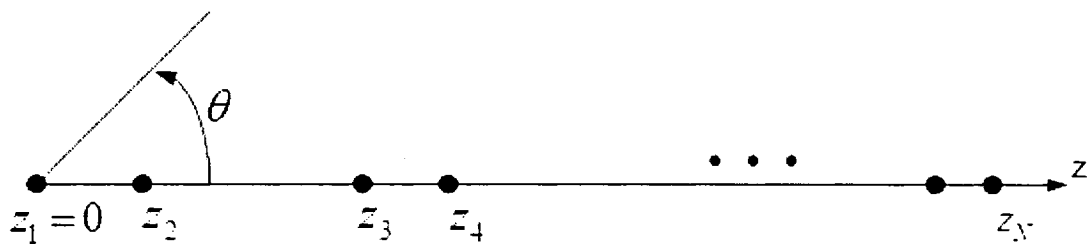

Figure 2.13 - Array of point sources with its spacing based on the interference pattern minima spacing

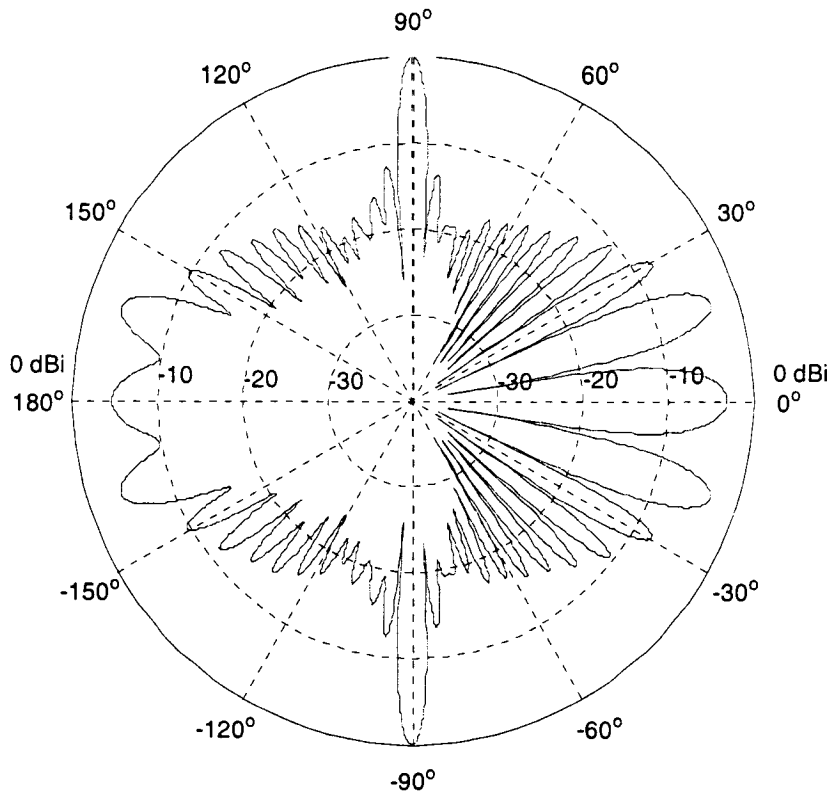

Figure 2.14 - Normalized array factor using the strip locations from the interference pattern minima, t = 0.508mm, L = 140mm, f=30GHz

To observe the changes in the strip positions after optimization we compared the strip positions of the optimized antenna with that of the initial antenna for case 3. The same procedure was also applied to the optimized and un-optimized free-space antenna. The strip movement restriction for case 3 is +/- 2mm and we see that most of the strips moved about 1mm ($\lambda_o/10$) in Figure 2.15, so case 3 is a more accurate realization than the optimized free-space hologram where most of its strips moved more than 1mm in Figure 2.16. The strip movement restriction for the free-space antenna was +/- 5mm since the strips were spaced at every 10mm. It is interesting to note that 13 out of 27 strips in the optimized free-space hologram were within 1mm of the strip positions of the optimized case 3 antenna (which was synthesized from the true interference pattern).

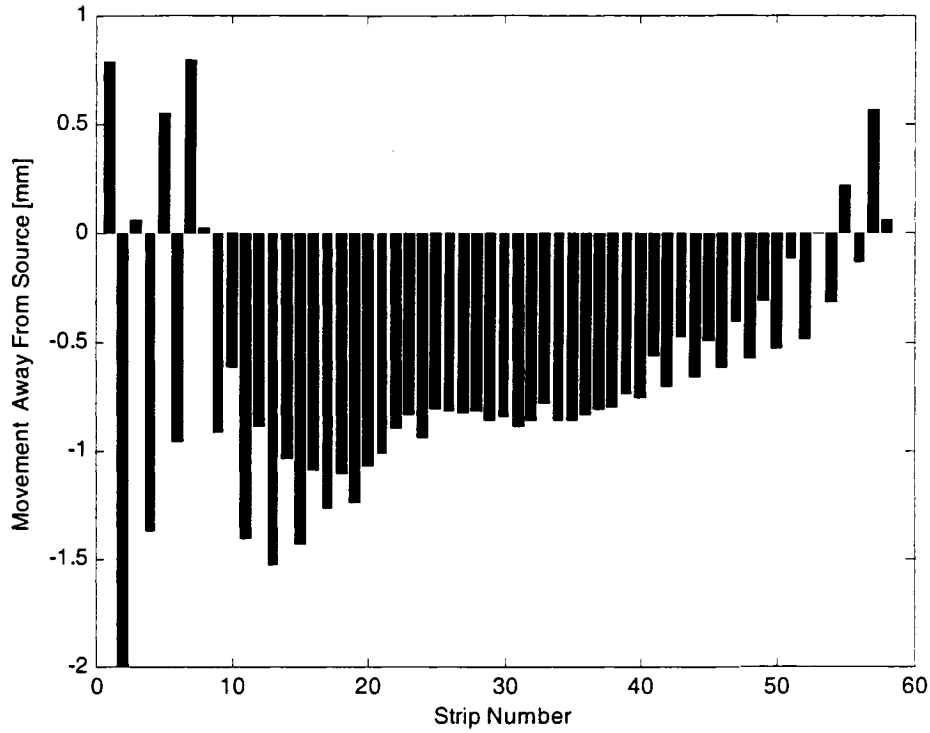

Figure 2.15 - Strip movements of optimized antenna compared to initial antenna for case 3

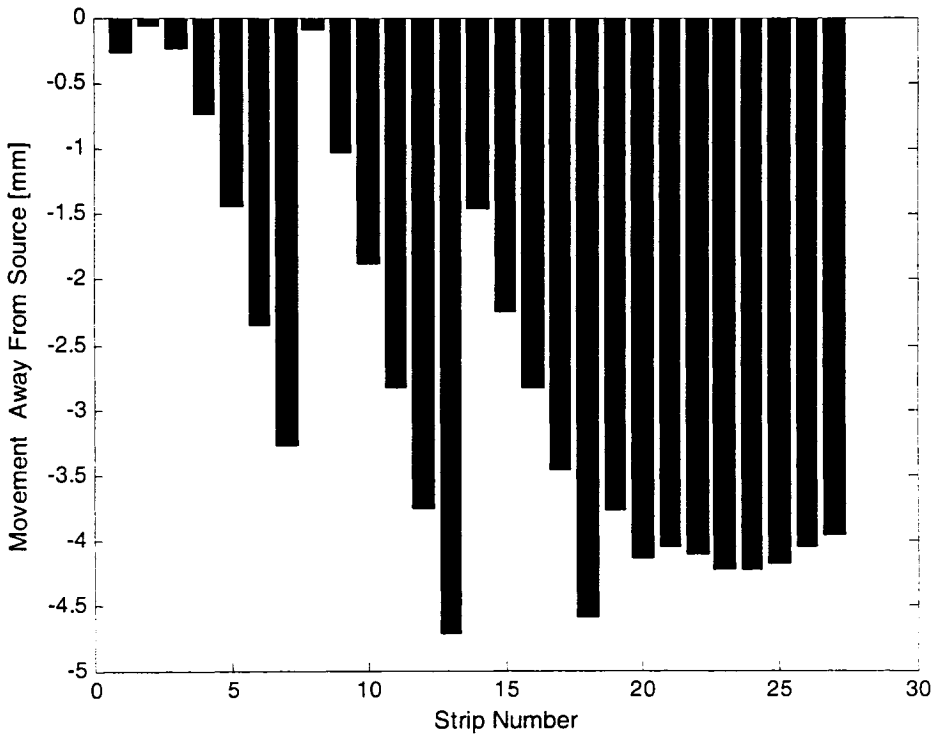

Figure 2.16 - Strip movements of optimized antenna compared to initial antenna for the free-space hologram

The directivity and angle of directivity of the free-space, case 3, and optimized case 3 antennas from 25-35GHz are shown Figures 2.17 and 2.18, respectively. The beam scanned with frequency because the phase distribution of the antennas changes with frequency. For broadside radiation, the distance between the strips is equal to λ_g of the design frequency, f_o. At frequencies lower than f_o, this distance is smaller than λ_g of the lower frequencies so the beam will be scanned off broadside towards the backfire direction. And at frequencies higher than f_o, the distance is larger than λ_g of the higher frequencies so the beam will be scanned off broadside towards the endfire direction, and grating lobes will appear causing the directivity to decrease. This is why the directivity decreased drastically for the case 3, optimized case 3 antennas at frequencies higher than 32GHz and at frequencies higher than 31GHz for the free-space antenna. Also, the directivity is low when the antennas scan through broadside, which is 29GHz for the free-space antenna, 31GHz for case 3, and 32GHz for the optimized case 3 antennas. The directivity is inherently narrowband because like the optical holograms the holographic antennas only work well at the recorded/designed wavelength.

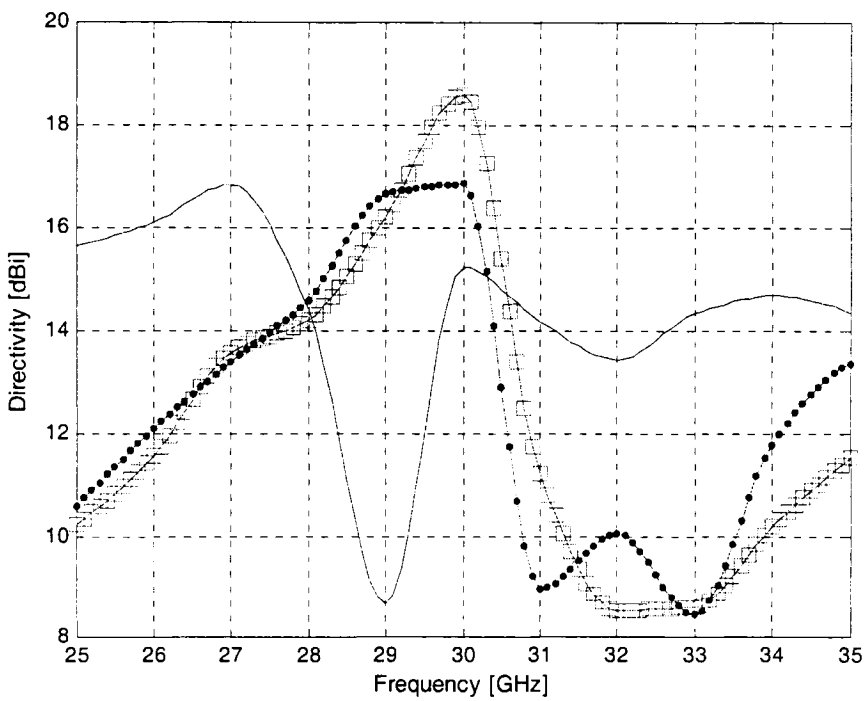

Figure 2.17 - Directivity of free-space (——————), case 3 (— • — • — • —), and optimized case 3 (— □ — □ — □ —) holograms, L = 280mm

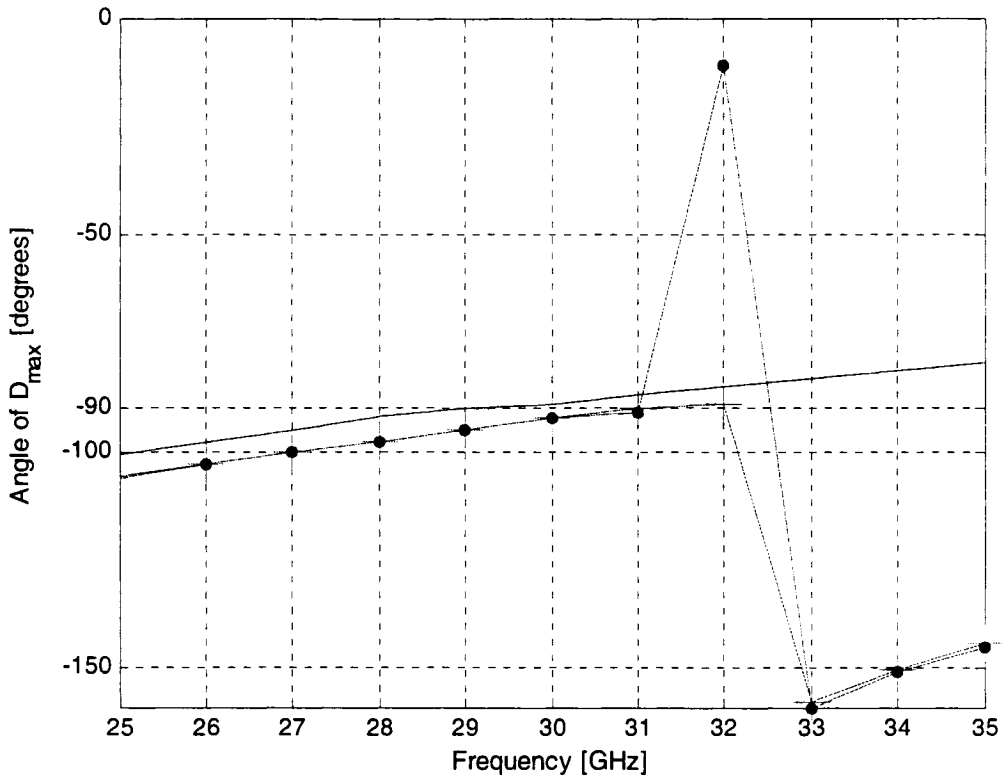

Figure 2.18 - Angle of directivity of free-space (——————), case 3 (— • — • — • —), and optimized case 3 (— □ — □ — □ —) holograms, L = 280mm

2.1.5 Comparison of Antenna Parameters for Case 1 to 3 with Non-Equal Source Amplitude Used in the Recording Stage of the Interference Patterns

When we recorded the interference patterns in case 1-3, we let the amplitude of the plane wave be equal to the amplitude of the reference wave. This section will discuss the effect of varying the sources' amplitude on the interference patterns. We will keep the amplitude of the reference source, A, the same as before and vary the amplitude of the plane wave source, B. For case 1, the profile of the fringe pattern did not change as we changed B, the minima position moved slightly by at most 1mm and did not change the directivity by more 0.2dB when ratios of B/A = [0.01, 100] were used. For case 2, when B is much smaller than A the contribution from the plane wave to the interference pattern will be negligible and the interference pattern will look like the total field due to just the line source with the presence of the substrate. The opposite situation occurs when B is much larger than A, where the pattern resembles the total field due to just the plane wave with the presence of the substrate.

In between these extreme B/A ratios, we can vary B/A to get the interference pattern to exhibit a double-minima behaviour that we saw earlier in the true interference pattern of case 3. We can then make use of this feature to place more strips on the substrate to increase the antenna's directivity. Table 2.4 shows the directivity for case 2 where a B/A ratio of 0.1 gives the maximum directivity when pairs of strips are placed at the double-minima of the interference pattern. The B/A ratio is dependent on the initial value of B where B is only the amplitude of the incident plane wave, but by using the average total field ratio in the region of the substrate the dependence on the choices of B can be ignored. Therefore we will also use a ratio of the average total field due to the plane wave compared to the average total field due to the reference wave in the substrate region to represent the optimal ratio for maximum directivity. The average field ratio representation is similar to the ratio of the reference beam intensity to object beam intensity in [14] where it was determined experimentally for specific setups to enhance image quality. Table 2.5 shows the optimal ratio for the true interference pattern where the initial ratio (B/A = 1) is close to the optimal ratio (B/A = 1.1), for that reason we presented the results of using B/A = 1 for all cases in the first discussion of the interference patterns in Sections 2.1.1 to 2.1.4. And although the directivity from the optimal field ratio of case 2 is relatively good compare to case 3, we will use case 3 to synthesize the holograms because case 3 represents the true interference pattern in 2-D.

Table 2.4 - Field ratios for case 2 with L = 280mm, w = 0.254mm, t = 0.508mm

B/A ratio	Field ratio of Object wave to Reference wave in substrate region	D [dBi]	Number of strips
0.1 (optimal ratio)	0.053	16.16	58
1 (initial ratio)	0.533	11.29	29

Table 2.5 - Field ratios for case 3 with L = 280mm, w = 0.254mm, t = 0.508mm

B/A ratio	Field ratio of Object wave to Reference wave in substrate region	D [dBi]	Number of strips
1 (initial ratio)	0.069	16.84	58
1.1 (optimal ratio)	0.076	16.92	58

Initially we thought the double-minima behaviour was caused by the more complicated reference wavefront generated by the feed horn, but the double-minima was also observed in case 2 where the reference source is a simple cylindrical wave the only difference between

case 2 and case 1 (the simplest case) is the inclusion of the finite substrate. Therefore the double-minima behaviour is caused by the presence of the finite-length dielectric substrate for any type of sources. This behaviour can viewed in terms of transmission lines where the finite-length substrate is a transmission line of finite length, the reference source and plane wave source are two sources that will excite their own standing wave patterns with different minima locations on the transmission line. The interference pattern is the sum of the standing waves where for some particular source amplitude values the interference pattern will exhibit double-minima instead of single-minima.

2.2 The Effect of the Substrate Thickness on the Interference Pattern

This section will discuss the effect of the substrate thickness on the interference pattern and antenna's directivity since a $\lambda_g / 4$ thick substrate will be used to realize the double-sided hologram. We will use the same procedure described in Section 2.1.5 where we will vary the plane wave's amplitude to obtain the double-minima behaviour and to maximize the hologram directivity. Figure 2.19 shows the dependence of the optimal field ratio on the substrate thickness. Only the field ratio is shown since the field ratio defined in Section 2.1.5 is proportional to the B/A ratio shown Tables 2.4 and 2.5. Although the initial B/A = 1 ratio gave high directivity for the thin substrate (t = 0.508mm), Figure 2.20 illustrates the benefit of varying B/A for a substrate thickness of 1.36mm where the directivity of a hologram using the initial ratio (B/A = 1) is compared with that using the optimal ratio. An improvement of about 10dB was achieved when using the optimal ratio for this thickness. However, the beam of the hologram using the optimal amplitude ratio has shifted off broadside due to mutual coupling between the closely spaced strips. The thicker hologram caused λ_g to decrease from 9.4mm (for t = 0.508mm) to 7.72mm (for t = 1.36mm), and caused the distance between the higher and lower minimum in the double-minima to decrease from 3.74mm to 2.53mm. This in turn caused the mutual coupling to be stronger and tilted the beam farther away from broadside. The linear array factor which does not consider mutual coupling was used to compute the beam angle using the actual strip locations, and its pattern showed a broadside beam in Figure 2.21.

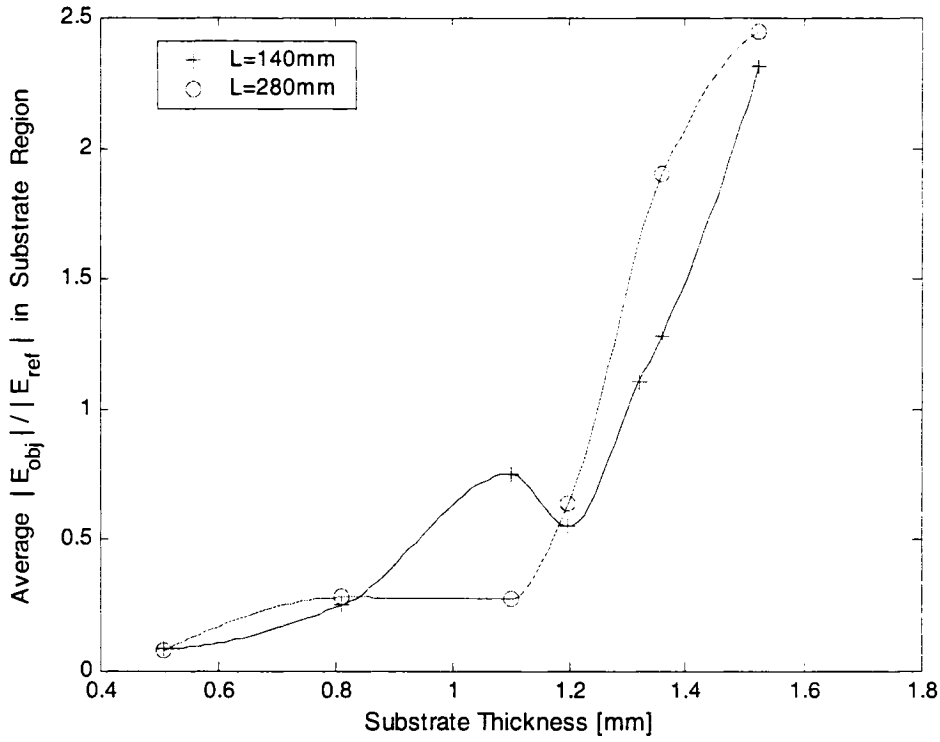

Figure 2.19 - Field ratio to maximize hologram directivity with L = 140, 280mm

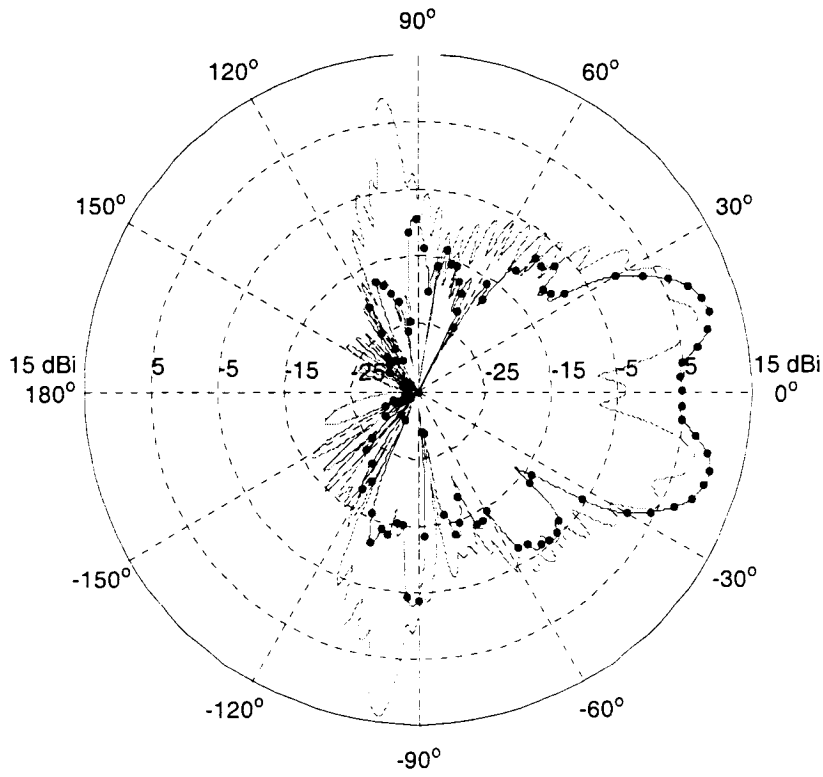

Figure 2.20 - Directivity of holograms with initial B/A ratio (— • — • — • —), optimal ratio (————— ————) for t = 1.36mm, L = 140mm, f=30GHz

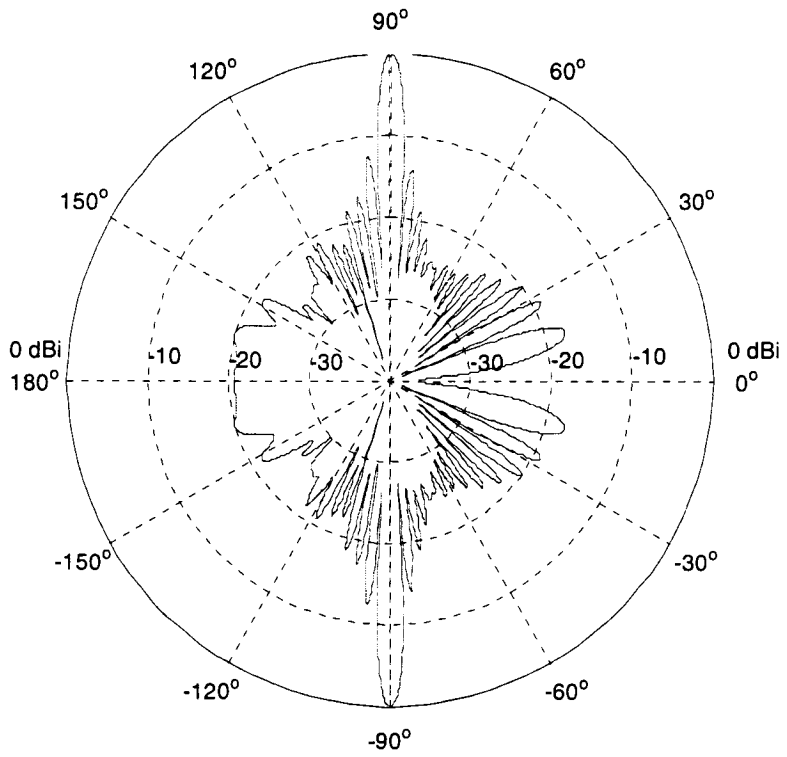

Figure 2.21 - Normalized array factor using the optimal strip locations from the interference pattern minima, t = 1.36mm, L = 140mm, f=30GHz

2.3 Double-Sided Holographic Antenna

The double-sided hologram is realized by placing a set of strips according to the true interference pattern minima observed at the top surface of the substrate, then a second set of strips is placed on the bottom surface with the same strip spacings but with an offset distance, O, to reduce the bottom beam, (O is defined in Figure 1.6). Two offset spacings with O $= \lambda_o / 4 = 2.5$mm and O $= \lambda_g / 4 = 1.93$mm were used to determine the best directivity and back lobe suppression. For the wave travelling along the substrate in the axial direction $\lambda_g =$ 7.72mm, but in the vertical direction through the substrate $\lambda_g = \lambda_o / 4\sqrt{\varepsilon_r} = 1.36$mm since the substrate is electrically long. So the double-sided hologram will use a 1.36mm thick substrate. As shown in Figure 2.22, the hologram using O $= \lambda_o / 4$ instead of $\lambda_g / 4$ produced higher directivity and front-to-back ratio so we will use O $= \lambda_o / 4$. The new double-sided hologram is also compared with the free-space double-sided hologram in Figure 2.23. The

free-space hologram used strips spaced at 10mm which is larger than λ_g and this caused gratings lobes to appear and decreased the directivity.

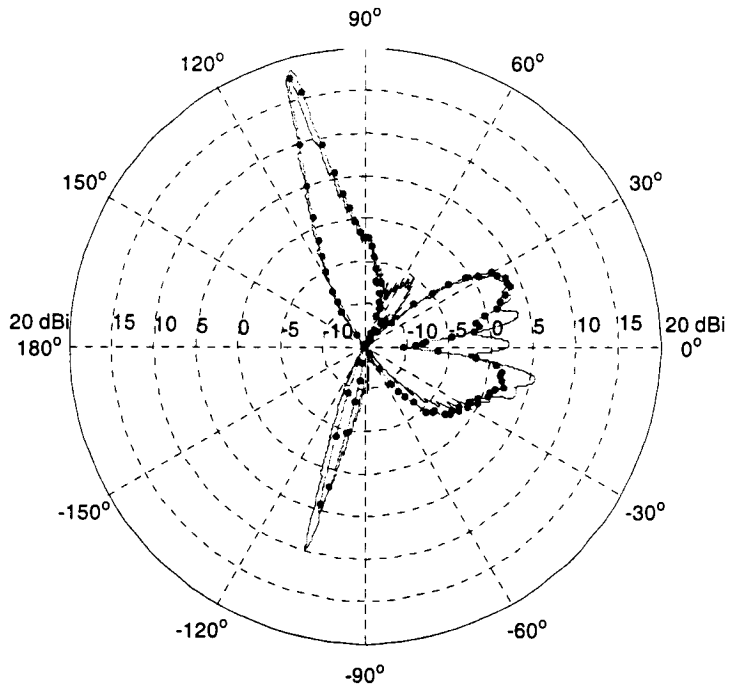

Figure 2.22 - Directivity of double-sided holograms using O = 2.5mm with D = 18.7dBi (— • — • — • —) and O = 1.93mm with D = 17.8dBi (————————), f=30GHz

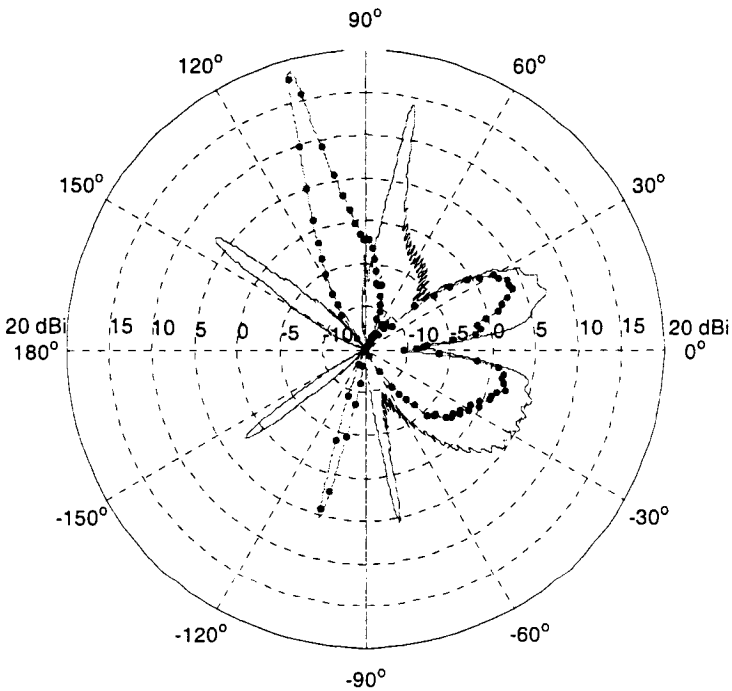

Figure 2.23 - Directivity of double-sided hologram, O = 2.5mm (— • — • — • —) and free-space double-sided hologram (————————), f=30GHz

Using the same optimization procedure as in the single-sided hologram, the double-sided hologram was optimized and gave a 2.8dB directivity improvement as shown in Figure 2.24 and Table 2.6. The ideal 2-D directivity, $D_{uniform}$, for the single-sided case is 19.48dBi with L = 280mm, so $D_{uniform}$ for the double-sided case is 22.48dBi if we could completely suppress radiation from the bottom side.

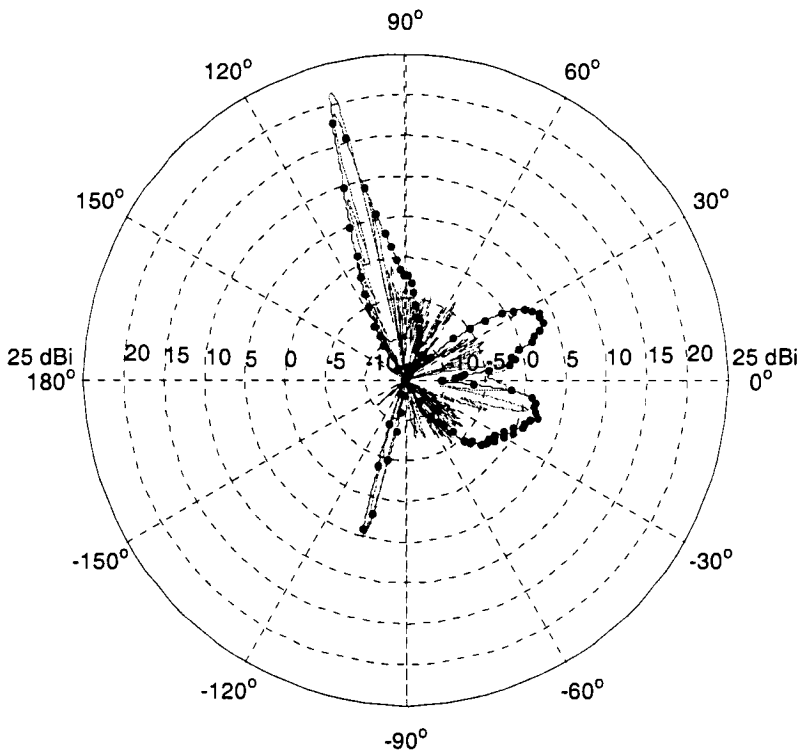

Figure 2.24 - Directivity of un-optimized (– • – • –) and optimized double-sided holograms (——), f=30GHz

Table 2.6 - Directivity of double-sided holograms for L = 280mm

Type of hologram	D [dBi]	Angle of D_{max} [degrees]	e_{ap} [%] with $D_{uniform}$ = 22.48dBi	Front-to-Back ratio [dB]
Free-space	14.2	78.6	14.6	8.7
New (case 3)	18.7	105.3	41.9	13.4
Optimized new	21.5	104.7	79.8	17.8

Table 2.7 - Directivity of double-sided holograms for L = 140mm

Type of hologram	Directivity [dBi]	Angle of D_{max} [degrees]	e_{ap} [%] with $D_{uniform}$ = 19.48dBi	Front-to-Back ratio [dB]
Free-space	11.74	78.5	16.8	8.4
New (case 3)	15.95	103	44.4	13.2
Optimized new	18.14	103.3	73.5	18.8

Figures 2.25-2.27 show the free-space, new, and optimized new double-sided hologram performances over a frequency band of 20-35GHz. One of the limitations in the free-space hologram is it does not work at the designed frequency of 30GHz when the substrate is thick. The best operation of the hologram has changed to about 25GHz where the strip spacings $\approx \lambda_g$ of the lower frequency, but even the directivity at 25GHz is still not as good as the new double-sided holograms.

The large "jump" in the angle of maximum directivity in Figure 2.26 is due to grating lobes, which occurs when the distance between the strips is larger than λ_g at the observed frequencies, this then causes the directivity to decrease drastically to the point where the directivity of the desired beam is now lower than that of the endfire beam.

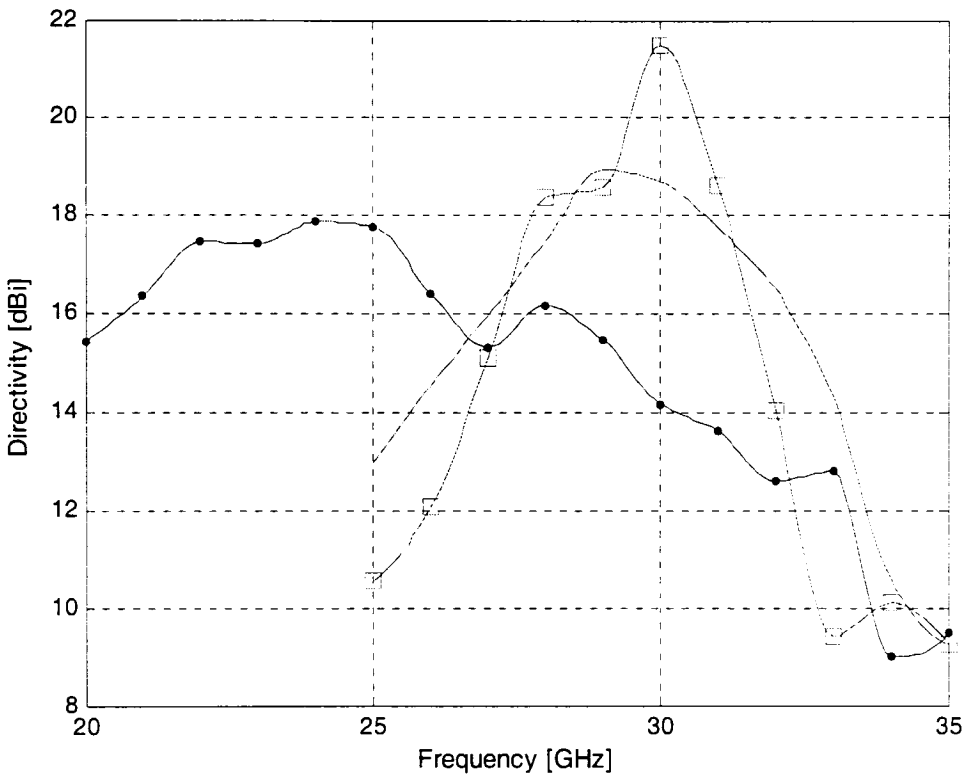

Figure 2.25 - Directivity of free-space (— • — • — • —), new (————————), and optimized new double-sided antennas (— □ — □ — □ —), L = 280mm

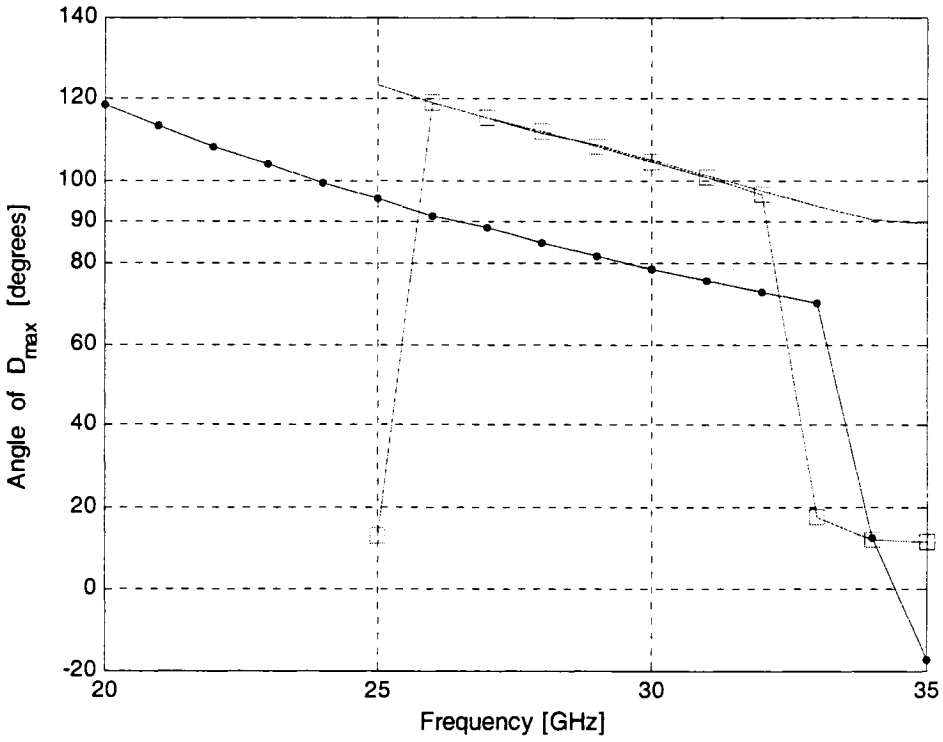

Figure 2.26 - Angles of directivity of free-space (— • — • — • —), new (————————), and optimized new double-sided antennas (— □ — □ — □ —), L = 280mm

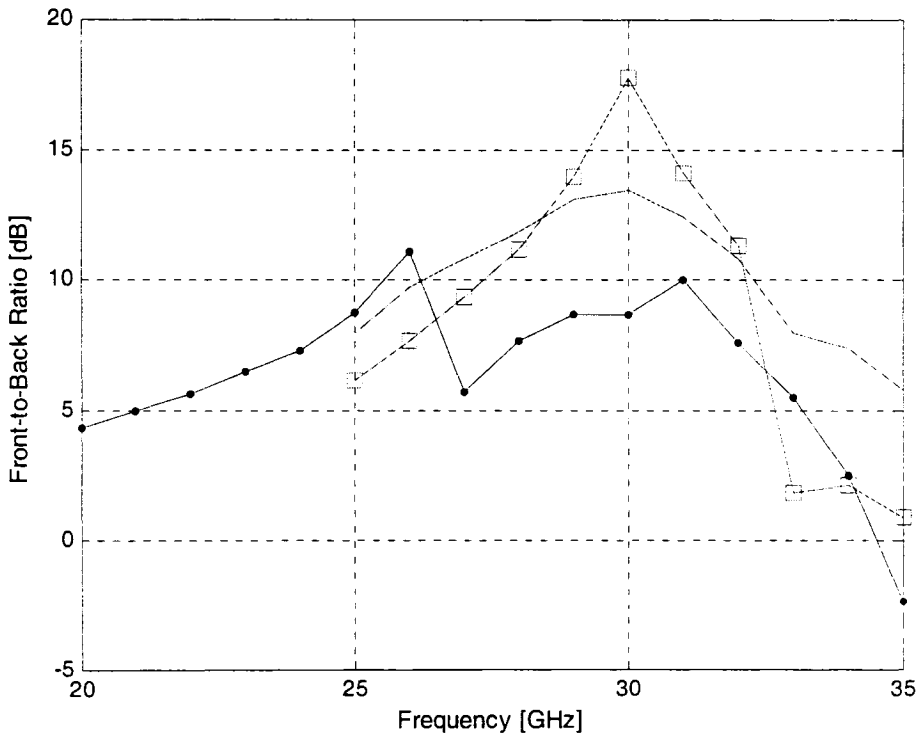

Figure 2.27 - Front-to-Back ratio of free-space (— • — • — • —), new (————————), and optimized new double-sided antennas (— □ — □ — □ —), L = 280mm

2.4 Holographic Antennas Using a Grounded Dielectric Substrate

Previous single beam holographic antennas studied in [2-4] used the free-space double-sided hologram or double-layer hologram to reduce the bottom lobe. Both holograms are essentially arrays of single-sided holograms. A ground plane could not be placed on the bottom side of the free-space holograms to suppress the bottom beam because the free-space interference pattern could not model the effect of the ground plane. However, by including the presence of the ground plane in the computation of the interference pattern we can realize a hologram with a ground plane and produce single beam radiation. The procedure to synthesize this hologram is the same as the true interference pattern of case 3 in Section 2.1.4 except a grounded substrate is used instead of the usual substrate. That is, (a) the field due to the reference wave is determined in the presence of the grounded substrate without the plane wave source, (b) the field due to the plane wave is determined in the presence of the grounded substrate without the feed horn, and finally the interference pattern is sum of the two fields determined in steps (a) and (b). Unlike the dielectric slab which has a cutoff frequency of zero, the grounded substrate has a cutoff frequency given by

$$f_c = \frac{(2n-1)c}{4t\sqrt{\varepsilon_r - 1}} \tag{2.4}$$

where t is the substrate thickness, c = $3\text{x}10^8$ m/s, n = 1, 2, 3, ... for the TE_n modes [15]. The TE_1 cutoff frequency for t = [0.508, 1.36, 2] mm is [95.7, 35.8, 24.3] GHz. Figure 2.28 shows the radiation patterns for the free-space hologram with/without the ground plane where t = 0.508mm, and f = 30GHz. The inclusion of the ground plane on the bottom side of the thin free-space hologram ruined the desired radiation pattern because the grounded substrate is in cutoff and does not allow the incident field to propagate along the substrate (which is necessary for the strips to scatter the incident wave to form a beam in an intended direction). By using a 2mm thick grounded substrate, we are now in the guided mode of the grounded slab and Figure 2.29 compares the radiation pattern of this grounded substrate hologram using the true interference pattern to that using the free-space interference pattern. And, using the usual optimization procedure the hologram improved by 2.5dB, as shown in Figure 2.30 and Table 2.8. Although the front-to-back ratio of the grounded-substrate

hologram is better than that of the double-sided hologram, there is still radiation on the bottom side of the grounded-substrate hologram due to radiation from the horn scattering off the grounded-substrate.

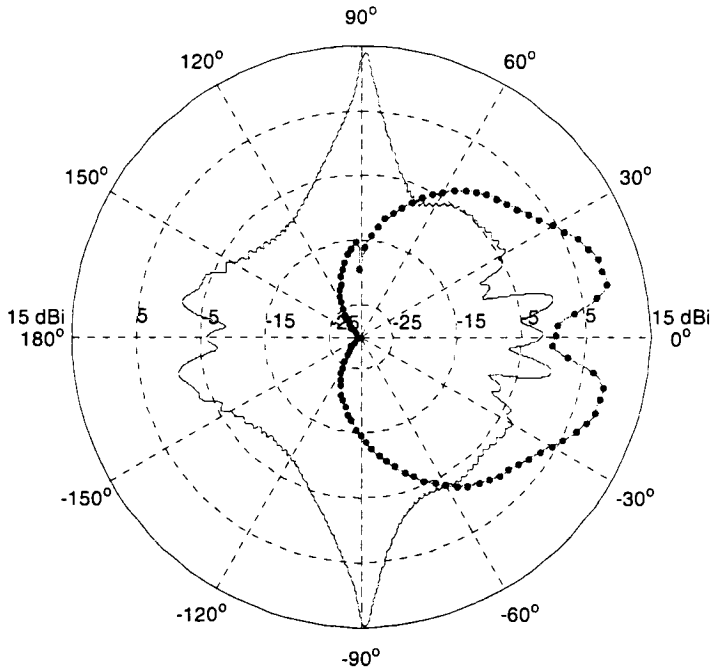

Figure 2.28 - Directivity of the free-space hologram (————————), free-space hologram with a ground plane (— • — • — • —), t = 0.508mm, f=30GHz for both cases

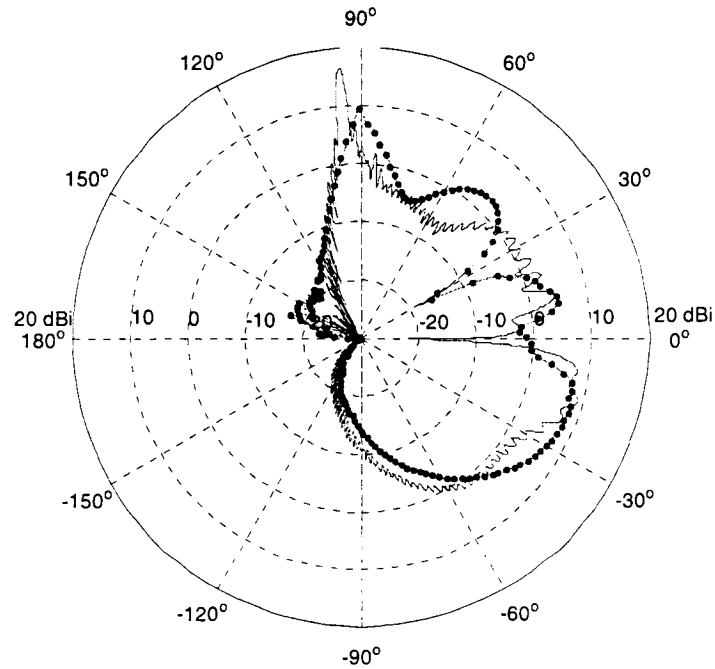

Figure 2.29 - Directivity of the free-space antenna (— • — • — • —), holographic antenna using a grounded substrate (————————), t = 2mm, f=30GHz for both cases

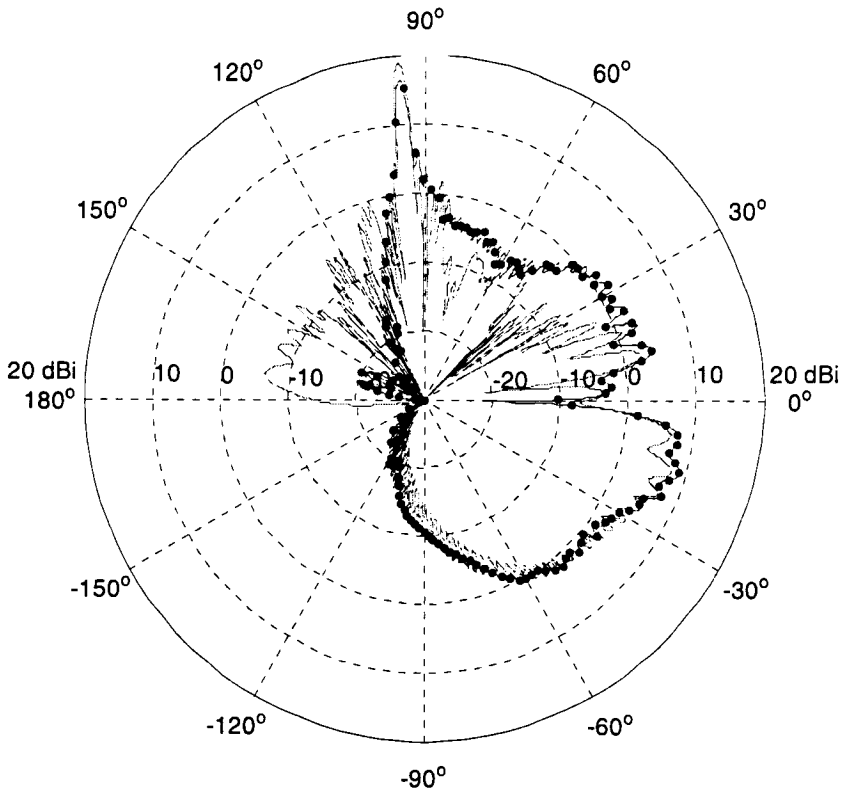

Figure 2.30 - Directivity of the un-optimized (— • — • — • —), and optimized antennas (————— —) using a grounded substrate, t = 2mm, f=30GHz both cases

Table 2.8 - Directivity of various holograms for L = 280mm

Type of hologram	D [dBi]	Angle of D_{max} [degrees]
Free-space grounded slab	9.3	90.2
Free-space single-sided	14.9	-89.1
New grounded slab	**16.5**	**94.6**
Optimized new grounded slab	**19**	**94.6**
New single-sided (case 3 in Section 2.1.4)	16.8	-92.6
Optimized new single-sided (case 3 in Section 2.1.4)	18.6	-92.1
New double-sided	18.7	105.3
Optimized new double-sided	21.5	104.7
New double-sided with L = 140mm	16	103
Optimized new double-sided with L = 140mm	18.1	103.3

Based on Table 2.8, for a fixed substrate length the grounded substrate antenna has comparable performance to the single-sided antenna. The directivity of the grounded substrate hologram is lower than that of the double-sided hologram because the double-sided hologram has two sets of strips where each set of strips is designed to scatter the incident

field in an intended direction whereas the ground plane does not scatter in an intended direction. The advantage with the grounded slab antenna is the bottom lobe will be suppressed at any frequency, while the double-sided antenna can only suppress the bottom lobe over a range of frequency and has poorer front-to-back ratio than the grounded slab antenna. Therefore, if the length of the antenna is a constraint then using the double-sided antenna will give higher directivity than the grounded substrate antenna. Otherwise, the grounded substrate antenna can offer comparable performance to the double-sided antenna of shorter length with complete suppression of the bottom lobe.

2.5 Observation of the Power Density in the Dielectric Substrate With/Without a Ground Plane

To observe the flow of energy and the influence of the substrate on the antenna we will observe the power density throughout the substrate. The structure of interest is the same as that in Figure 2.4 except only the horn antenna is used to excite the substrate. The real part of the complex Poynting vector represents real power transported per unit area [19], where

$$\underline{S}_{ave} = \frac{1}{2}\mathrm{Re}\left\{\underline{E}\times\underline{H}^{*}\right\} = \hat{x}S_{ave,x} + \hat{y}S_{ave,y} \tag{2.5}$$

The main component of interest is the power flow along the axial direction so we will be observing $\hat{x}\bullet\underline{S}_{ave} = \hat{x}S_{ave,x}$ throughout the substrate. Also, the $\hat{y}$-component of $\underline{S}_{ave}$ is very small compared to $\hat{x}S_{ave,x}$ since the horn is oriented in the x-direction.

With $S_{ave,x} = -\frac{1}{2}\mathrm{Re}\left\{E_z H_y^{*}\right\}$, the electric field external to the substrate is

$$E_z^{ext}(x,y) = E_z^{inc}(x,y) + E_z^{ext,scat}(x,y) \tag{2.6}$$

where the incident field due to a line source located at (x_{LS}, y_{LS}) is

$$E_z^{inc} = \frac{-k_o\eta_o}{4}H_o^{(2)}\left(k_o\left|\underline{\rho}-\underline{\rho}_{LS}\right|\right) \tag{2.7}$$

with $k_o = \omega\sqrt{\mu_o\varepsilon_o}$, and $\eta_o = \sqrt{\mu_o/\varepsilon_o}$. The external scattered field is

$$E_z^{ext,scat} = \frac{-k_o\eta_o}{4}\int_C \hat{g}(\underline{\rho}')H_o^{(2)}\left(k_o\left|\underline{\rho}-\underline{\rho}'\right|\right)dt' \tag{2.8}$$

where $\underline{\rho}'$ is the segment coordinates on the substrate and horn surfaces, and $\hat{g}(\underline{\rho}')$ is the external equivalent current on the surface of interest from the moment method solution [5]. The field inside the substrate region is $E_z^{\text{int}}(x,y) = E_z^{\text{int,scat}}(x,y)$, with

$$E_z^{\text{int,scat}} = \frac{-k\eta}{4}\int_C \hat{f}(\underline{\rho}')H_o^{(2)}\left(k\left|\underline{\rho}-\underline{\rho}'\right|\right)dt' \tag{2.9}$$

where $\hat{f}(\underline{\rho}')$ is the internal equivalent current on the substrate and horn surfaces. The total magnetic field is $H_y(x,y) = \frac{1}{j\omega\mu_o}\frac{\partial E_z(x,y)}{\partial x}$ and the incident magnetic field is

$$H_y^{inc} = \frac{k_o}{4j}\frac{(x-x_{LS})}{\sqrt{(x-x_{LS})^2+(y-y_{LS})^2}}H_1^{(2)}\left(k_o\sqrt{(x-x_{LS})^2+(y-y_{LS})^2}\right) \tag{2.10}$$

As we move the observation point closer to the source, whether it is the line source or equivalent current segment, $H_1^{(2)}(\arg)$ "blows up" much quicker than $H_o^{(2)}(\arg)$ as $\arg \to 0$. Therefore we will use a singularity extraction technique to let us observe the field close to the surface of interest by modifying the terms for the external and internal scattered magnetic field [11]. The small argument of $H_1^{(2)}(\arg)$ is $H_1^{(2)}(\arg)\xrightarrow[\arg\to 0]{}\frac{2j}{\pi\arg}$. The external magnetic field is $H_z^{ext}(x,y) = H_z^{inc}(x,y) + H_z^{ext,scat}(x,y)$ where the external scattered magnetic field is given by

$$H_y^{ext,scat} = \int_C\left[\hat{g}(\underline{\rho}')\frac{k_o}{4j}\frac{(x-x')}{\left|\underline{\rho}-\underline{\rho}'\right|}H_1^{(2)}\left(k_o\left|\underline{\rho}-\underline{\rho}'\right|\right) - \frac{2j}{\pi k_o\left|\underline{\rho}-\underline{\rho}'\right|}\right]dt' + \int_C\frac{2j}{\pi k_o\left|\underline{\rho}-\underline{\rho}'\right|}dt' \tag{2.11}$$

The small argument was subtracted from $H_1^{(2)}\left(k_o\left|\underline{\rho}-\underline{\rho}'\right|\right)$ to make it numerically stable and the second integral of (2.11) can be evaluated analytically to avoid the singularity problem. Similarly, the internal magnetic field is $H_y^{\text{int}}(x,y) = H_y^{\text{int,scat}}(x,y)$,

$$H_y^{\text{int,scat}} = \int_C\left[\hat{f}(\underline{\rho}')\frac{k}{4j}\frac{(x-x')}{\left|\underline{\rho}-\underline{\rho}'\right|}H_1^{(2)}\left(k\left|\underline{\rho}-\underline{\rho}'\right|\right) - \frac{2j}{\pi k\left|\underline{\rho}-\underline{\rho}'\right|}\right]dt' + \int_C\frac{2j}{\pi k\left|\underline{\rho}-\underline{\rho}'\right|}dt' \tag{2.12}$$

The fundamental cutoff frequency for a dielectric slab waveguide is zero so the slab will support a guided mode for any thickness and frequency. Therefore even when the substrate is

electrically thin, such as that used in the single-sided hologram, a guided mode is always present where the power density is higher inside the slab, as shown in Figure 2.31. The standing wave pattern in the substrate region is caused by the finite substrate length. Although the incident power from the horn antenna is being guided by the thin substrate, it did not couple strongly into the substrate since the power density along the slab boundaries (at y = +/- 0.254mm) in the axial direction is still greater than -2dB. Figure 2.32 shows $S_{ave.x}$ for the grounded dielectric slab of 0.508mm thick with the ground plane at y = -0.254mm. At 30GHz, this structure is in cutoff and the grounded slab is acting as a spatial high-pass filter which blocks the field from propagating along the slab. And without the incident power, the strips cannot scatter the incident wave to form a broadside beam shown earlier in Figure 2.28. Figure 2.33 shows the electric field throughout the grounded slab from a "zoomed out" point of view where we can observe this blocking action in the cutoff mode compared to the field throughout a substrate without the ground plane of Figure 2.34. Since the field could not travel along the axial direction, it scattered at an angle from the grounded slab to produce beams at around +/-15° that can be seen in the radiation pattern of Figure 2.28.

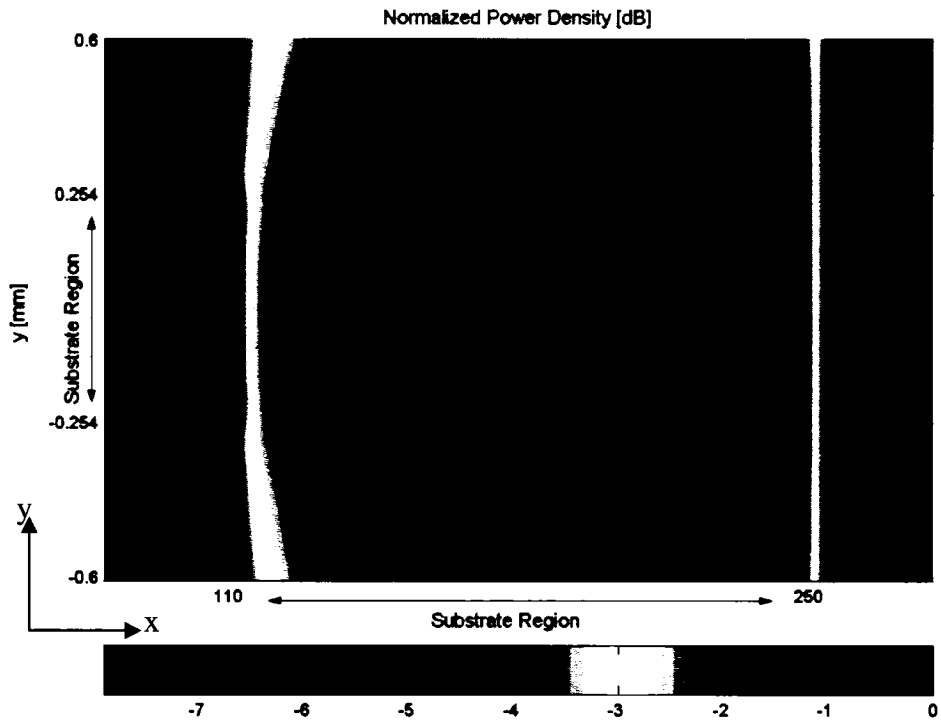

Figure 2.31 - Normalized power density of a 0.508mm thick substrate, the slab exists from x = 110 to 250mm, y = -0.254 to 0.254mm

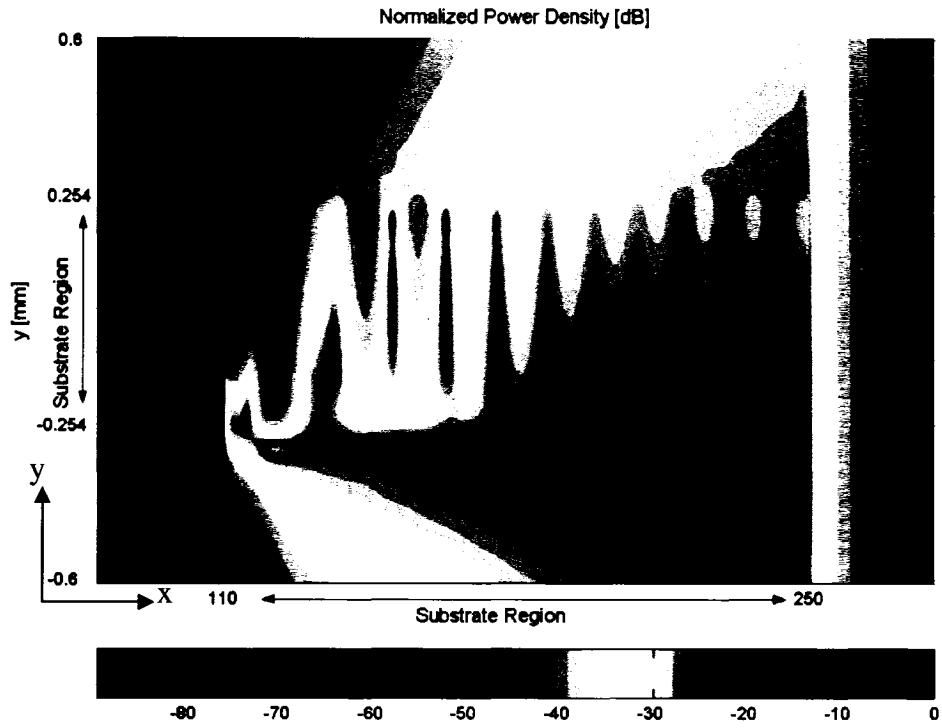

Figure 2.32 - Normalized power density of a 0.508mm thick grounded substrate, the slab exists from x = 110 to 250mm, y = -0.254 to 0.254mm, the ground plane is at y = -0.254mm

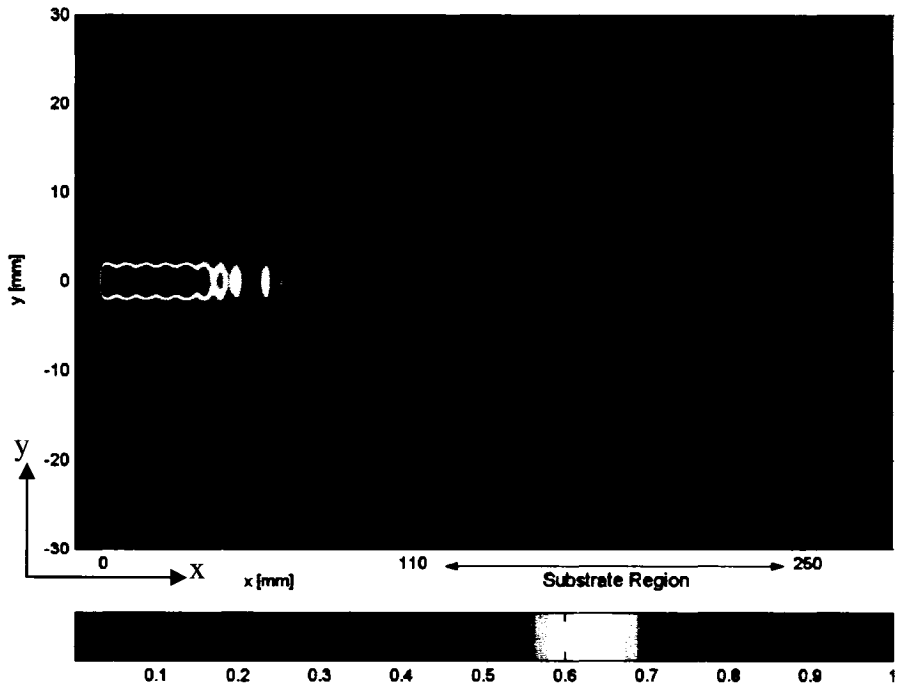

Figure 2.33 - Normalized electric field of a 0.508mm thick grounded substrate

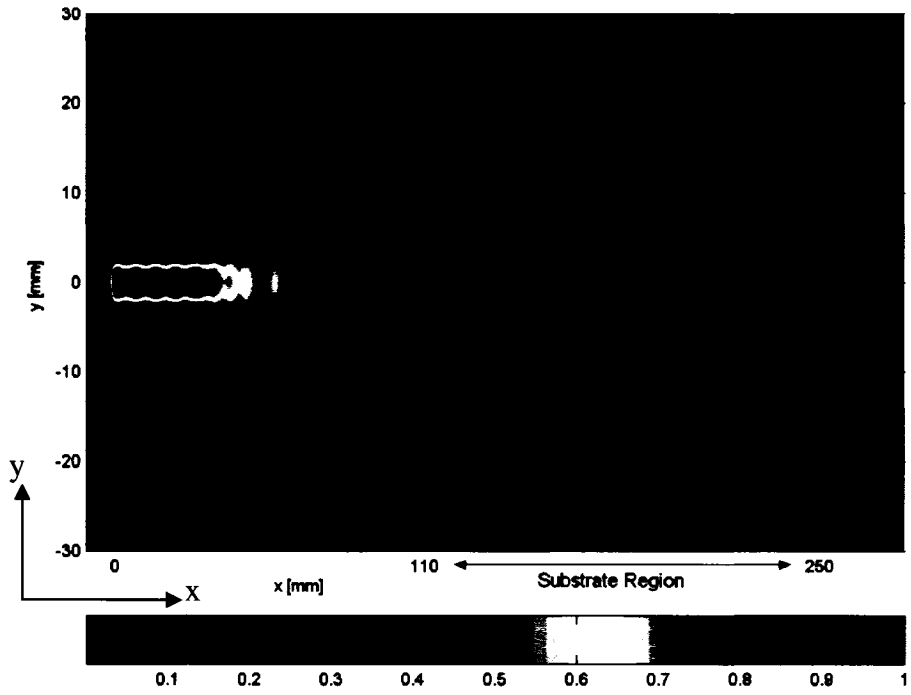

Figure 2.34 - Normalized electric field of a 0.508mm thick substrate

Figure 2.35 shows the power density throughout the 1.36mm thick substrate used in the double-sided hologram. The power density is more confined to the center since the slab is thicker than the 0.508mm slab but it is still high at around -3dB at the slab boundaries (y = +/- 0.68mm). This is could be why the offset spacing used in the double-sided holograms of $O = \lambda_o / 4$ produced better results than $O = \lambda_g / 4$. The power density of the grounded slab of 2mm thick is shown in Figure 2.36 where the slab is operating in a guided mode and we can observe a transfer of power along the slab. The ground plane is at y = -1mm and causes the power density to be near zero in the bottom substrate region.

Based on observations in this chapter, the operation of the holographic antenna is similar to a leaky-wave antenna where a guided wave is required and radiation is achieved by the strips scattering the guided power flowing along the slab.

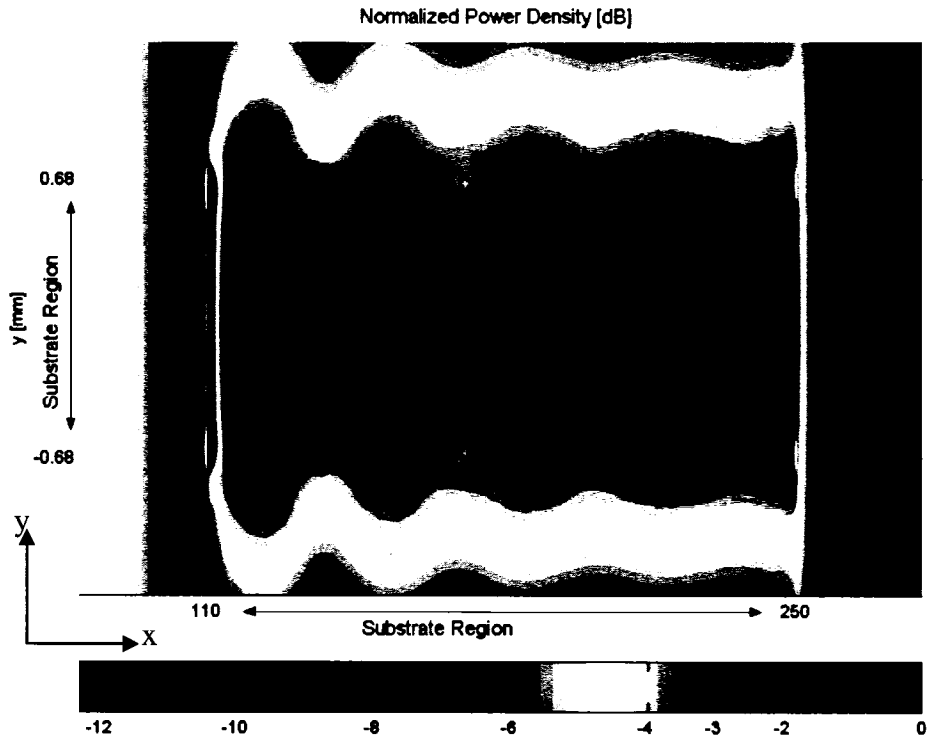

Figure 2.35 - Normalized power density of a 1.36mm thick substrate

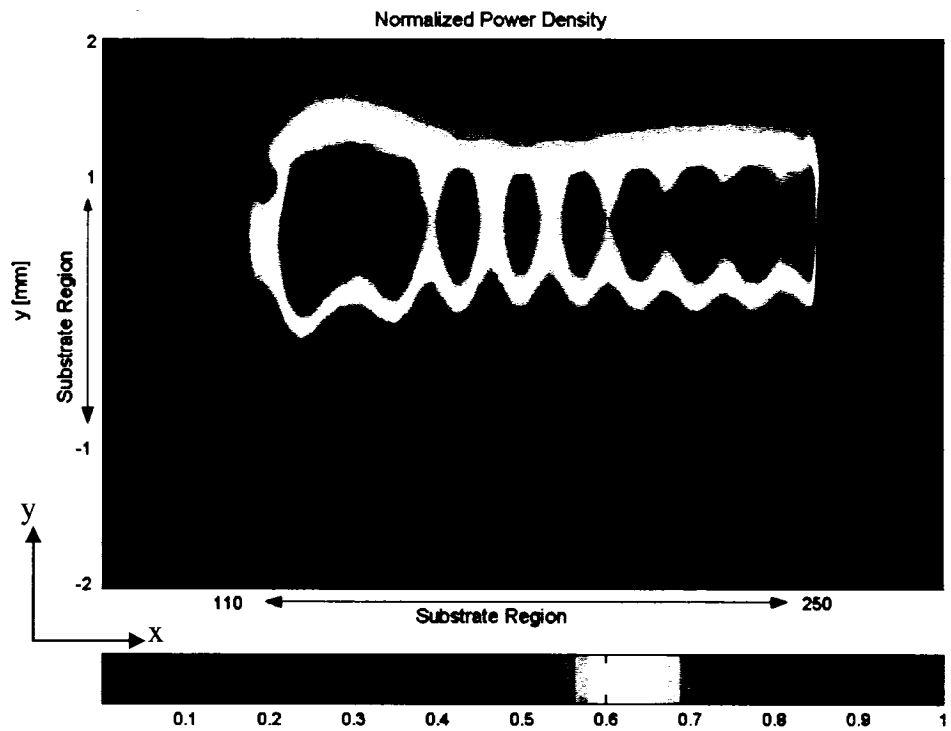

Figure 2.36 - Normalized power density of a 2mm thick grounded substrate

2.6 Analyzing the Relationship between the Strip Widths and the Antenna's Leakage Rate

From a two-dimensional point of view, the hologram is a uniform leaky-wave antenna where the aperture distribution, A(x), is related to the antenna's leakage rate, or radiation rate $\alpha(x)$, by

$$\alpha(x) = \frac{\frac{1}{2}|A(x)|^2}{\frac{1}{1-f_p}\int_0^L |A(x')|^2 dx' - \int_0^x |A(x')|^2 dx'} \tag{2.13}$$

where x is the axial direction, $f_p = P_{load}/P_{in}$ is the leftover power ratio, L is the substrate's length, and the antenna configuration is the same as that in Figure 2.1 but without the plane wave source [16]. The maximum achievable gain of an antenna is dependent on its aperture size, so if the antenna radiates too quickly along its length then the rest of the aperture will not be used to its full extent and increasing the aperture length will not increase the gain. Therefore the gain can be improved by reducing $\alpha(x)$ so that the end region of the hologram will be utilized. So far we have not considered the effect of the strip widths on the hologram, besides a short quantization test to differentiate between the higher and lower minima in Section 2.1.4, we will now use (2.13) to study the relationship between the strip width, w, and the antenna leakage rate, $\alpha(x)$. We will approximate the input power with

$P_{in} = \int_{-t/2}^{t/2} \frac{1}{2\eta_o} |E_z(x = \text{start of dielectric slab}, y')|^2 dy'$ and the power at the load with

$P_{load} = \int_{-t/2}^{t/2} \frac{1}{2\eta_o} |E_z(x = \text{end of dielectric slab}, y')|^2 dy'$. The 2-D radiation efficiency, e_{rad}, can be computed as $e_{rad} = \frac{P_{rad}}{P_{in}} = \frac{P_{in} - P_{load}}{P_{in}} = 1 - f_p$ and the 2-D gain is

$G = e_{rad} D = e_{rad} e_{ap} D_{uniform} = e_{total} D_{uniform}$. In this study the strip width, w, will be varied uniformly for all strips. As shown in Figure 2.37, the electric field is zero at a conducting surface and it will force the leakage rate to be zero there as well if we use the field distribution at the hologram's surface as A(x). This also makes $\alpha(x)$ fluctuates rapidly and

difficult to observe trends in $\alpha(x)$, consequently we will use the envelope of the field at the hologram's surface as A(x), as illustrated in Figure 2.38. Although $\alpha(x)$ looks like A(x), it does not necessarily have to resemble A(x) as we will see later on.

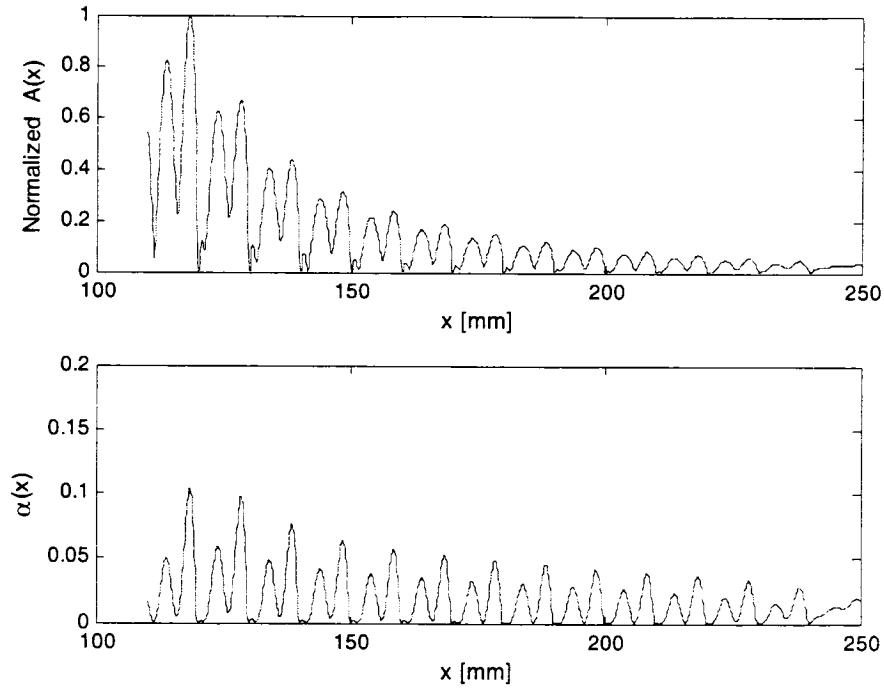

Figure 2.37 - Using the field distribution at the hologram's surface as A(x)

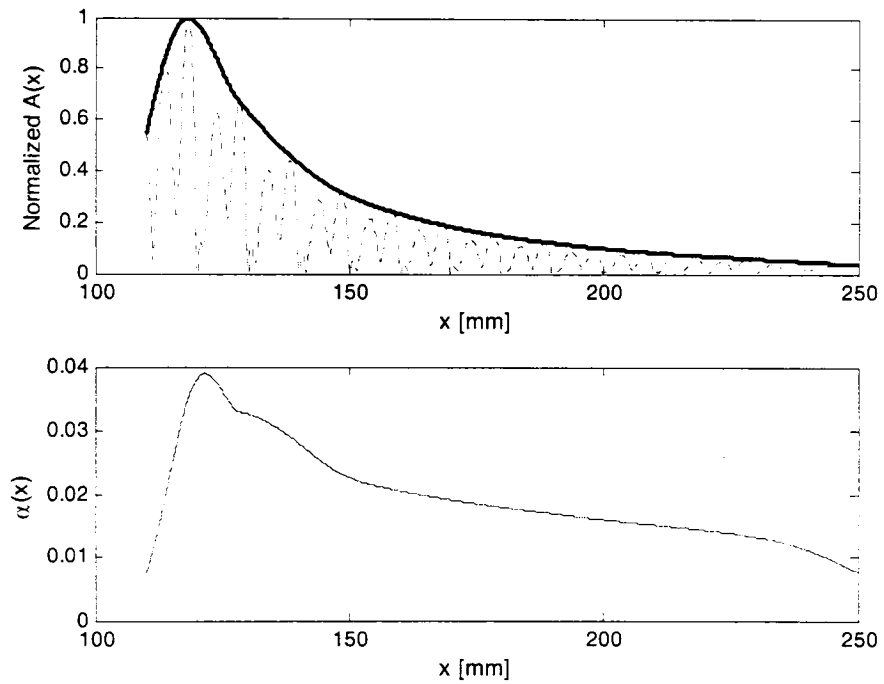

Figure 2.38 - Using the envelope of the field distribution at the hologram's surface as A(x)

2.6.1 Leakage Rate of Free-space Single-Sided Hologram

Table 2.9 and Figure 2.39 show the aperture distribution and leakage rate of the free-space hologram for various strip widths where the wider strips lead to a quicker decay in A(x), lower directivity, higher e_{rad}, and larger $\alpha(x)$. The amplitude of A(x) at the end of the substrate (x = 250mm) is proportional to the directivity of the endfire lobe and the leftover power ratio f_p. The same procedure was repeated for a longer substrate length of 280mm, as shown in Figure 2.40 and Table 2.10, to observe if $\alpha(x)$ can be extrapolated from $\alpha(x)$ of the shorter hologram. For most cases, $\alpha(x)$ of antennas using a periodic strip spacing could be approximated with $\alpha(x)$ of the shorter antennas as this provides a convenient approach for determining $\alpha(x)$ of antennas that are too electrically long.

One limitation with the free-space hologram is the directivity does not increase proportionally with an increase in aperture length. This is caused by the antenna radiating too quickly which then leads to a small percentage of power left at the end of the antenna. Therefore an increase in that aperture length will not improve the directivity but will decrease the aperture efficiency because the extra length is not being utilized. As observed in Table 2.10 (which repeats some data from Table 2.8 to enable easier comparison with the new data) for a configuration of L = 140mm, w = 0.254mm, the free-space hologram has radiated most of its power, so doubling the length did not increase the directivity by 3dB and the aperture efficiency decreased as a result under-utilizing the aperture. Although it is desirable to radiate all the input power for a fixed aperture length, we need to balance the radiation efficiency and aperture efficiency to operate at an optimal total efficiency where these two quantities are similar to balancing the spillover and taper efficiency in reflectors [13].

Table 2.9 - Efficiency of free-space holograms with L = 140mm, w = 0.127 to 1.016mm

w [mm]	D [dBi]	e_{rad} [%]	G [dBi]	f_p [%]	$D_{endfire}$ [dBi]	e_{ap} [%]	e_{tot} [%]
0.127	13.42	96	13.24	3.99	4.33	49.38	47.41
0.254	*13.34*	*98.87*	*13.29*	*1.13*	*2.94*	*48.92*	*48.37*
0.508	12.51	99.6	12.49	0.39	1.77	40.1	39.94
0.762	11.7	99.68	11.68	0.32	1.73	33.2	33.09
1.016	10.99	99.62	10.97	0.38	2.12	28.24	28.13

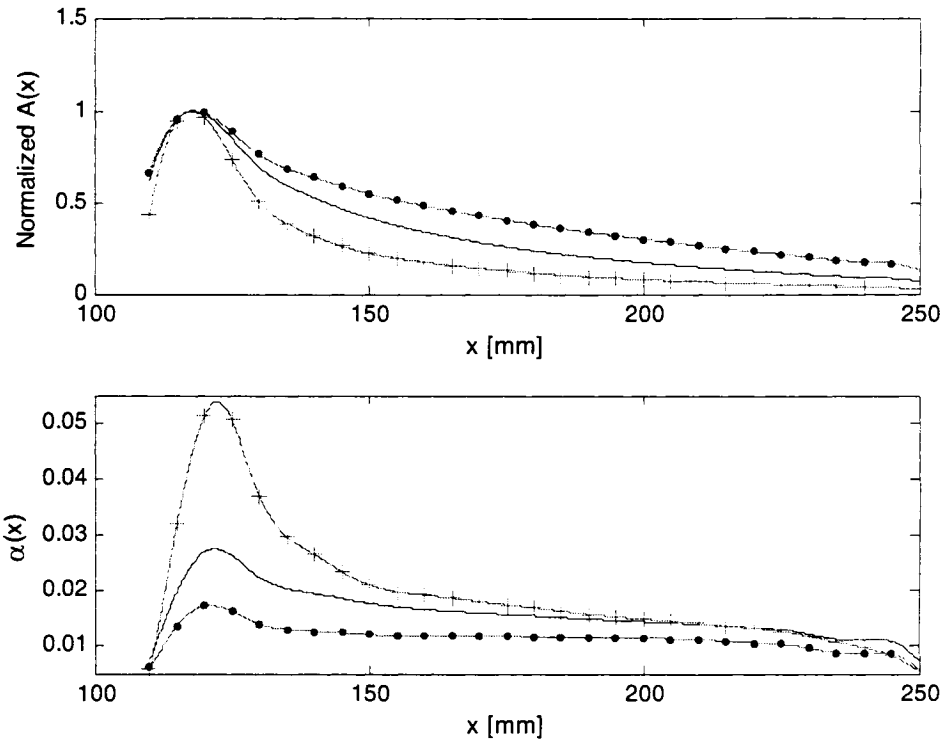

Figure 2.39 - Aperture distribution and leakage rate of the free-space holograms with w = 0.127mm (— • — • —), 0.254mm (————), and 1.016mm (— + — + —), L = 140mm, t = 0.508mm

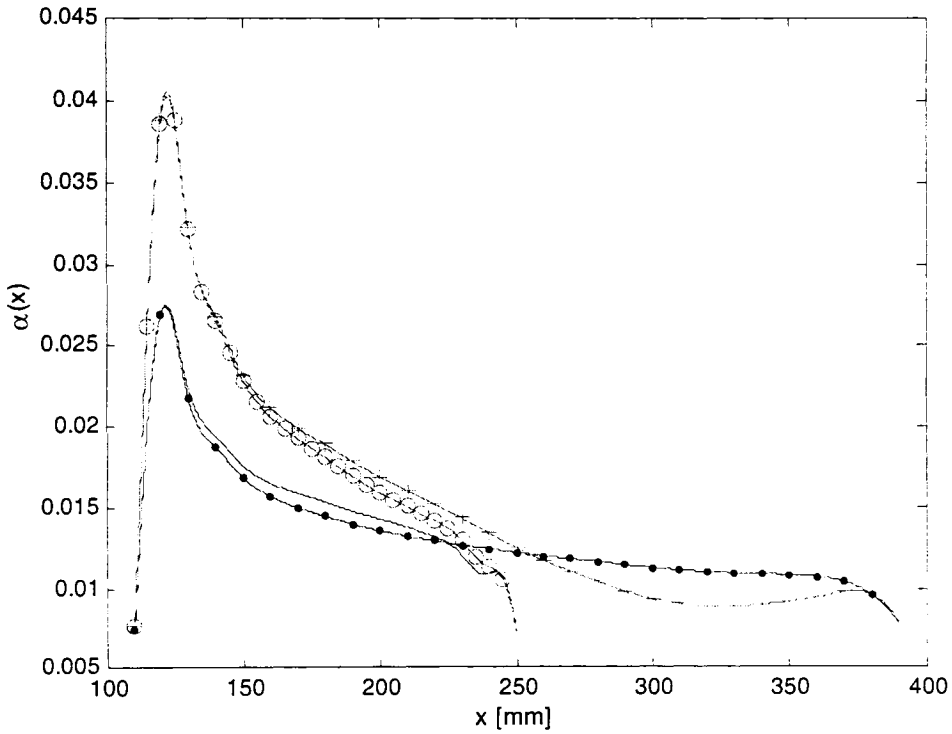

Figure 2.40 - Leakage rate of free-space holograms, L = 140mm with w = 0.254mm (————), 0.508mm (— O — O —); and L = 280mm with w = 0.254mm (— • — • —), 0.508mm (— + — + —)

Table 2.10 - Efficiency of free-space holograms with L = 140, 280mm, w = 0.127 to 0.508mm

L [mm]	w [mm]	D [dBi]	e_{rad} [%]	G [dBi]	f_p [%]	$D_{endfire}$ [dBi]	e_{ap} [%]	e_{tot} [%]
140	0.127	13.42	96	13.24	3.99	4.32	49.38	47.41
140	*0.254*	*13.34*	*98.87*	*13.29*	*1.13*	*2.94*	*48.92*	*48.37*
140	0.508	12.51	99.6	12.49	0.39	1.77	40.10	39.94
280	0.127	15.77	97.13	15.64	2.87	-3.78	42.52	41.3
280	*0.254*	*14.89*	*99.94*	*14.89*	*0.06*	*-1.37*	*34.31*	*34.29*
280	0.508	13.29	99.98	13.29	0.02	-1.91	24.05	24.05

2.6.2 Leakage Rate of New Single-Sided Hologram

The leakage rates for the new single-sided hologram with L = 140 and 280mm are shown in Figures 2.41, 2.42, and Table 2.11, 2.12, respectively. As illustrated in Figure 2.42, the leakage rates of the longer holograms are not similar to its shorter holograms because the strips are spaced randomly instead of periodically like the free-space hologram. Nevertheless, both of the free-space and new holograms show a common trend of poorer performance when the strip width increases.

Another way to visualize the advantage of using the true interference pattern to synthesize the hologram is its leakage rate is lower than that of the free-space hologram. This leads to more leftover power at the load for the case L = 140mm, so that an increase in aperture length to L = 280mm will increase the directivity and total efficiency. Plus, with optimization e_{tot} is much better than the free-space hologram of the same length, as shown in Figure 2.44 and Table 2.13. Of course, since the hologram was optimized at a strip width of 0.254mm, using any other strip width will decrease its optimal directivity.

Table 2.11 - Efficiency of new single-sided holograms, L = 140mm, w = 0.127 to 1.016mm

w [mm]	D [dBi]	e_{rad} [%]	G [dBi]	f_p [%]	$D_{endfire}$ [dBi]	e_{ap} [%]	e_{tot} [%]
0.127	13	83.71	12.23	16.29	9.28	44.94	37.62
0.254	*13.46*	*89.51*	*12.98*	*10.49*	*8.91*	*49.9*	*44.67*
0.508	13.42	94.16	13.16	5.84	7.92	49.41	46.52
0.762	12.63	97.33	12.52	2.67	6.42	41.25	40.15
1.016	11.55	98.83	11.49	1.17	4.66	32.1	31.72

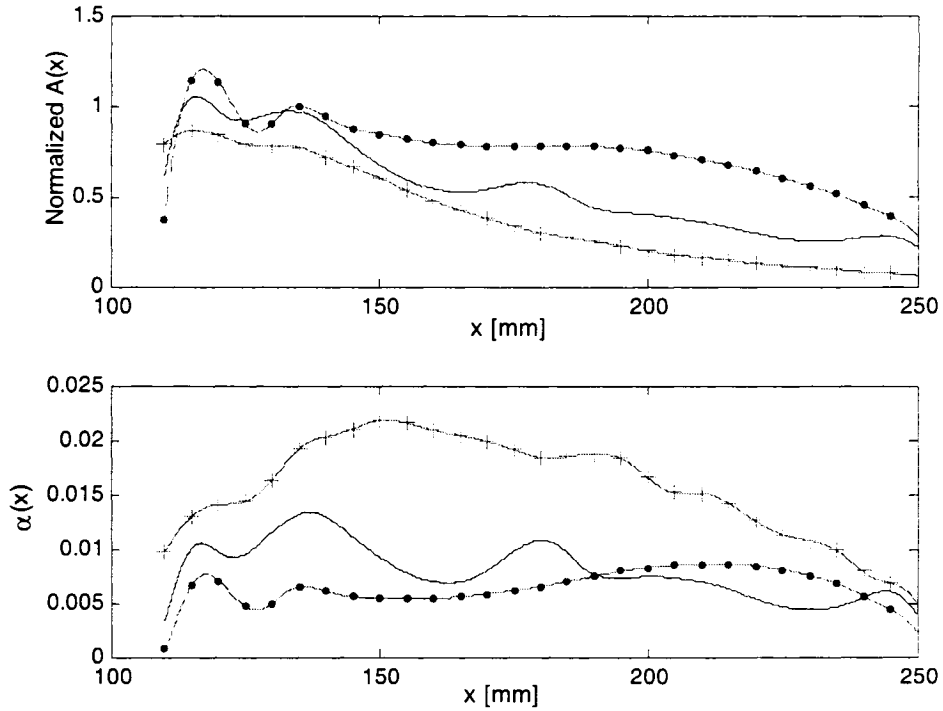

Figure 2.41 - Aperture distribution and leakage rate of the new single-sided holograms, L = 140mm, t = 0.508mm, w = 0.127mm (— • — • —), 0.254mm (————), and 1.016mm (— + — + —)

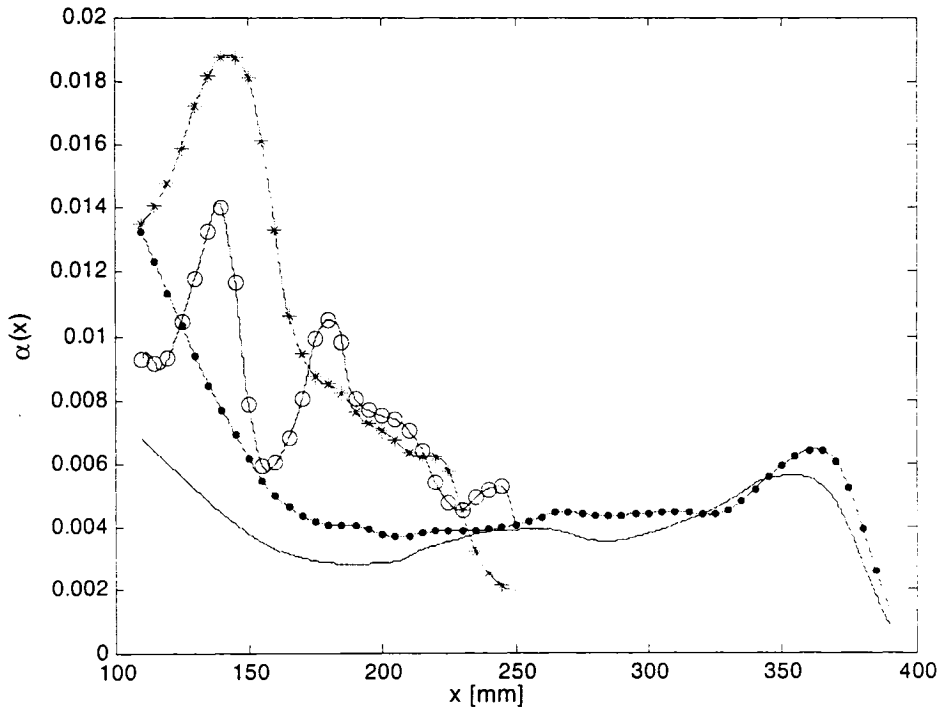

Figure 2.42 - Leakage rate of new single-sided holograms, L = 140mm with w = 0.254mm (— O — O —), 0.508mm (— * — * —); and L = 280mm with w = 0.254mm (————), 0.508mm (— • — • —)

Table 2.12 - Efficiency of new single-sided holograms with L = 140, 280mm, w = 0.127 to 0.508mm

L [mm]	w [mm]	D [dBi]	e_{rad} [%]	G [dBi]	f_p [%]	$D_{endfire}$ [dBi]	e_{ap} [%]	e_{tot} [%]
140	0.127	13.01	83.71	12.23	16.29	9.28	37.62	37.62
140	*0.254*	*13.46*	*89.51*	*12.98*	*10.49*	*8.91*	*44.67*	*44.67*
140	0.508	13.42	94.16	13.16	5.84	7.92	46.52	46.52
280	0.127	16.17	87.43	15.59	12.57	1.83	46.7	40.83
280	*0.254*	*16.84*	*89.48*	*16.36*	*10.52*	*5.74*	*54.45*	*48.72*
280	0.508	14.99	94.57	14.75	5.43	6.6	35.54	33.61

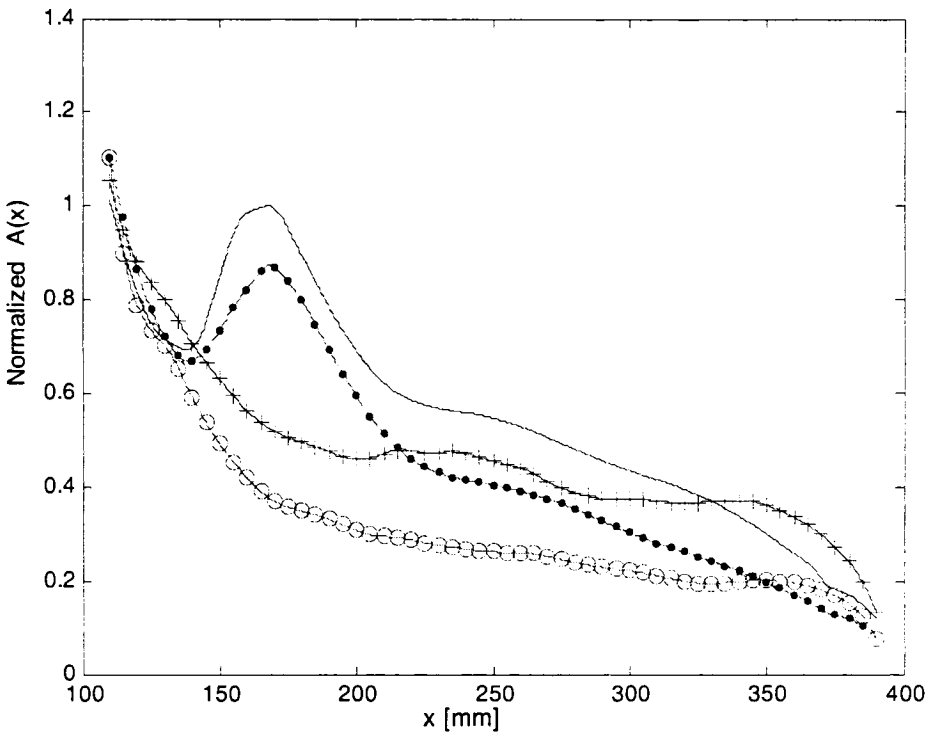

Figure 2.43 - Aperture distribution of new single-sided holograms with L = 280mm: un-optimized case with w = 0.254mm (— + — + —), 0.508mm (— O — O —); and optimized case with w = 0.254mm (——), 0.508mm (— • — • —)

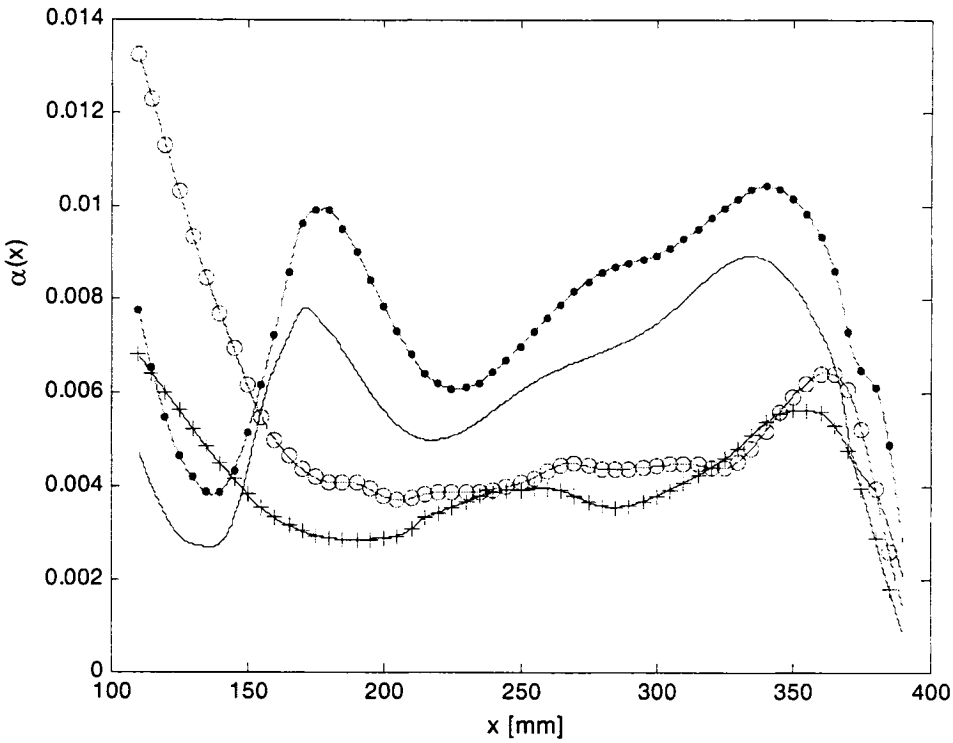

Figure 2.44 - Leakage rate of single-sided hologram with L = 280mm: un-optimized case with w = 0.254mm (—— + — + —), 0.508mm (— O — O —); and optimized case with w = 0.254mm (————), 0.508mm (—— • — • ——)

Table 2.13 - Efficiency of un-optimized and optimized single-sided holograms, w = 0.127 to 0.508mm, L = 280mm

	w [mm]	D [dBi]	e_{rad} [%]	G [dBi]	f_p [%]	e_{ap} [%]	e_{total} [%]
Optimized	0.127	18.12	94.39	17.87	5.61	73.14	69.04
Optimized	*0.254*	*18.6*	*96.71*	*18.06*	*3.29*	*81.7*	*79.01*
Optimized	0.508	16.74	98.64	16.67	1.357	53.16	52.44
Un-optimized	0.127	16.17	87.43	15.59	12.57	46.7	40.83
Un-optimized	*0.254*	*16.84*	*89.48*	*16.36*	*10.52*	*54.45*	*48.72*
Un-optimized	0.508	14.99	94.57	14.75	5.43	35.54	33.61

2.6.3 Leakage Rate of New Double-Sided Hologram

The leakage rates for the new double-sided hologram are shown in Figures 2.45-46 and Table 2.14 for L = 140 and 280mm, respectively. The leakage rate follows the same trend as the single-sided hologram because the strips are spaced randomly according to their interference pattern.

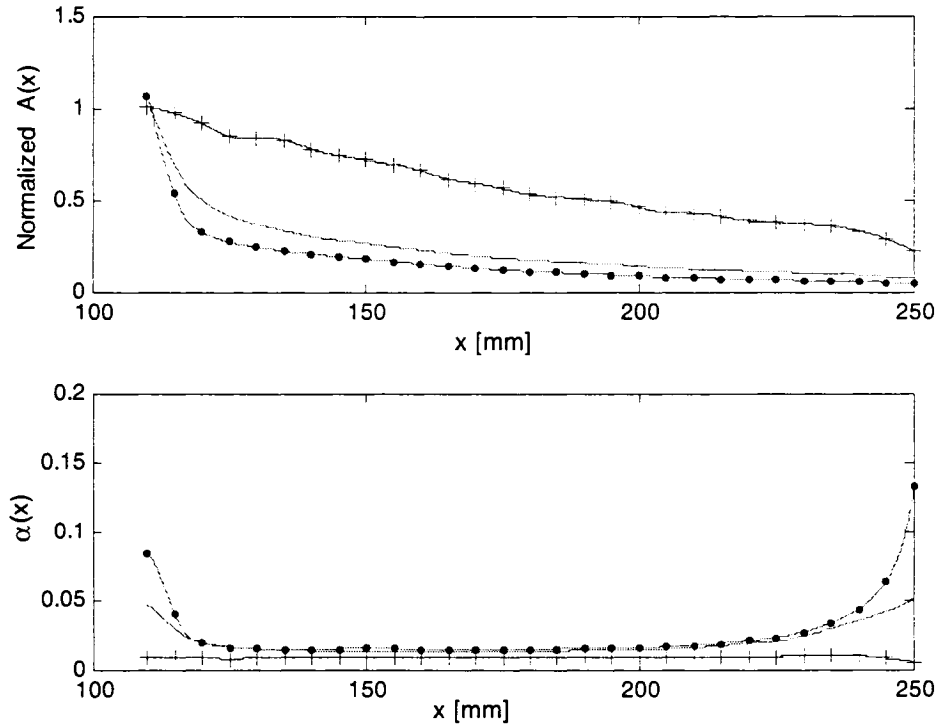

Figure 2.45 - Aperture distribution and leakage rate of new double-sided holograms, L = 140mm, t = 1.36mm, w = 0.127mm (—— • — • ——), 0.254mm (—— + — + —), and 0.508mm (——————)

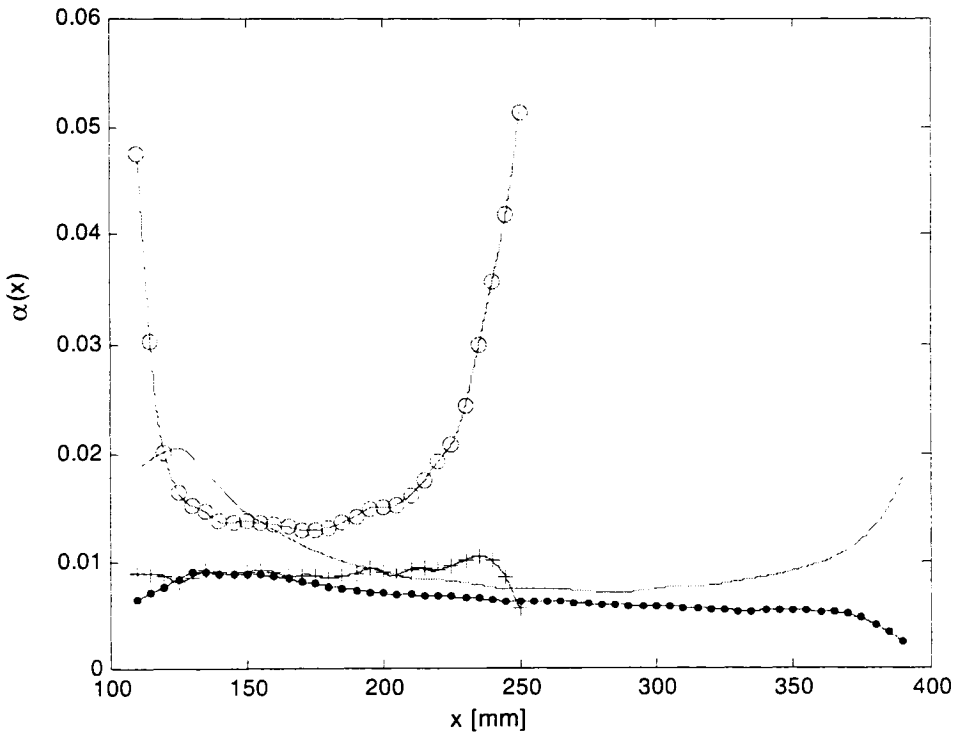

Figure 2.46 - Leakage rate of double-sided hologram, L = 140mm: w = 0.254mm (—— + — + —), 0.508mm (— O — O —); and L = 280mm with w = 0.254mm (—— • — • ——), 0.508mm (———)

Table 2.14 - Efficiency of double-sided holograms with L = 140, 280mm, w = 0.127 to 0.508mm

L [mm]	w [mm]	D [dBi]	e_{rad} [%]	G [dBi]	f_p [%]	e_{ap} [%]	e_{tot} [%]
140	0.127	8.55	99.87	8.55	0.13	8.07	8.06
140	*0.254*	*15.95*	*91.96*	*15.58*	*8.04*	*44.4*	*40.83*
140	0.508	10.82	99.56	10.8	0.44	13.6	13.54
280	0.127	18.43	98.12	18.35	1.88	39.39	38.65
280	*0.254*	*18.7*	*97.35*	*18.75*	*2.66*	*41.9*	*40.79*
280	0.508	13.42	99.72	13.41	0.26	12.42	12.39

As demonstrated in these cases, increasing the strip width will increase the leakage rate and decrease the directivity for any type of holograms. In most cases the initial strip width of 0.254mm has the best performance.

2.6.4 Leakage Rate Comparison of All Antennas Using w = 0.254mm

The leakage rate of all holograms using L = 140, 280mm are compared in Tables 2.15, 2.16 and Figures 2.47, 2.48, respectively. As stated earlier the free-space hologram suffers from lower aperture efficiency due to its high $\alpha(x)$. By reducing $\alpha(x)$, as achieved by the double-strips in the new holograms, we were able to achieve higher gain at a longer substrate length. The trend in $\alpha(x)$ is useful for antennas using a periodic strip spacing, but is not too useful for holograms using randomly spaced strips. Particularly the trend of increasing $\alpha(x)$ will decrease the directivity does not apply to the optimized antennas. Usually in the periodic-strip antennas, when $\alpha(x)$ increases e_{rad} will increase, e_{ap} will decrease and we have to balance these two efficiencies to maximize e_{tot}, but with the optimized antennas (using random strip positions) we are able to increase e_{rad} and e_{ap} simultaneously which contrasts the trend of the periodic-strip antennas. Changing the uniform strip spacing will not change the usual trend in $\alpha(x)$, and the only way to balance e_{rad}, e_{ap} when the strip width is fixed is to place the strips randomly via optimization as demonstrated in the optimized free-space single-sided hologram in Section 2.1.4 where 13 of the 27 strips ended up within 1mm of the strip positions of the new optimized single-sided hologram. Although (2.13) is a useful tool for relating A(x) to $\alpha(x)$, it is mainly applicable to uniform antennas whose cross-sections

are constant along the axial direction. The three-dimensional hologram cross-section varies continuously along the axial direction so it would be undesirable to use (2.13) in the 3-D analyses.

Table 2.15 - Efficiency of holograms with L = 140mm, w = 0.254mm

Type of hologram	D [dBi]	e_{rad} [%]	G [dBi]	f_p [%]	e_{ap} [%]	e_{tot} [%]
Free-space	13.34	98.87	13.29	1.13	48.92	48.37
Single-sided	13.46	89.51	12.98	10.49	44.67	44.67
Double-sided	15.95	91.96	15.58	8.04	44.4	40.83
Optimized double-sided	18.14	95.19	17.93	2.65	73.5	69.96

Table 2.16 - Efficiency of holograms with L = 280mm, w = 0.254mm

Type of hologram	D [dBi]	e_{rad} [%]	G [dBi]	f_p [%]	e_{ap} [%]	e_{tot} [%]
Free-space	*14.89*	*99.94*	*14.89*	*0.06*	*34.31*	*34.29*
Single-sided	*16.84*	*89.48*	*16.36*	*10.52*	*54.45*	*48.72*
Optimized single-sided	*18.6*	*96.71*	*18.08*	*3.29*	*81.7*	*79.01*
Double-sided	*18.7*	*97.35*	*18.75*	*2.66*	*41.9*	*40.79*

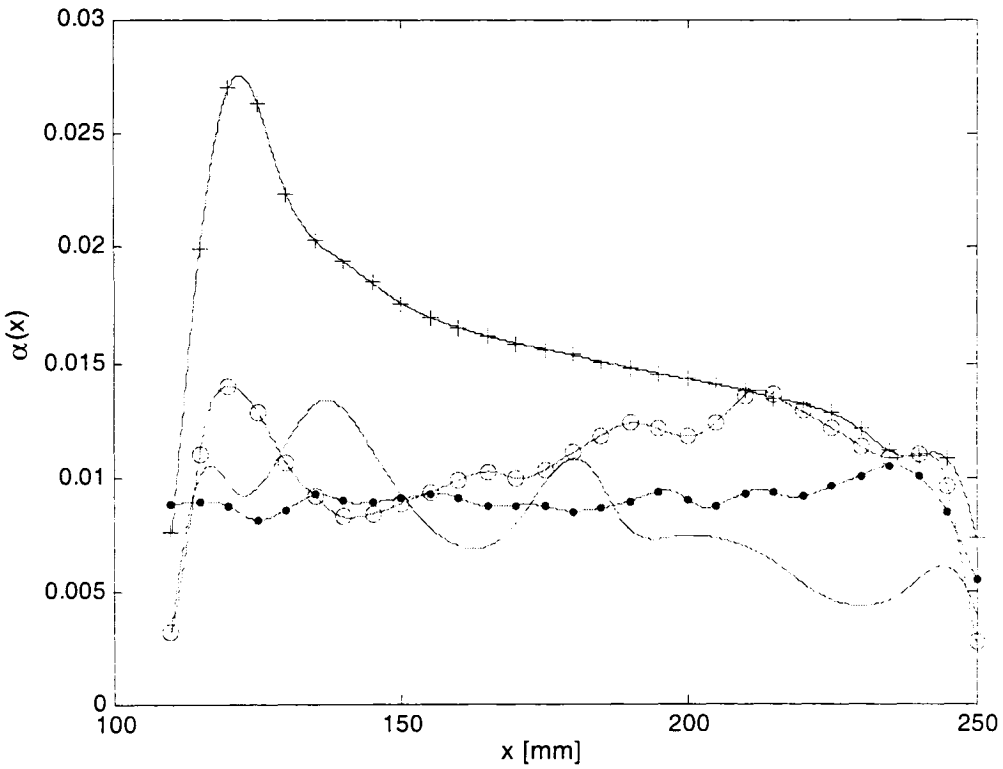

Figure 2.47 - Leakage rates for various holograms: free-space (— + — + —), single-sided (————), double-sided (— • — • —), optimized double-sided (— O — O —), w = 0.254mm, L = 140mm for all cases

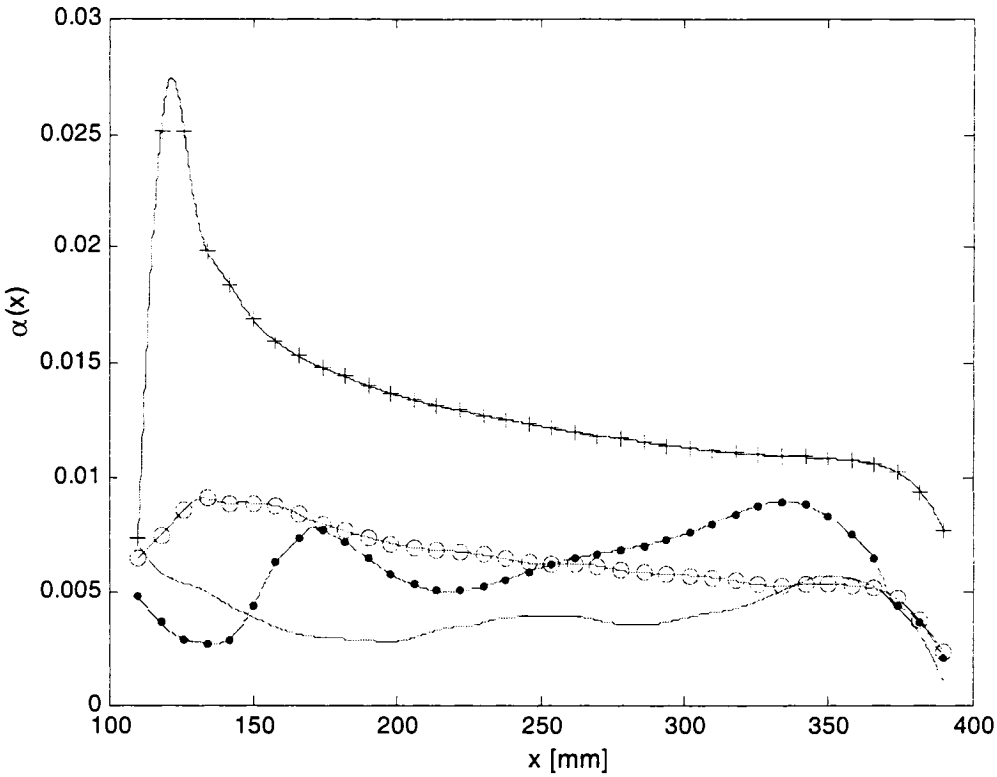

Figure 2.48 - Leakage rates for various holograms: free-space (—— + — + —), single-sided (————), optimized single-sided (— • — • —), double-sided (— O — O —), w = 0.254mm, L = 280mm for all cases

2.7 Summary of the Two-Dimensional Holographic Antenna Investigation

Initially in Section 2.1, we studied the true interference pattern by using the horn antenna as the reference source and included the presence of the dielectric substrate. Double-minima was observed in the interference patterns that contained a substrate of finite length for sources of any complexity. To more finely quantize this behaviour, we placed pairs of strips at the double-minima locations to maximize the directivity, i.e. placed strips at all minima instead of just at the lower minima. Although the beam shifted off broadside when the directivity is maximized, this is acceptable in practice. It was shown in Section 2.1.4 that this beam shift is not simply due to the location of the strips relative to the forward traveling wave from the source. We conjecture that it is due to the presence of the reflected (and hence standing) wave in the substrate, as well as mutual coupling between the strip pairs.

We then synthesized the double-sided hologram by using two sets of strips placed on a substrate with a thickness of $\lambda_g/4$ in Section 2.3. The top set of strips was placed according to the minima positions of the interference pattern observed at the top surface. The bottom set used the same strip spacing but shifted $\lambda_o/4$ with respect to the top strips to create at 180^o phase difference that will reduce the bottom lobe. It was during this part of the study that we realized the amplitude of the sources needs to be varied during the recording stage of the interference pattern in order to produce the double-minima behaviour and maximize the directivity. The optimal amplitude values were then determined using numerical experimentation and are dependent on the substrate thickness. Further reading revealed that similar "trial and error" is needed in making good optical holograms, although this is seldom shown in the literature.

Previously, a ground plane could not be used in holographic antennas because the effect of the ground plane could not be modelled by the analytical free-space interference pattern. But by including the presence of the ground plane in the computation of the interference pattern and varying the sources' amplitude, we were able to synthesize a grounded dielectric slab hologram that suppressed the bottom lobe and achieved high directivity in Section 2.4. When the antenna length is not a constraint then the grounded substrate hologram can offer comparable directivity to the single-sided hologram with the additional advantage of suppressing the bottom beam over all frequencies. The double-sided hologram is preferable to the grounded slab hologram when the aperture length is a constraint since it provides higher directivity as it is in effect an array of two single-sided holograms. However, it can only reduce the bottom beam over a range of frequencies.

Section 2.6 studied the effect of the strip width on the hologram. We varied the strip width uniformly and related its behaviour to the leakage rate of the antenna. The trend of increasing the strip width will decrease the antenna performance was observed in all cases. This is due to the high leakage rate causing the antenna to radiate too quickly and end up under-utilizing the aperture length which then causes poor aperture efficiency. The initial strip width turned out to be the best case for the substrates considered in this study. Although the leakage rate

analysis is useful for uniform antennas, it is not practical for designing three-dimensional holograms because the cross-section varies along the axial direction.

With these results in mind, we can now form design "guidelines" that can be carried over to the three-dimensional study of Chapter 3:

- First, by including the actual source and substrate in the computation of the interference pattern we will know where to place the strips with respect to the feed, and the curvature of the strips.
- Second, we can exploit the double-minima behaviour (or some similar effects) to place more strips on the substrate to increase the directivity. This can be accomplished by varying the sources' amplitude in the computation of the interference pattern.

Chapter 3 - Three-Dimensional Investigations of Holographic Antennas

The objective of this chapter is to apply the design procedure from the 2-D studies to design 3-D holograms and compare them with the existing holograms in [7]. We will use the commercially available electromagnetic simulators HFSS [22] and IE3D [23] to carry out the 3-D studies. HFSS can model true 3-D objects, and IE3D can model multi-layered planar objects but with an approximation that the substrates are of finite thickness but are infinite in extent. The true 3-D interference pattern would be the interference pattern of the actual source with the plane wave determined in the presence of the large finite $10\lambda_o$ x $10\lambda_o$ 3-D dielectric substrate. This is electrically large for any electromagnetic tools to model in 3-D since the tools have to divide all objects into small segments and solve for the unknown quantities on those segments, and the number of segments that can be handled is proportional to the amount of memory required. Even with a UNIX system with 8GB of RAM and 20GB of virtual memory, we still do not have enough memory to model the large $100\lambda_o^2$ substrate accurately, especially in the near-field region where we need to use more segments to capture the correct field distribution to compute the interference pattern. Therefore, we will approximate the 3-D interference pattern by assuming the substrate is infinite in the design of the large 3-D hologram. IE3D will be used to compute the interference pattern in the presence of the infinite substrate and the 3-D source. We will use a 3-D printed-source instead of a horn antenna because this has the advantage of producing a flat-profile for the whole antenna, consisting of the hologram and source antenna, and it can be fabricated on a single sheet of dielectric substrate. Also, the feed alignment problems incurred in using the feed horn, and the need for a specialized fixture to mount the hologram, will be eliminated [7].

Section 3.1 will discuss the 3-D printed-source that will be used in all the 3-D studies of this chapter. Although we will use the interference pattern of the infinite substrate to design the 3-

D antennas, we will also study the interference pattern of a smaller ($4\lambda_o$ x $4\lambda_o$) 3-D finite substrate using HFSS to observe the effect of the finite substrate in Section 3.2. The interference pattern using the infinite substrate is discussed in Section 3.3. Experimental results of the printed-Yagi-fed hologram are presented Section 3.4. Finally, Section 3.5 summarizes Chapter 3.

3.1 Printed-Yagi Antenna Used in the 3-D Studies

Initially we were going to select the printed-dipole used in [7] as the reference source to have a direct comparison with the existing hologram but its large ground plane required more than 50 000 unknowns in IE3D and the program cannot accurately model such a large structure. Nevertheless we let the program ran for at least one week on a 2.6GHz Pentium Xeon machine with 2GB of RAM and it did not respond nor finish with computing the current density. So we will use a printed-Yagi antenna based on [17] and minimize the amount of metallic area to reduce the number of unknowns in IE3D. The dimensions in [17] could not be scaled by λ_g to 30GHz, so we used the design guidelines in [18] to come up with the dimensions to operate at 30GHz. Figure 3.1 shows the antenna designed with HFSS because IE3D is not able to predict the correct radiation pattern in the endfire direction since it considers the substrate to be infinite in this direction. The top side of the antenna has 2 directors to increase the endfire gain and the dipole is fed by a microstrip line. The bottom side has the ground plane placed at $\lambda_g/4$ from the bottom dipole arm to function as a reflector and reduce the backfire lobe. The return loss of the antenna is good and the endfire gain is acceptable at 30GHz, as shown in Figure 3.2. The H-plane (xz-plane) and E-plane (yz-plane) radiation patterns are shown in Figure 3.3. Note that the design of the printed-source did not use the much larger substrate size required for the eventual holographic antenna with which the Yagi-source is to be used.

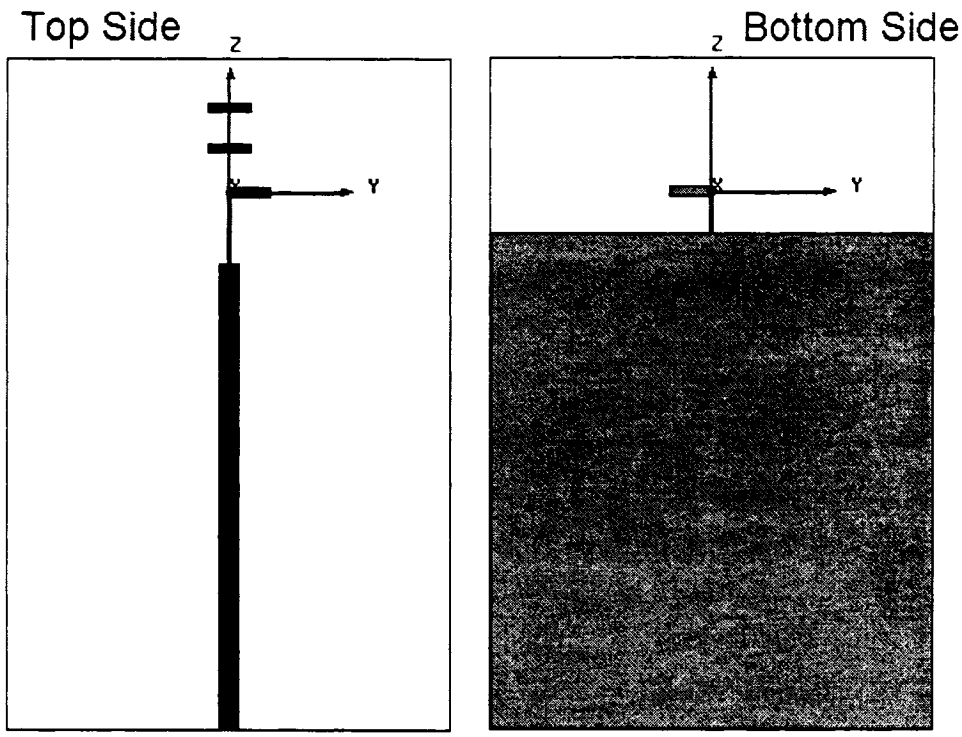

Figure 3.1 - Printed-Yagi antenna used in 3-D interference patterns and 3-D holograms

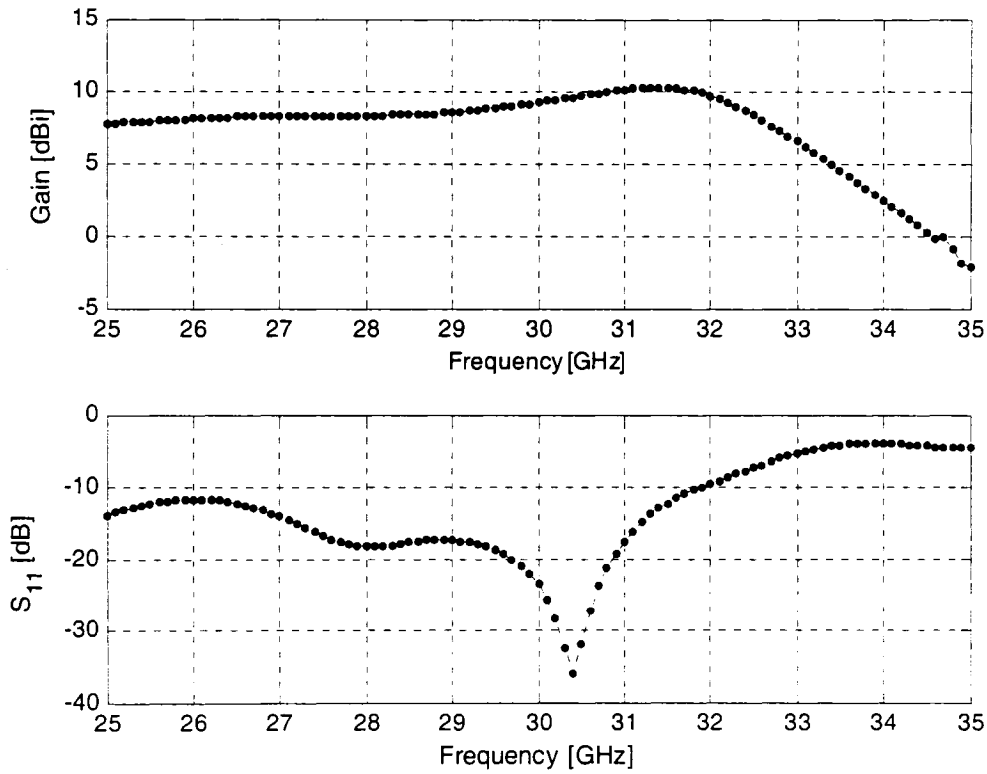

Figure 3.2 - Return loss and endfire gain of printed-Yagi antenna

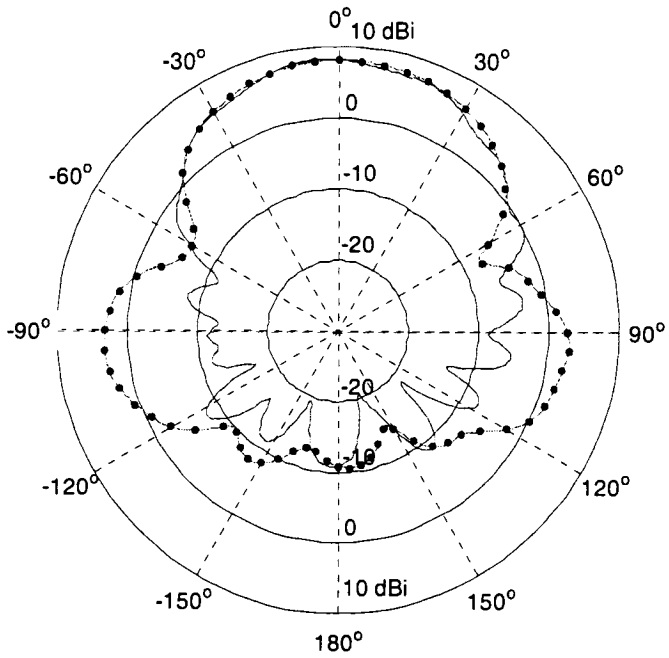

Figure 3.3 - Computed gains of printed-Yagi antenna: H-plane (— • — • —), E-plane (———), f=30GHz

3.2 Interference Patterns Determined in the Presence of the Finite Dielectric Substrate, and Antennas Realized from these Patterns

Since the interference pattern of the large substrate could not be modelled, we will study the fringe pattern of a smaller substrate and antennas using the smaller substrate. The structure used in the computation of the interference pattern is shown in Figure 3.4 and the holographic antenna will be what is shown in the figure but with strips etched on the top surface of the dielectric slab. The small substrate used in this study is $4\lambda_o$ x $4\lambda_o$ instead of the large $10\lambda_o$ x $10\lambda_o$ substrate used in the fabricated antennas of [3-5, and 7]. The limitation of HFSS on the UNIX workstation is about 500 000 tetrahedra where they are used to represent all discretized objects in the entire model's volume. To maximize the accuracy of the field values, we set the mesh size to be at most 0.5mm (λ_o/20) on the top surface of the dielectric slab along with the usual adaptive mesh setting. This setting will only force the

tetrahedra to be small on the surface of interest and is more efficient than increasing the default mesh setting, which would apply to the entire volume. The number of tetrahedra required was around 400 000 with a surface mesh setting of 0.5mm.

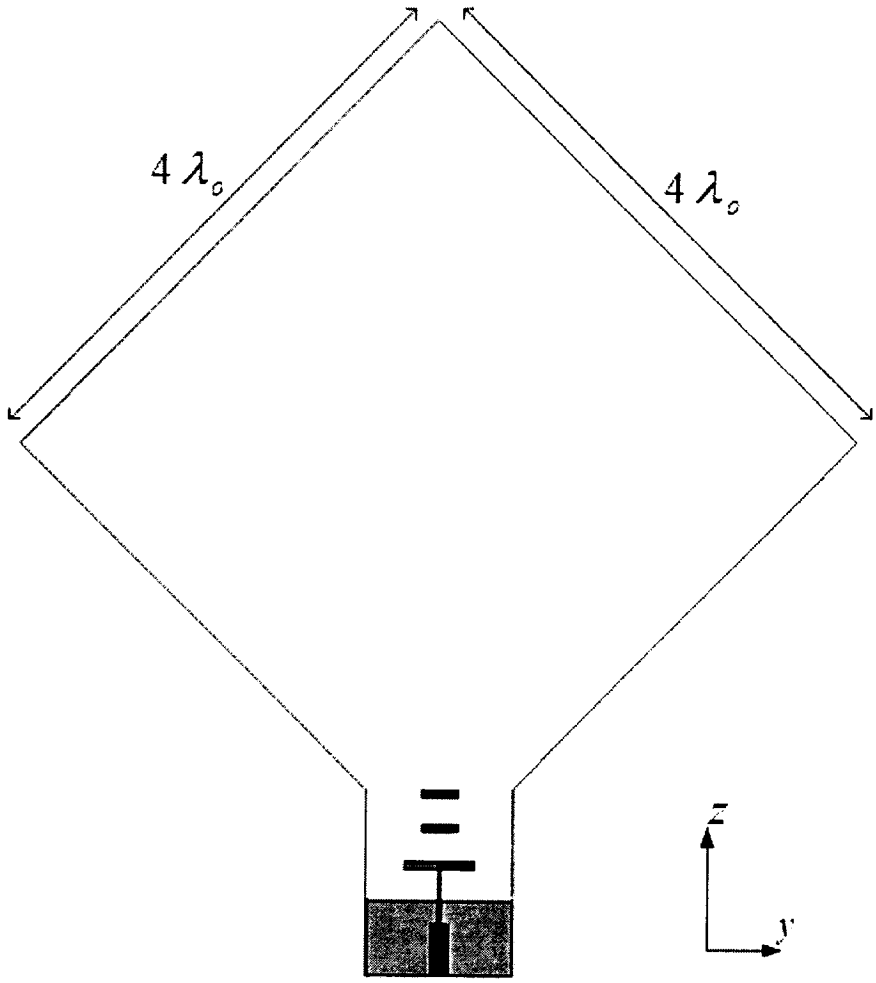

Figure 3.4 - Printed-Yagi antenna and the dielectric slab of $4\lambda_o$ x $4\lambda_o$

In the 3-D studies, the ratio of the amplitude of the plane wave, B, to the amplitude of the reference source, A, will be normalized to the maximum amplitude of the reference source in the substrate region instead of the amplitude of the reference source at the top edge of the dielectric slab as in the 2-D study. Figure 3.5 shows the 3-D interference pattern observed at the substrate surface where the high field values correspond to the source region and we can see the outline of the substrate. The minima appear random compared to the 3-D free-space fringe pattern, using (1.2), shown in Figure 3.6 because all finite effects are modelled in

HFSS. Although we have used the highest possible mesh setting to compute the interference pattern, there is still numerical "noise" in the data as shown in Figure 3.7 where the minima positions are plotted on top of the fringe pattern. Even after various low-pass filtering schemes were implemented we were not able to remove the numerical noise. As a result the minima locations of the filtered interference pattern did not coincide with the minima positions of the unfiltered pattern, as shown in Figure 3.8.

The low-pass filtering was performed in the spatial domain by convolving the matrix representing the interference pattern with a filter available from [26]. And to find the minima positions we used a local minima searching routine available from [27]. The routine can only search in a one-dimension so we let the routine searched for the local minima in one column at a time and repeated the procedure N times for N columns in the matrix containing interference pattern.

We cannot increase the mesh setting to increase the field resolution because we have reached our computational limit. Nevertheless, we will apply the design procedure from Section 2.7 of the 2-D study to synthesize a small ($4\lambda_o$ x $4\lambda_o$) antenna even though the minima appear random and not in circular tracks like the free-space case. Figure 3.9 shows the antenna model and Figure 3.10 shows the computed gain of the antenna realized from the unfiltered interference pattern with B/A = 0.01 and that using the filtered pattern with B/A = 0.005. Two beams near broadside were reconstructed along with large amount of leftover power in the endfire region due to the small aperture size. Because of our memory limitation we cannot use this procedure to design the actual large ($10\lambda_o$ x $10\lambda_o$) hologram, but it was worthwhile to demonstrate that the desired beam can be reconstructed even when the strips appear more random than what we expected. The true large interference pattern covers an area of $100\lambda_o^2$ and we will approximate this with the interference pattern determined in the presence of an infinite substrate in the next section.

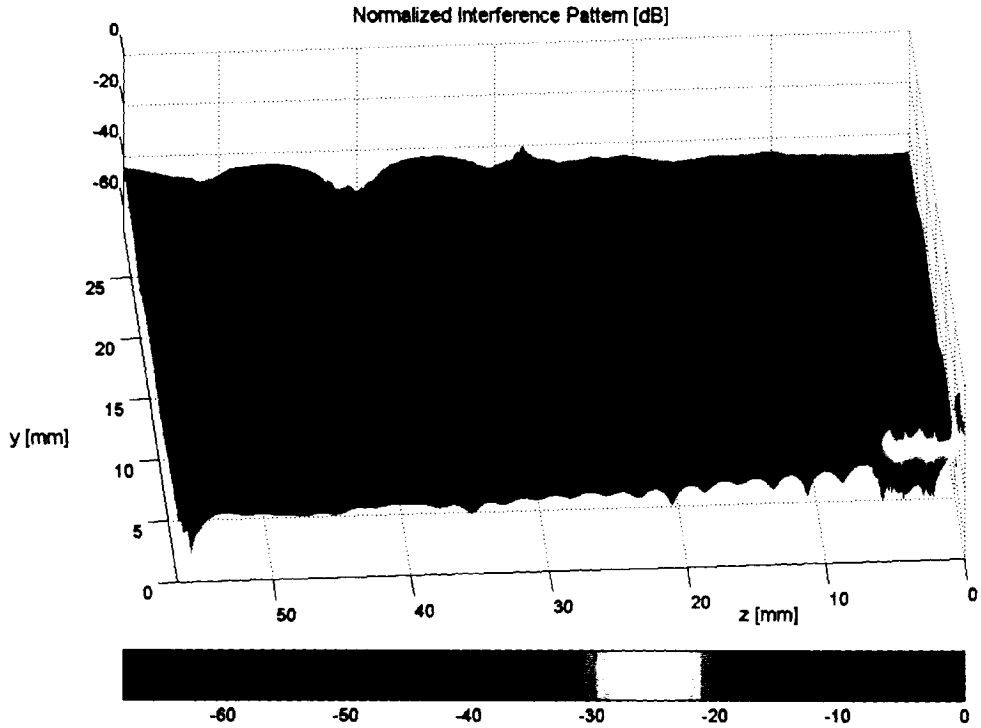

Figure 3.5 - 3-D interference pattern of finite dielectric substrate with B/A = 0.01

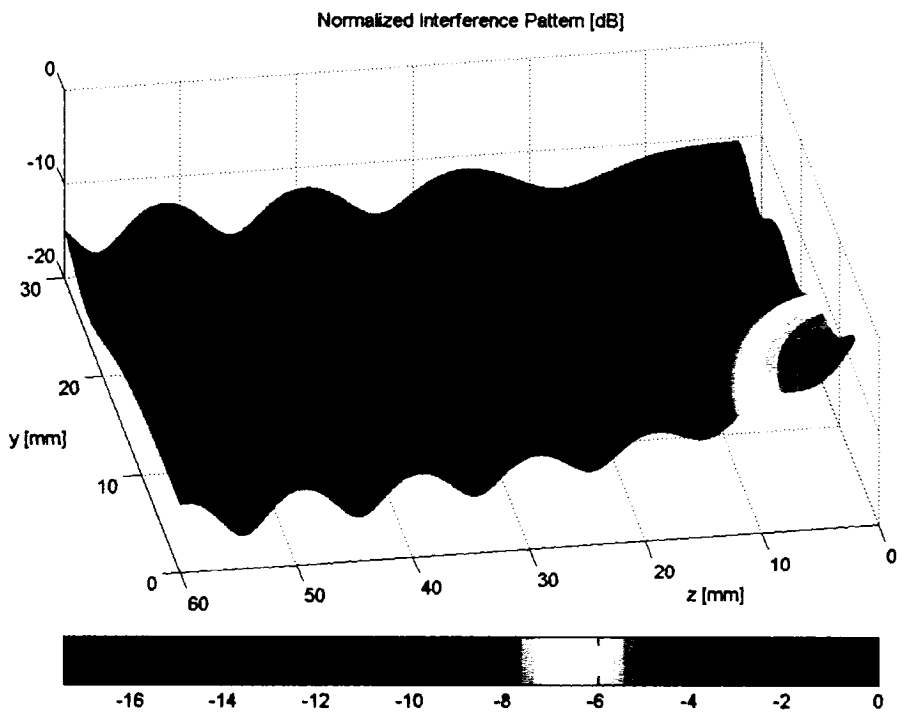

Figure 3.6 - Free-space 3-D interference pattern

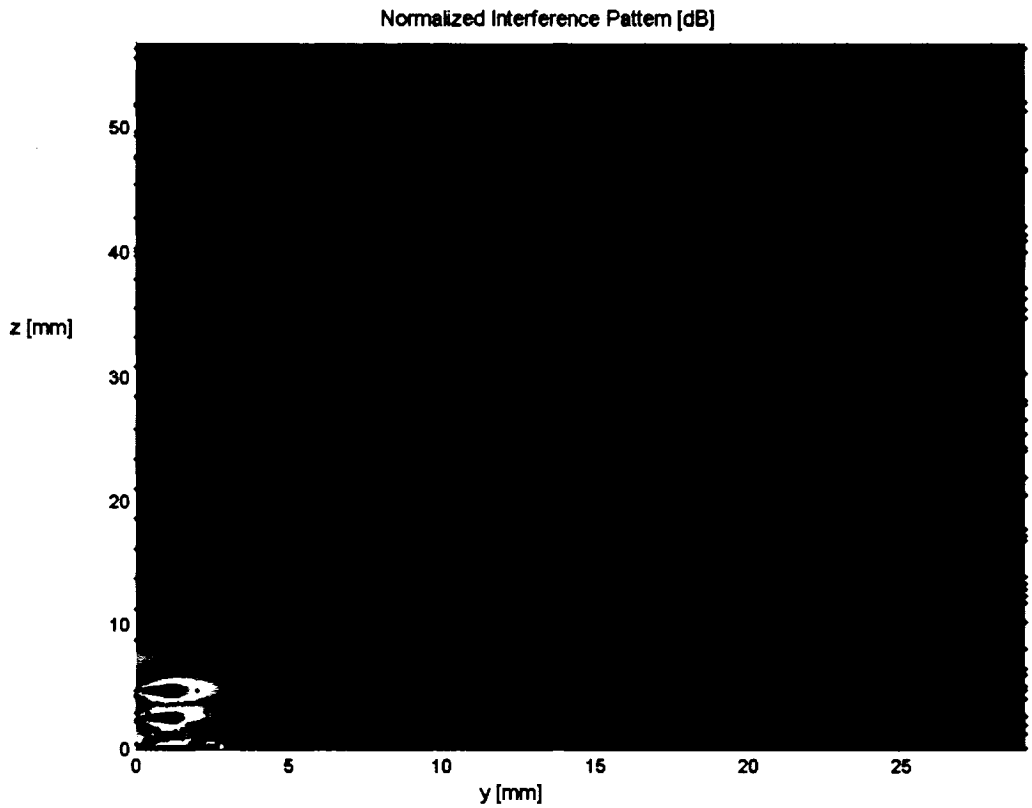

Figure 3.7 - 3-D interference pattern, B/A = 0.01, and minima position (. . . . . .)

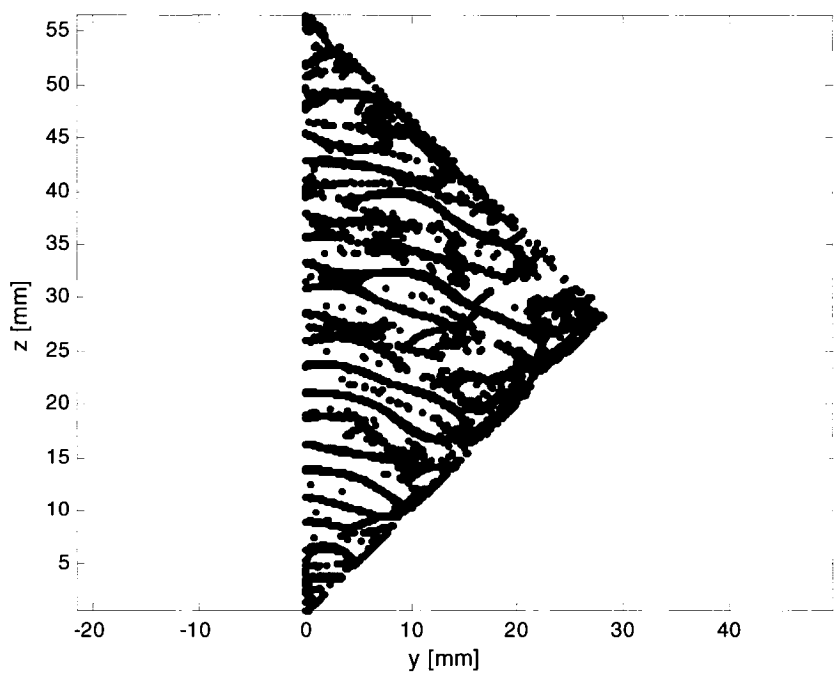

Figure 3.8 - Minima position of unfiltered interference pattern (blue), filtered interference pattern (red)

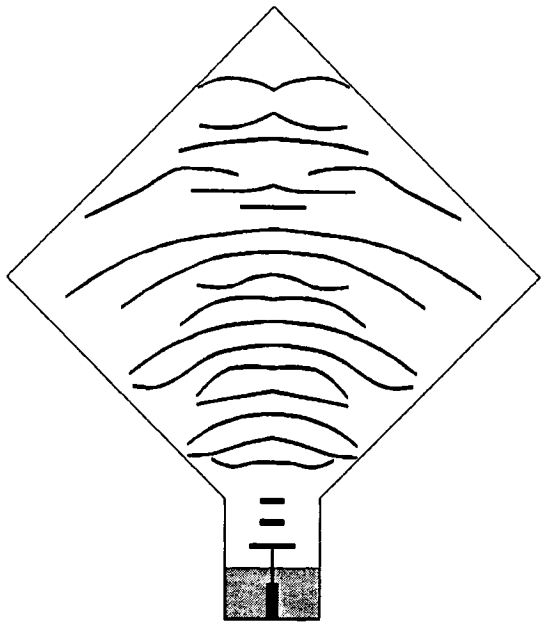

Figure 3.9 - 3-D antenna realized from unfiltered interference pattern minima with B/A = 0.01

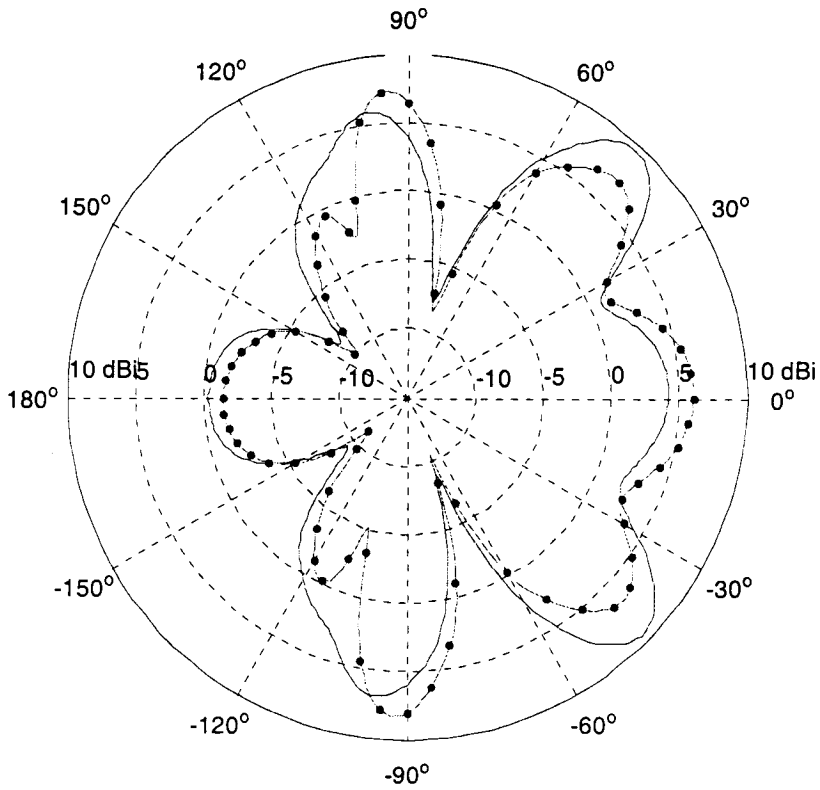

Figure 3.10 - H-plane radiation pattern of antennas realized from unfiltered interference pattern with B/A = 0.01 (————) and filtered interference pattern with B/A = 0.005 (— • — • —), f=30GHz

3.3 Interference Patterns Determined in the Presence of the Infinite Dielectric Substrate and Antennas Realized from these Patterns

Even though IE3D cannot model planar endfire antennas, it can still provide the correct near-field distribution of the source because it does not use any approximations to compute near-zone quantities. The advantage of using IE3D is that only metallic objects are required to be segmented. Thus the simulation does not require as much memory as the finite substrate case because the effect of the infinite substrate is already considered in the program's formulation. The field is computed from the currents on the discretized objects, and we will be able to observe the field over a large region with higher fidelity. The geometry for the Yagi-source in IE3D is the same as the structure shown in Figure 3.4 but the substrate is now infinite, and the coordinates system has been changed so that the yz-plane is now the xy-plane (due to the default restriction in IE3D's formulation). The field due to the 3-D source in the presence of the infinite substrate will be determined with IE3D, and we will compute the field due to the plane wave in the presence of the infinite substrate analytically. We then combine the two fields to obtain the interference pattern. The field due to the plane wave can be modelled by transmission lines with a one-to-one correspondence between the plane wave parameters ($E_{tot}, H_{tot}, k, \eta$) and transmission line parameters ($V_{tot}, I_{tot}, \beta, Z$) [19]. The geometry for the plane wave source is illustrated in Figure 3.11 where the infinite dielectric substrate is located on the xy-plane, and its transmission line equivalence is shown in Figure 3.12. The total field due to the plane wave on the dielectric surface is

$$\underline{E}_{tot}^{PW}(x, y, z = t) = \hat{x} \quad B\left(e^{j\beta_o t} + \Gamma_{in} e^{-j\beta_o t}\right) \tag{2.14}$$

where

$$\Gamma_{in} = \frac{Z_{in} - Z_o}{Z_{in} + Z_o} \tag{2.15}$$

$$Z_{in} = Z_d \frac{\left(1 + \Gamma_L e^{-j2\beta_d t}\right)}{\left(1 - \Gamma_L e^{-j2\beta_d t}\right)} \tag{2.16}$$

and $\Gamma_L = \frac{Z_L - Z_d}{Z_L + Z_d}$, $Z_L = Z_o = \eta_o = \frac{\mu_o}{\varepsilon_o}$, $Z_d = \frac{\eta_o}{\sqrt{\varepsilon_r}}$, $\beta_d = k_o\sqrt{\varepsilon_r}$. The interference pattern observed on the dielectric surface is then

$$I(x, y, z = t) = \sqrt{\left(E_x^{ref} + E_x^{PW}\right)^2 + \left(E_y^{ref}\right)^2 + \left(E_z^{ref}\right)^2} \tag{2.17}$$

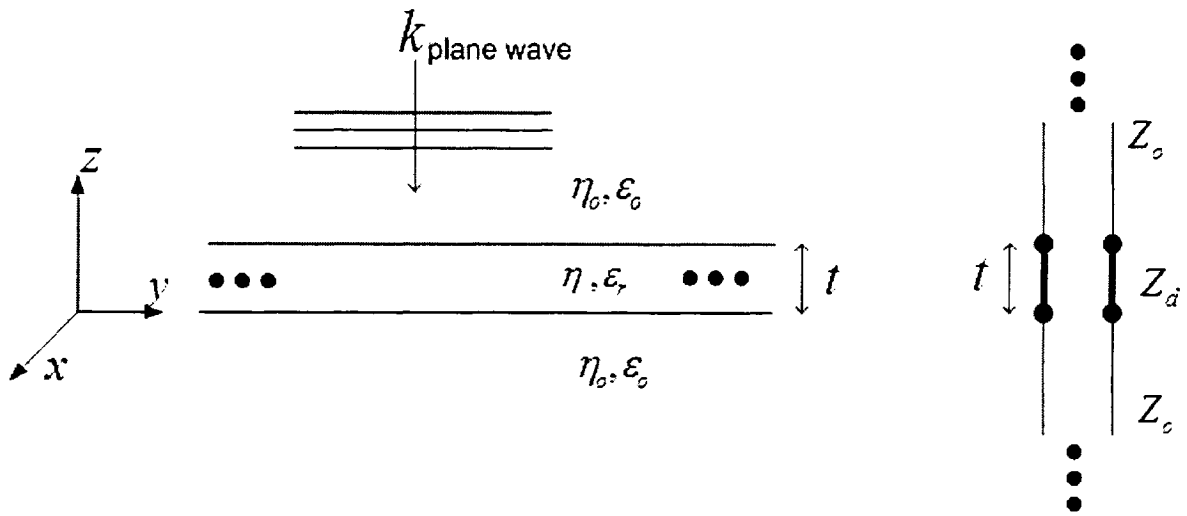

Figure 3.11 - Normally incident plane wave on an infinite dielectric slab and its transmission line model

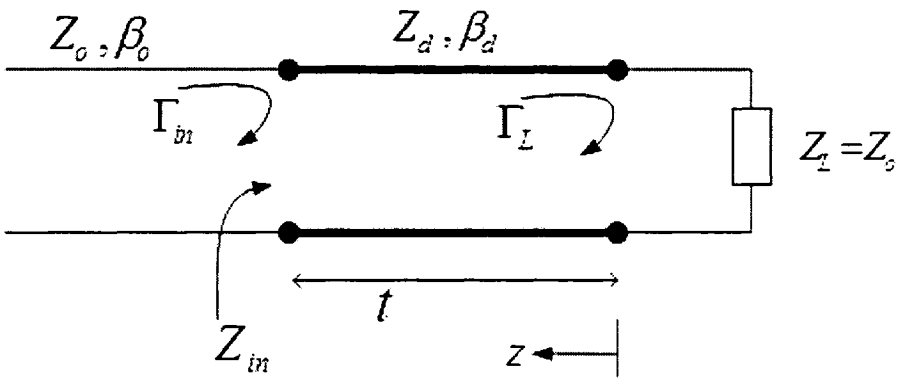

Figure 3.12 - Transmission line model of the normally incident plane wave on an infinite dielectric slab

The interference pattern for the infinite substrate case is shown in Figure 3.13 with the minima locations overlaid on top. For a standard mesh setting of 20 cells/λ_o, the numerical noise still exist but it is does not appear as widespread as in the finite substrate case in

Section 3.2. The noise appeared near the dipole axis because the field needs to be low in this region to be consistent with the null-effect on the dipole axis, and thus is difficult for the program to produce a smooth field variation. The noise is still present for a much higher mesh setting of 100 cells/λ_o for a test case of the simplest configuration consisting of a printed dipole fed by a gap source. At any rate, the field has converged and the minima of the filtered interference pattern coincide with the minima of the unfiltered pattern as shown in Figure 3.14.

The distance between the minima is 9.4mm (λ_g) which agrees with the 2-D results when we only had single-minima in the interference pattern. The double-minima behaviour did not appear as we varied the plane wave's amplitude in the infinite substrate case. This outcome could also be interpreted in terms of transmission lines where the line is now infinite so we do not have reflections, and hence standing waves. Therefore, the interference pattern only showed single-minima like the free-space interference pattern because the medium is infinite for both cases. Figure 3.15 compares the minima shown in red with the superimposed circles shown in blue (where the circles' radii are determined from the minima positions). The first two curves of the minima are elliptical and the remaining minima curves agree with the circular curves. Using HFSS, we modelled two small antennas, using a substrate size of $4\lambda_o$ x $4\lambda_o$, with all circular strips in one case, and the other case using two elliptical strips and circular strips for the remaining strips. Both radiation patterns have the same appearance with the elliptical case having slightly less gain. Figure 3.16 compares the radiation pattern of the circular strips antenna with the antenna realized from the finite interference pattern of the same substrate size from Section 3.2. We see that the interference pattern of the finite substrate can be approximated by that of the infinite substrate to design the actual large antenna because the reflections in the finite small substrate are stronger than in the actual large finite substrate and yet we can achieve similar gain in the broadside direction using the interference pattern of the infinite substrate.

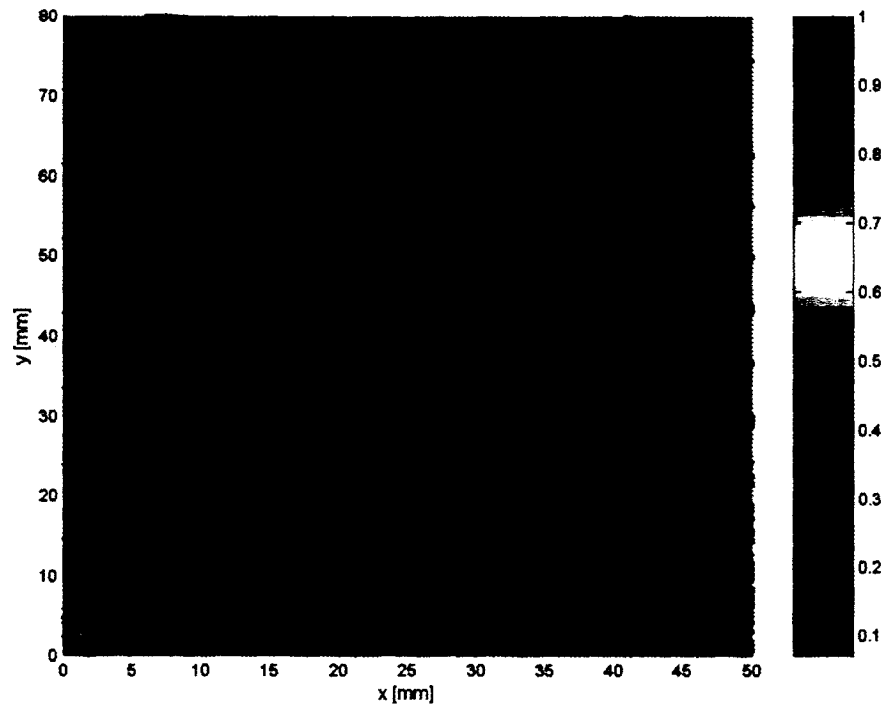

Figure 3.13 - Interference pattern determined in the presence of the infinite dielectric substrate

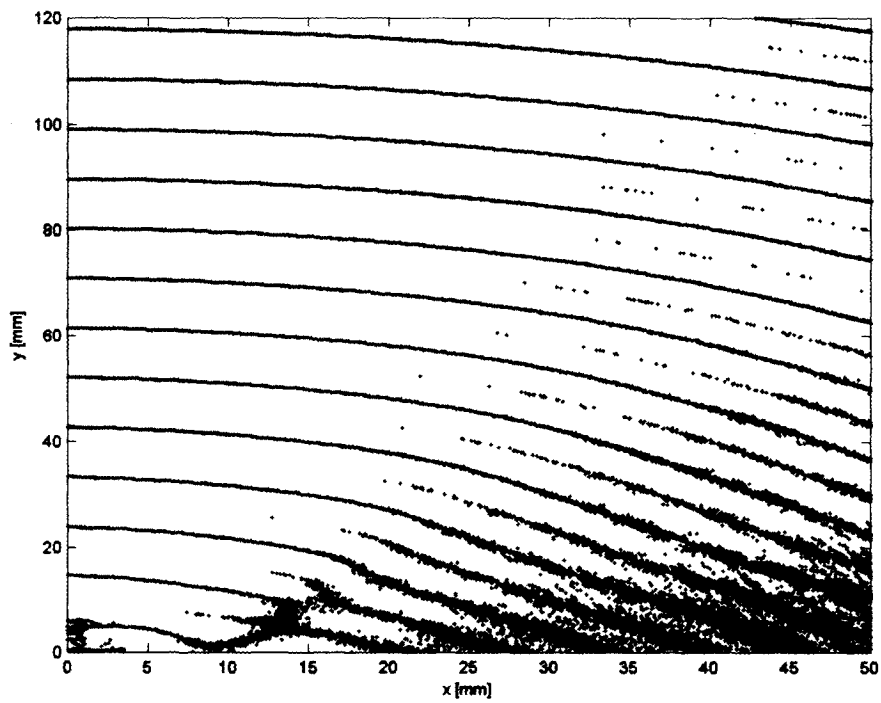

Figure 3.14 - Minima position of unfiltered (blue) and filtered interference patterns (red)

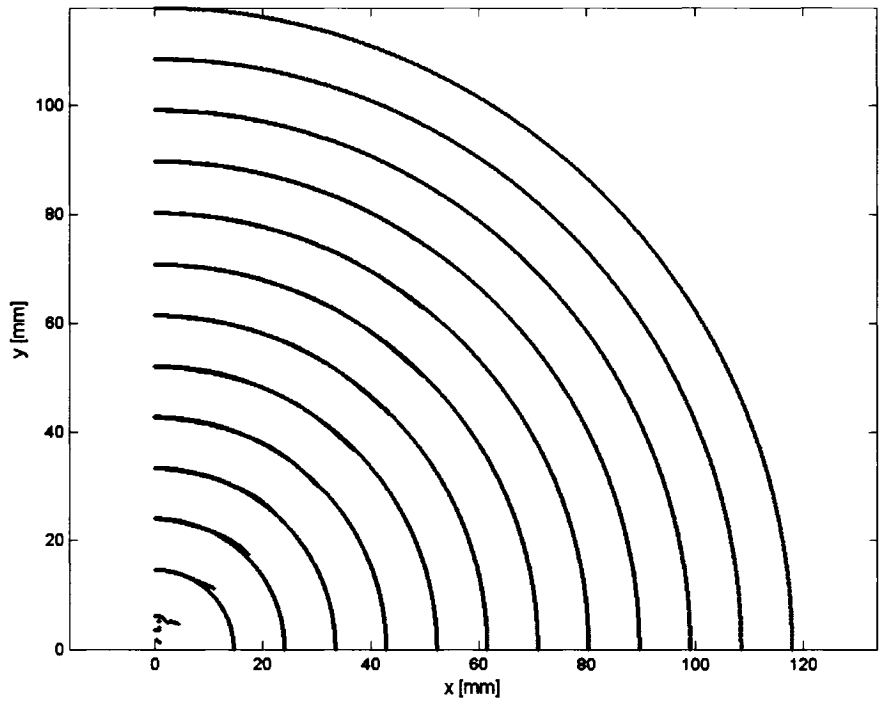

Figure 3.15 - Interference pattern minima (red) and circular tracks extrapolated from the minima (blue)

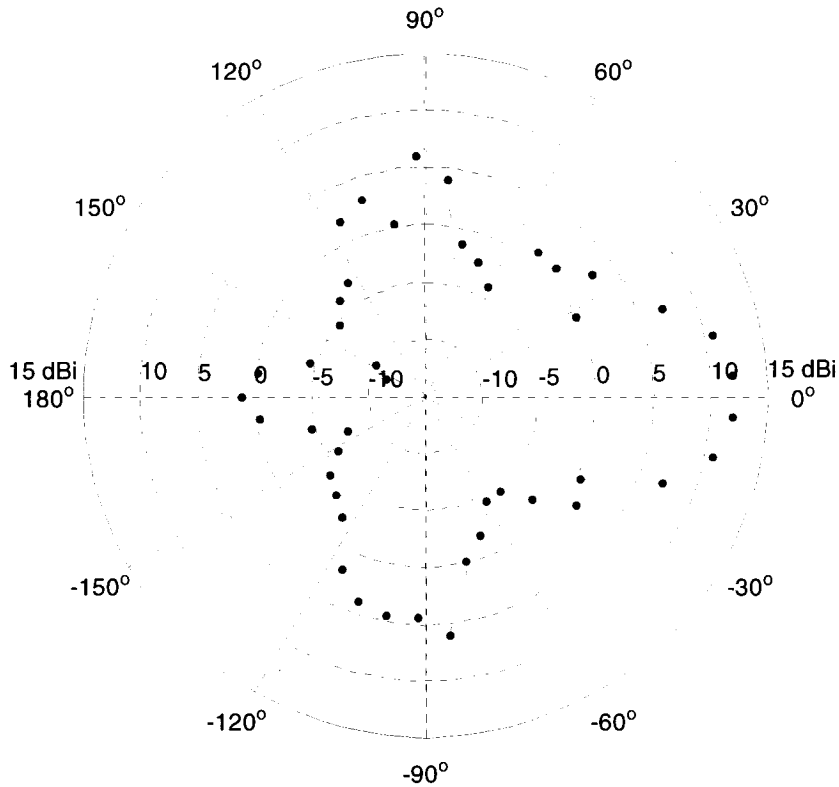

Figure 3.16 - Radiation pattern of antennas realized from interference pattern of the infinite substrate (– — • — • —) and from interference pattern of the finite substrate with B/A = 0.005 (————)

3.4 Experimental Validation of Three-Dimensional Antenna

As a proof-of-concept we fabricated a large ($10\lambda_o$ x $10\lambda_o$) hologram with the Yagi source to compare with the hologram fed by the printed-dipole in [7]. All the dimensions are listed in Appendix B. We used the same printed source described in Section 3.1 but with a larger ground plane to minimize the interference from the launch connector with the printed-Yagi source. The interference pattern of the infinite substrate was recomputed with the modified source since the larger ground plane changed the minima locations. The large antenna could not be modelled accurately in HFSS but we were able to compute its radiation pattern in Empire [24] which shows a directivity of 15.3dBi at broadside, as shown in Figure 3.17. Given that the interference pattern was computed in the presence of an infinite substrate, it did not matter whether we fabricated a rectangular shape or diamond shape substrate. So we fabricated the hologram on a rectangular substrate to allow us to observe the effect of the shape of the substrate on the antenna performance. The strips were still etched to fit into a diamond-shaped slab that will be crafted by cutting the corners off the rectangular shape slab, as illustrated in Figure 3.18. This gave us three cases: (1) rectangular slab, (2) top corners removed, (3) top and bottom corners removed to form the diamond shape slab.

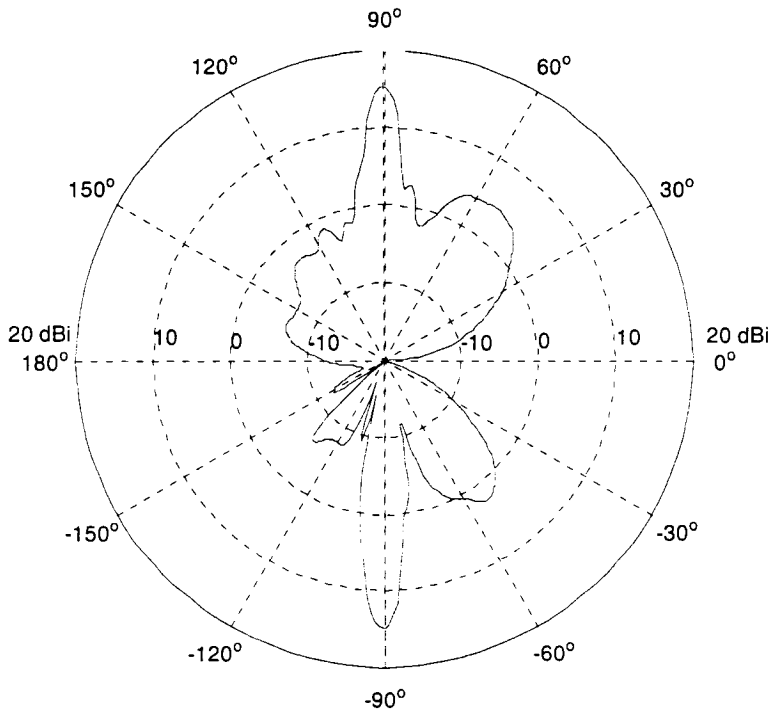

Figure 3.17 - Computed directivity pattern of large antenna with a directivity of 15.3dBi, f=30GHz

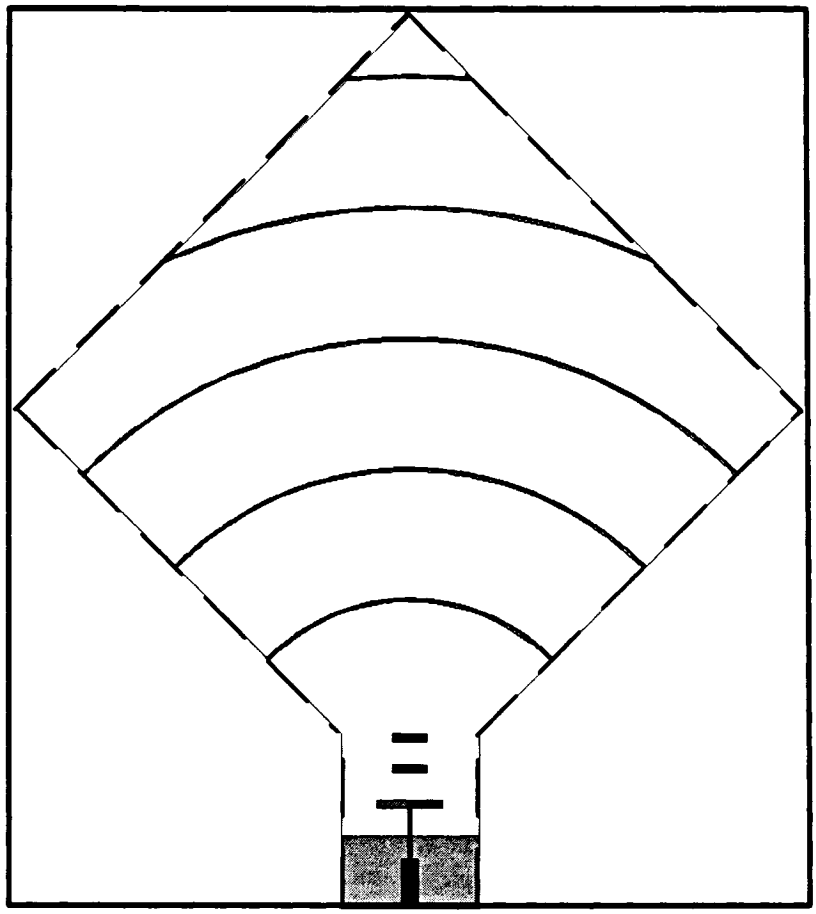

Figure 3.18 - Illustration of rectangular slab hologram

A picture of the fabricated antenna is given in Figure 3.19 where we can see part of the standard-size connector block is hanging out due to the small printed source. The hologram is held in place by a dielectric rod at the bottom of the picture during the measurement process. The measured return loss, RL, for the three cases are shown in Figure 3.20. All three cases show a good match at 30GHz, but they degrade around at 29-30GHz when the antennas scan through broadside. Figure 3.21 compares the RL of case 2 with the printed-dipole-fed hologram and open-waveguide-fed hologram from [7].

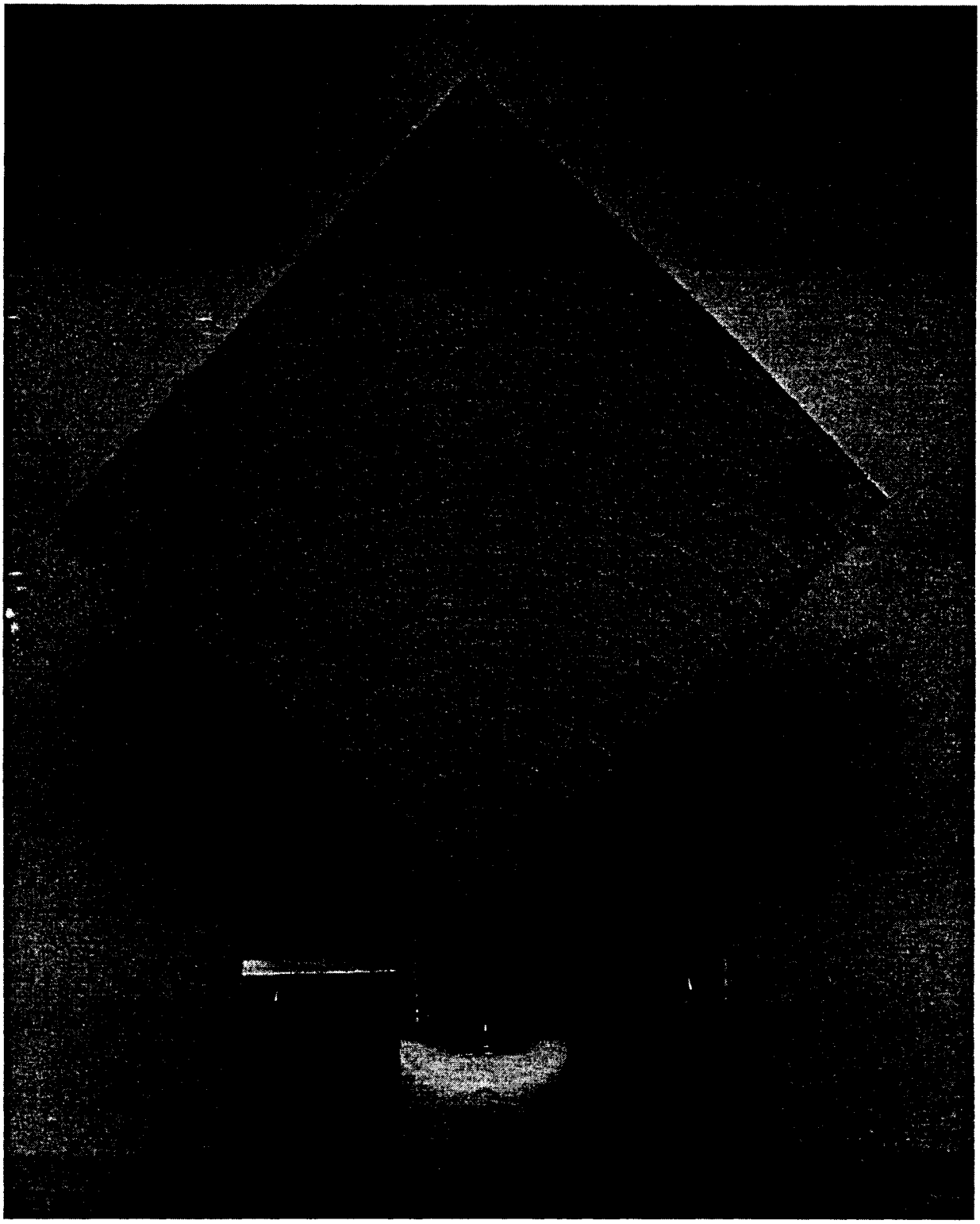

Figure 3.19 - Fabricated hologram fed by a printed-Yagi antenna

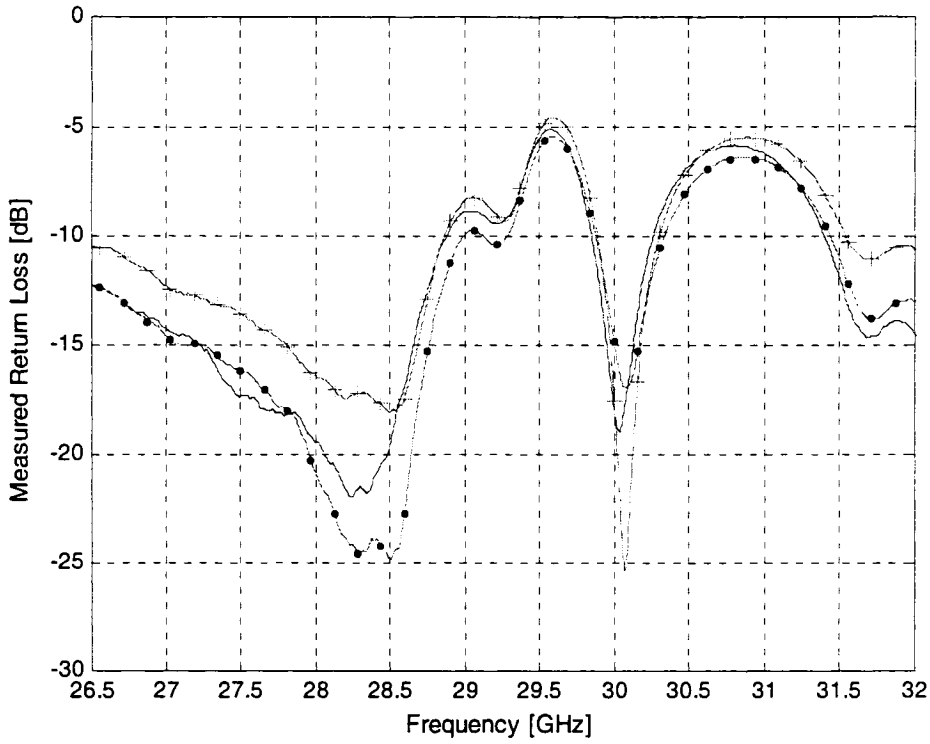

Figure 3.20 - Measured return loss of Yagi-fed holograms: case 1 (————), case 2 (— • — • —), case 3 (— + — + —)

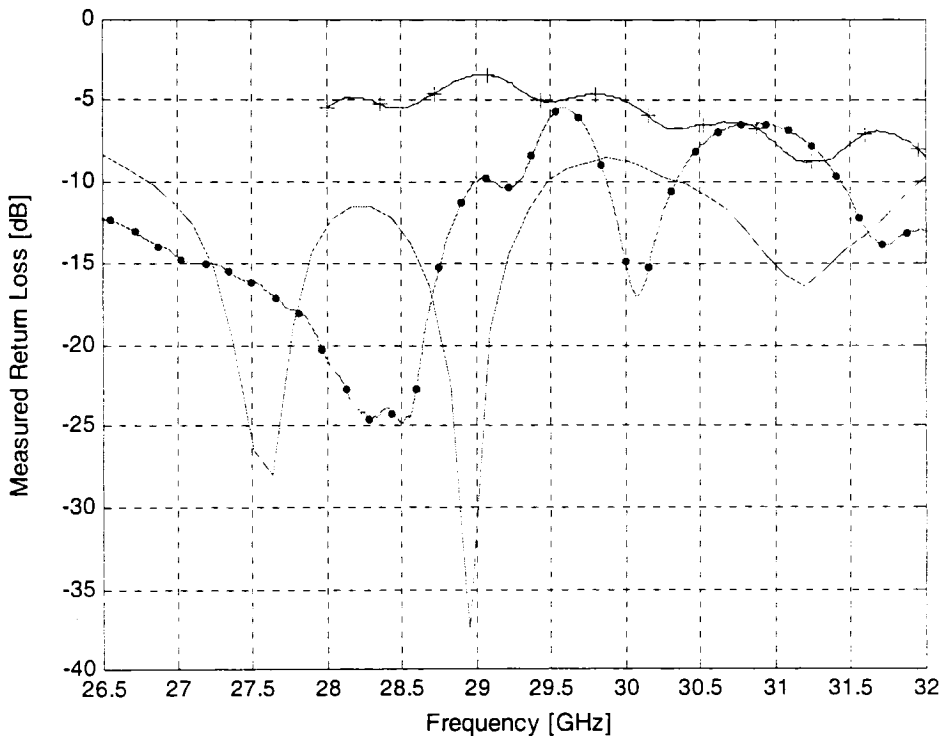

Figure 3.21 - Measured return loss of Yagi-fed hologram (— • — • —), dipole-fed hologram (———— —), and open-waveguide-fed hologram (— + — + —)

The corrected gain and its beam angle are shown in Figures 3.22 and 3.23, respectively. Note that for all measured patterns the bottom broadside beam is at +90° and not -90° as in the simulation results (due to the way the antenna was mounted in the anechoic chamber). The gain was corrected to compensate for the insertion loss from the semi-rigid cable used during the measurement process. A connector loss of 0.2dB was also added to the measured gain [5]. Case 2 and 3 showed similar gain but there is a noticeable difference between case 1 and 2/3. This could be due to the shape of the substrate where the guided wave is "free to go anywhere" in the rectangular case, hence less energy is being intercepted and scattered by the strips compared to when the top part is cut off and the guided wave is constrained by the triangular shape substrate, as illustrated in Figure 3.24. This difference can also be observed in the endfire lobe of case 1 and 2 in Figure 3.25 where it is higher for case 2.

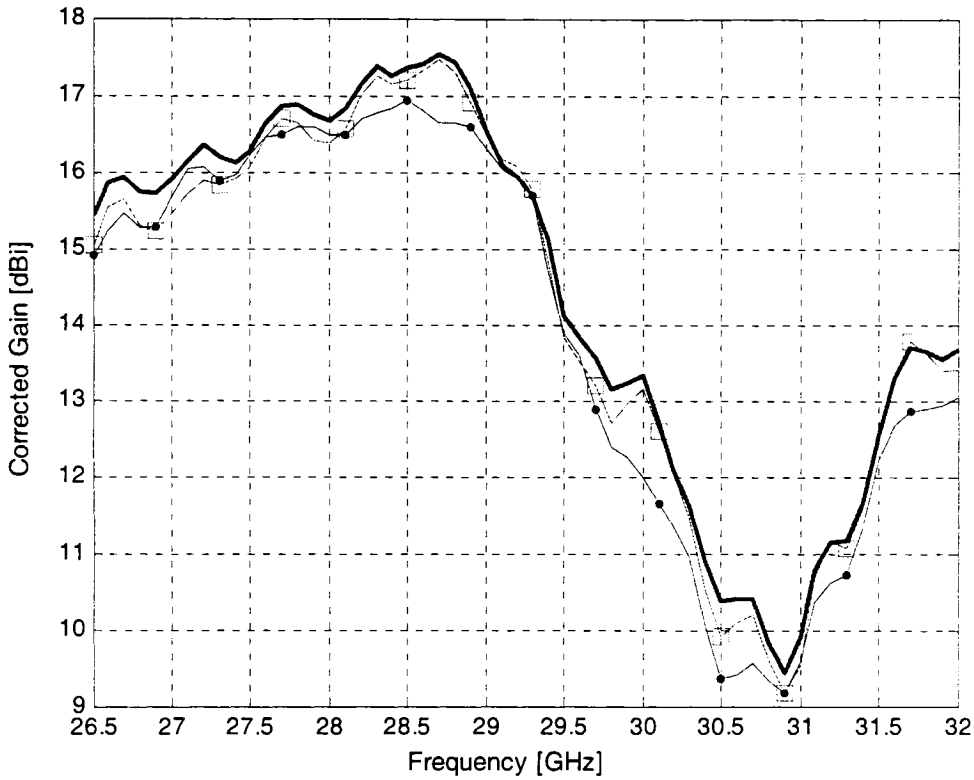

Figure 3.22 - Corrected measured gain of case 1 (—— • —— • ——), case 2 (————), case 3 (—— □ —— □ ——)

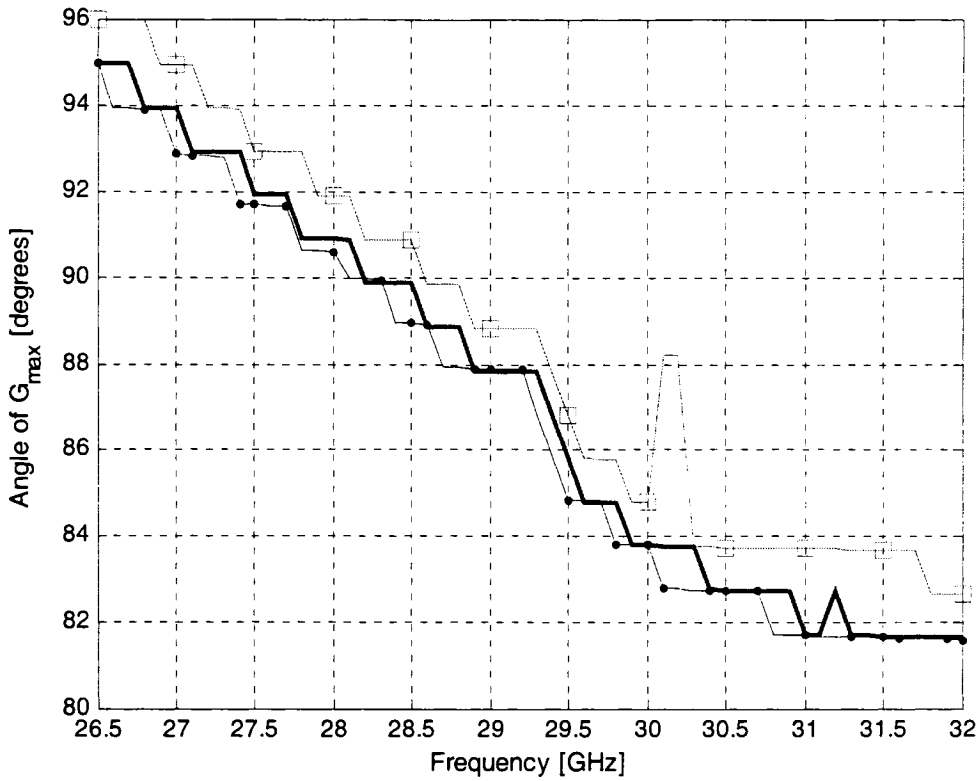

Figure 3.23 - Angle of maximum gain of case 1 (— • — • —), case 2 (————), case 3 (— □ — □ —)

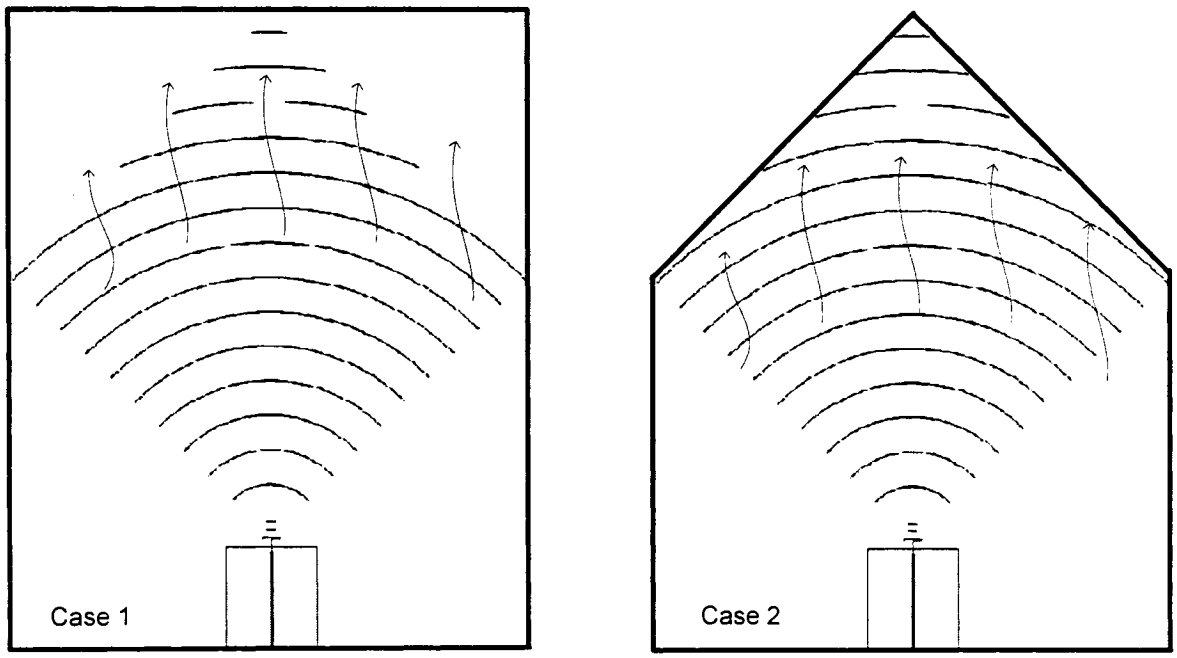

Figure 3.24 - Illustration of Case 1 and 2

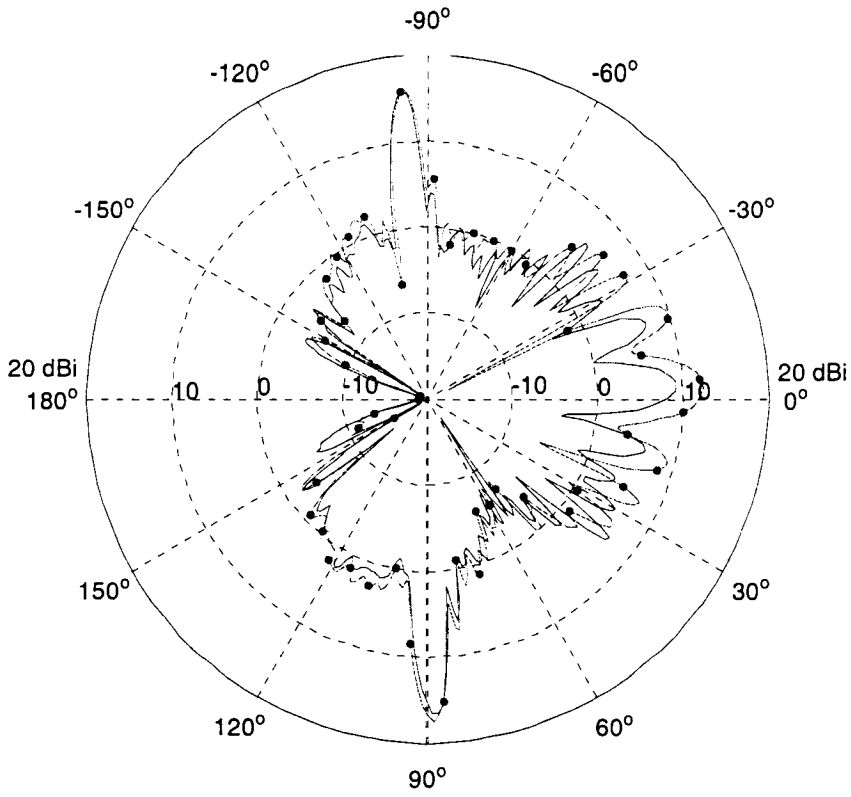

Figure 3.25 - Measured gains for case 1 (————), case 2 (— • — • —) at 28.7GHz

The asymmetry in the main beams is due to the asymmetric printed-feed, and was observed in all three cases. The printed-feed is asymmetric since the ground plane is situated on the bottom side of the substrate while the microstrip feed line is located on the top side. The asymmetric beams were not apparent in [4, 5] since symmetric sources (open-waveguide and feed-horn) were used to feed the hologram. As we varied the frequency, the asymmetry in the feed caused the bottom beam to scan through broadside first, and then both beams scan through broadside at around 29-30GHz. Grating lobes appeared after 30GHz because the spacing between the strips is now larger than λ_g of the observed frequency and caused the gain to decrease dramatically. The low gain associated with both beams at broadside is common in both simulation results (of Figures 2.17, 2.18) and measured results in [3, 4]. The beam scanning behaviour is illustrated in Figures 3.26, 3.27 where the radiation pattern of case 2 is shown for various frequencies. Simulation results of the small antennas from Sections 3.2, 3.3 also showed asymmetric beams as we changed the frequency but it was not

as apparent as the measured results due to the small aperture size. The cross-polarization level is about 20dB at 28.7GHz and 15dB at 30GHz for case 2.

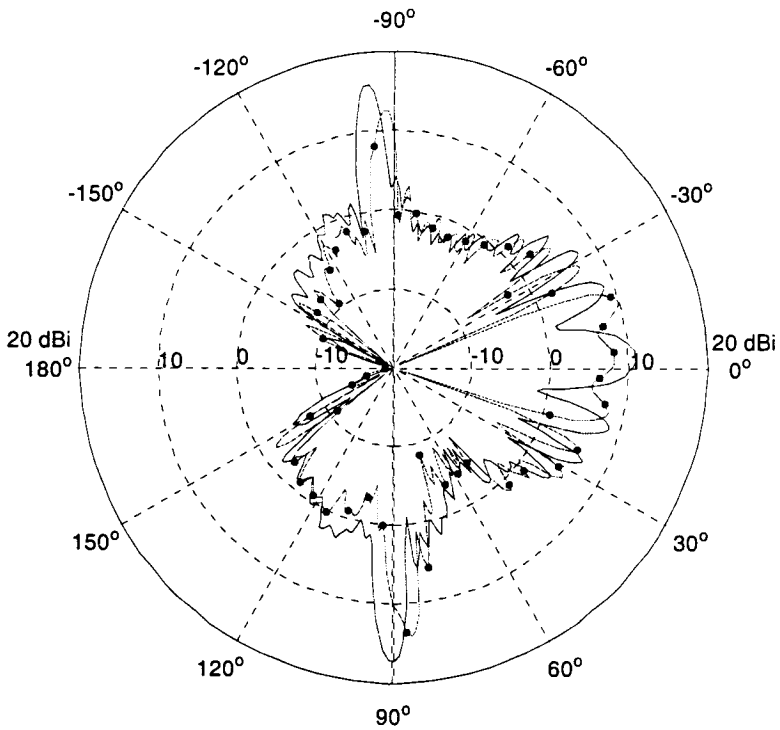

Figure 3.26 - Measured gain of Case 2 at 28.3GHz (————), 29.5GHz (— • — • —)

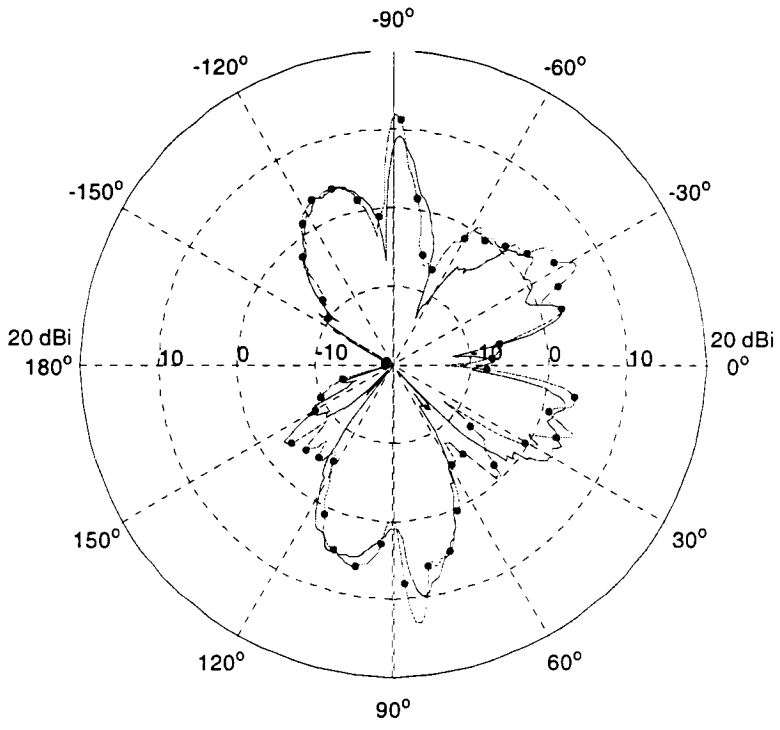

Figure 3.27 - Measured gain of Case 2 at 30GHz (— • — • —), 31GHz (————)

Due to the beam asymmetry in the fabricated hologram, the maximum gain is at 28.7GHz instead of at 30GHz. However, the gain is higher than the printed-dipole-fed hologram by 1dB, which is significant, considering that this represents an increase in the effective aperture size of roughly 25%. Plus, the new hologram has a "cleaner" pattern than the printed-dipole-fed hologram. As shown in Figure 3.28, the printed-dipole-fed hologram also exhibit similar beam asymmetry to the printed-Yagi-fed hologram due to its asymmetric feed. The pattern of the open-waveguide-fed hologram is shown in Figure 3.29. Its gain is higher than the printed-fed holograms because the open-waveguide is more directive than the printed-feeds in the plane of the substrate and the plane orthogonal to the substrate (H-plane) [7]. Hence, that antenna has lower spillover loss and higher gain. Also both printed-sources have more losses than the waveguide feed due to their microstrip feed lines [7]. On the other hand, as indicated in the endfire lobe the printe-Yagi-fed hologram has more leftover power than the two holograms in [7], as shown in Figures 3.28 and 3.29. This is actually desirable since one limitation with the free-space hologram is that it radiates too quickly, and consequently increasing the size of the hologram did not improve the gain proportionally.

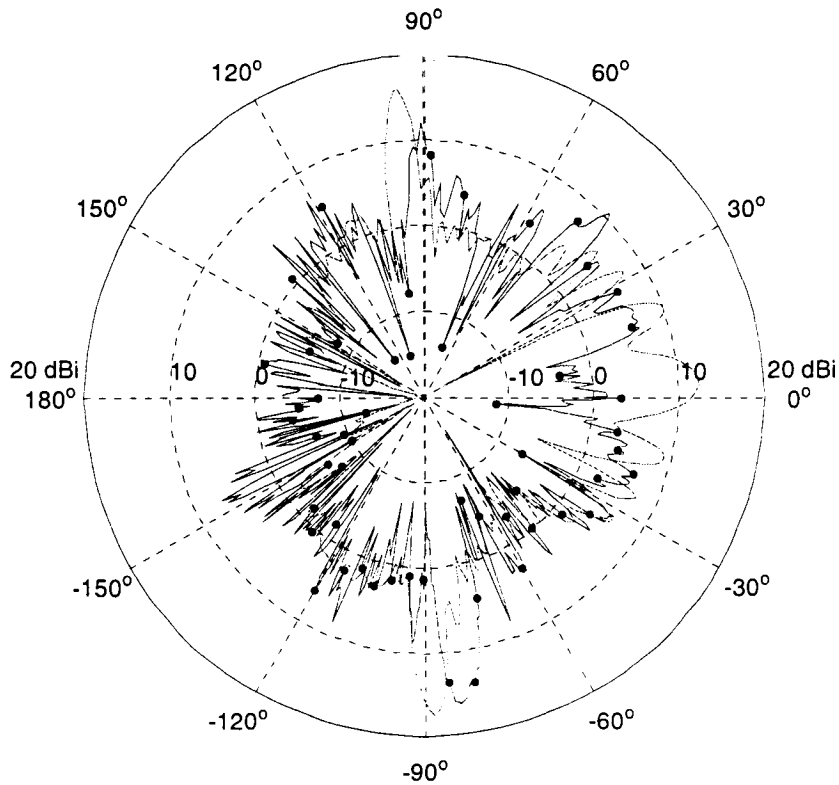

Figure 3.28 - Measured gain of Case 2 at 28.7GHz (——), printed-dipole-fed hologram at 30.5GHz (–•–•–)

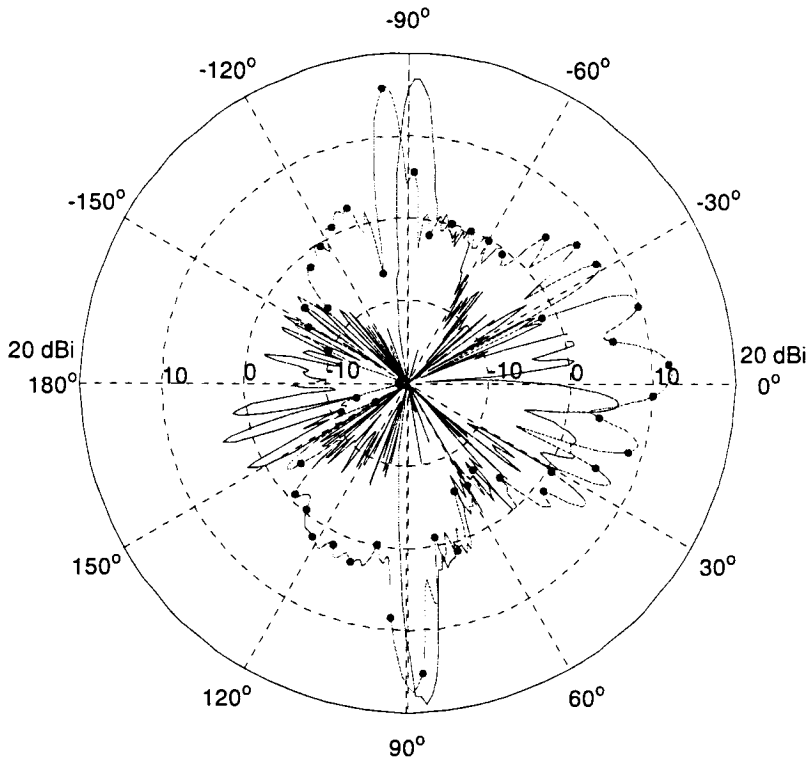

Figure 3.29 - Measured gain of Case 2 at 28.7GHz (— • — • —), open-waveguide-fed hologram at 30GHz (————)

The efficiency of the three holograms is given in Table 3.1. They are low because the thin binary amplitude holograms are inherently inefficient even in the optical holography regime [1, 3]. And although the $10\lambda_o$ x $10\lambda_o$ hologram is electrically large, it is quite small compared to optical holograms. For instance, a hologram on credit cards of roughly 1.5cm x 1cm has an aperture area of 150 x 10^6 λ_o^2, assuming $\lambda_o = 1\mu m$ (since the visible spectrum from red to violet has a wavelength of 700nm to 400nm) [19].

Table 3.1 - Measured gains and efficiencies

Type of feed	Gain [dBi]	Efficiency [%]	Beam shift from broadside [degrees]	Frequency of maximum gain [GHz]
Printed-Yagi	17.55	4.53	1.15	28.7
Printed-dipole	16.5	3.55	6.93	30.5
Open-waveguide	19	6.32	2.31	30

3.5 Summary of the Three-Dimensional Holographic Antenna Investigation

Chapter 3 involved applying the holographic interpretation in the 2-D study to synthesize 3-D holograms to compare with the printed-dipole-fed hologram in [7]. In Section 3.1 we presented the printed-Yagi source to be used in the eventual 3-D hologram because we could not model the printed-dipole accurately in IE3D. The true 3-D interference pattern required including the large $10\lambda_o$ x $10\lambda_o$ dielectric substrate along with the actual source but it could not be computed due to current computer-memory limits. Therefore we studied the interference pattern with the inclusion of a small $4\lambda_o$ x $4\lambda_o$ finite substrate in Section 3.2. The antennas realized from these patterns confirmed the holographic interpretation from the 2-D study and showed a broadside beam even though the strips are noncircular and are placed at random locations. Section 3.3 discussed the interference pattern determined in the presence of the infinite substrate required to synthesize the large hologram. The pattern only exhibits single-minima because reflections do not exist when the dielectric slab is infinite. However, by modelling the actual source in the interference pattern of the infinite substrate we were able to determine the strip positions with respect to the source and the required strip curvature. The large $10\lambda_o$ x $10\lambda_o$ hologram was fabricated and the measured results were presented in Section 3.4. The fabricated hologram showed a 1dB improvement in gain and good return loss performance.

Chapter 4 - General Conclusions and Suggested Future Work

4.1 General Conclusions

The effectiveness of using more accurate interference patterns to synthesize binary holograms has been investigated. Further insights into the antenna operation were achieved through detailed examinations of the influence of the substrate and the use of a realistic source on the interference pattern and antenna. The new interference pattern provided the knowledge of the strip positions with respect to the feed, and the required strip curvature, for the printed-Yagi source.

In the 2-D analyses, it was possible to study the effect of the finite length substrate on the interference pattern along with the realistic feed horn source. The finite substrate causes a double-minima effect in the interference pattern for sources of any complexity, and is dependent on the substrate thickness. The effect was exploited through varying the sources' amplitude in the computation of the interference pattern to achieve high directivity. Applying this approach to synthesize the double-sided hologram resulted in significant improvement compared to the free-space double-sided hologram. The effect of the strip width was studied and increasing the strip width will decrease the hologram directivity as it will increase the antenna leakage rate. The initial strip width is the optimal width for the substrates considered in this thesis. Additionally, the holographic interpretation was also confirmed through the realization of highly directive holograms that used a grounded dielectric substrate to suppress the bottom beam.

Although the interference pattern required to design the large $10\lambda_o$ x $10\lambda_o$ 3-D hologram could not be computed in the presence of the large finite substrate, investigations of the interference pattern with the small $4\lambda_o$ x $4\lambda_o$ 3-D finite substrate demonstrated that the holographic interpretation from the 2-D study could be carried over to the 3-D study. The

small 3-D hologram produced a broadside beam even though it consisted of noncircular strips that were located at random positions. Another small $4\lambda_o$ x $4\lambda_o$ 3-D hologram realized from the interference pattern determined in the presence of the infinite substrate also showed similar gain in the broadside direction. Therefore the large interference pattern required to design the large ($10\lambda_o$ x $10\lambda_o$) 3-D hologram was approximated with the interference pattern of the infinite substrate due to memory limitation on computing the interference pattern of the large finite substrate. Experimental validation confirmed the design procedure and showed a 1dB improvement compared to the printed-dipole-fed hologram. Additionally, the printed-Yagi-fed hologram has more leftover power which will enable the use of larger holograms to increase the gain.

4.2 Suggested Future Work

Due to the asymmetry in the feed, the fabricated single-sided hologram had asymmetry in the main beams which caused the best gain to be off the designed frequency. Therefore the effect of the asymmetric feed will need be considered in future designs of the double-sided hologram. In addition to the effect of the asymmetric feed, the printed-feed will need to be modified to account for the thick substrate used in the double-sided hologram before we apply the design procedure. Another way to eliminate the undesired beam is to use the grounded substrate hologram that was demonstrated in the 2-D study. We can still use the interference pattern of the infinite substrate approximation if we use a printed-feed that has both dipole arms on the same plane [25] so that the other side of the substrate will only consist of the ground plane. Using this approach will enable the use of IE3D to model the infinite ground plane and infinite substrate. The influence of the plane wave on an infinite grounded dielectric slab can be determined using the same transmission line model where the load is now a short-circuited load, and is similar to the design procedure in the 2-D study. The advantage with this hologram is its ability to suppress the undesired beam over all frequency instead of over a range of frequencies as in the double-sided hologram.

If it is possible with other 3-D electromagnetic modelling tools, the interference pattern of the finite 3-D substrate should be investigated to include the reflections caused by the finite

3-D substrate in the interference pattern. Further gain could be achieved as we have observed in the 2-D study where by manipulating the sources' amplitude we were able to place more strips on the substrate to increase the gain. This was also evident in the small ($4\lambda_o$ x $4\lambda_o$) 3-D antenna where there was a 0.8dB difference between the hologram synthesized from the interference pattern determined in the presence of the finite substrate compared to that using the infinite substrate. And the shape of the substrate could be studied to minimize the spillover loss of the feed's radiation.

Appendix A - Holograms Used in 2-D Study

Type of hologram	Configuration to compute the interference pattern	Strips placement of hologram
Case 1	Line source with plane wave in free-space.	Strips placed at single minima positions.
Free-space	Line source with plane wave in free-space.	Strips placed periodically at every λ_o.
Optimized free-space	Line source with plane wave in free-space.	Strip positions were optimized using strip positions of free-space hologram as initial starting point with a strip movement restriction of +/- 5mm ($\lambda_o/2$).
Case 2	Line source with plane wave in the presence of finite length dielectric substrate.	Strips placed at single minima positions.
Case 3a	Line source and horn walls with plane wave in the presence of finite length dielectric substrate.	Strips placed at only higher minima positions in double minima.
Case 3b	Line source and horn walls with plane wave in the presence of finite length dielectric substrate.	Strips placed at only lower minima positions in double minima.
Case 3 (sometimes referred to as new hologram)	Line source and horn walls with plane wave in the presence of finite length dielectric substrate.	Strips placed at all double minima positions. Equal strip width of 0.254mm for all strips.

Optimized case 3 (sometimes referred to as optimized new hologram)	Line source and horn walls with plane wave in the presence of finite length dielectric substrate.	Strip positions were optimized using strip positions of case 3 hologram as initial starting point with a strip movement restriction of +/- 2mm ($2\lambda_o/10$).
Case 3d	Line source and horn walls with plane wave in the presence of finite length dielectric substrate.	Strips placed at all double minima positions. Strips at higher minima used a strip width of 0.254mm, and strips at lower minima used a strip width of 0.508mm.
Free-space double-sided	Line source with plane wave in free-space.	Strips placed periodically at every λ_o on top dielectric surface. Second set of strips were placed on bottom dielectric surface using the same strip spacings but shifted a quarter-wavelength relative to the top strips.
Double-sided	Line source and horn walls with plane wave in the presence of finite length dielectric substrate with a thickness of a quarter-wavelength.	Strips placed at all double minima positions on top dielectric surface. Second set of strips were placed on bottom dielectric surface using the same strip spacings but shifted a quarter-wavelength relative to the top strips.
Free-space grounded slab	Line source with plane wave in free-space.	Strips placed periodically at every λ_o on top dielectric surface.
New grounded slab	Line source and horn walls with plane wave in the presence of finite length grounded-dielectric substrate.	Strips placed at all double minima positions.

Appendix B - Procedure to Compute 2-D Directivity from an Aperture Field

This appendix will briefly describe the plane wave angular spectrum interpretation used to compute the far-field of a 2-D uniform aperture distribution. Then, the 2-D directivity can be computed using $D(\phi) = \frac{|E_z(\phi)|^2}{\frac{1}{2\pi}\int_0^{2\pi}|E_z(\phi)|^2\, d\phi}$, since $D_{\text{uniform}} = \frac{4\pi \ \ Area}{\lambda_o^2}$ only applies to the aperture area of 3-D antennas [13].

An arbitrary 2-D field can be represented as a set of plane waves travelling at different angles, which is analogous to representing an arbitrary temporal signal by a set of sinusoids of different frequencies of infinite duration [12]. For our case, the field to be transformed to the far-zone will be taken over a planar aperture, and will be assumed to be non-zero over a finite central portion of the aperture ($a \le y \le b$) and truncated to be zero elsewhere. The field over the aperture, $E_z^{ap}(y)$, can be expressed as a set of plane waves traveling at different angles by

$$E_z^{ap}(y) = \int_{-\infty}^{\infty} F(\sin\phi) \ \ e^{-jk\sin\phi y} \ \ d\sin\phi \tag{B.1}$$

where the angular spectrum is

$$F(\sin\phi) = \int_{-\infty}^{\infty} E_z^{ap}(y) \ \ e^{jk\sin\phi y} \ \ dy \tag{B.2}$$

The far-field is then

$$E_z(\rho,\phi) = \sqrt{\frac{\lambda}{\rho}} \ \ F(\sin\phi) \ \ \cos\phi \ \ e^{-j(k\rho-\pi/4)} \tag{B.3}$$

and can be written in the form $E_z(\rho,\phi) = \frac{E_z(\phi)}{\sqrt{\rho}} e^{-jk\rho}$, where

$$E_z(\phi) = \frac{e^{j\pi/4}}{\sqrt{\lambda^3}} \cos\phi \int_a^b E_z^{ap}(y)\ e^{jk\sin\phi y}\ dy \tag{B.4}$$

is then used to in the computation of the directivity.

To verify the procedure we used the total field above the substrate region as the aperture field, transformed it to the far-field, computed its directivity and compared it with the exact 2-D directivity from the 2-D moment method model. Figure A.1 shows this comparison of the case 3 holographic antenna from section 2.1.4. The procedure showed good agreement with the exact 2-D directivity over the region of interest. It cannot capture the full 2-D directivity such as the endfire lobe because the procedure only gives valid field values in the half-space above the planar aperture field, in other words the angular region $0^o \le \phi \le 180^o$ where ϕ is defined in Figure 2.1.

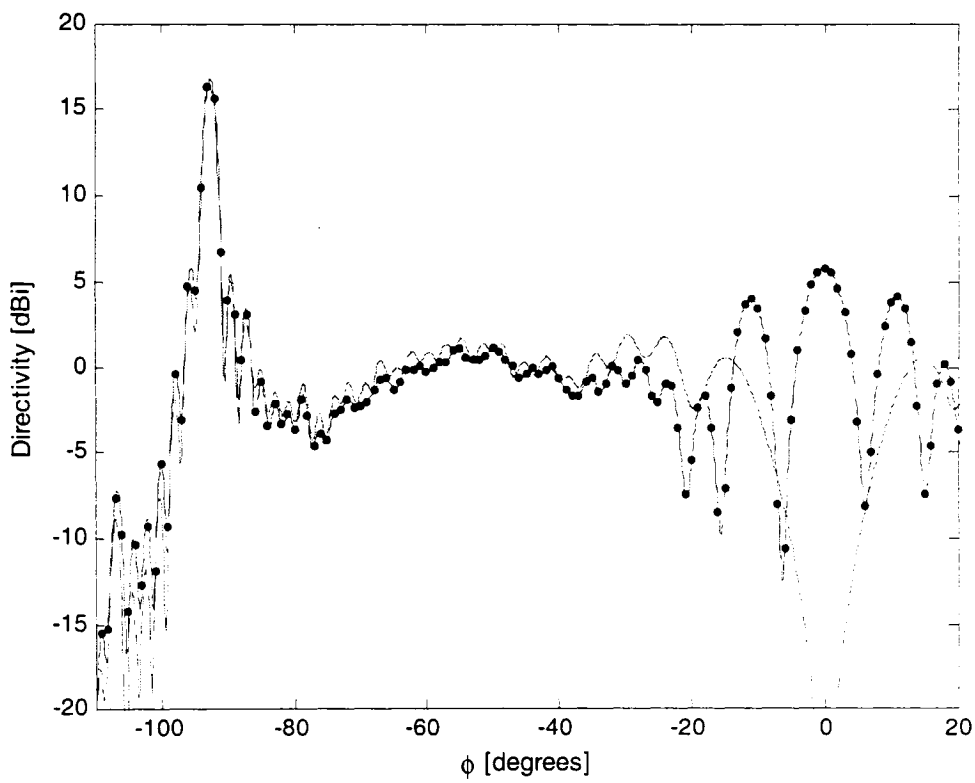

Figure B.1 - Directivity of case 3 with L = 280mm: Exact directivity from 2-D moment method model (— – • — • — • —), Directivity from near-field to far-field transform procedure (————————), f=30GHz

To compute the ideal 2-D directivity of a uniformly distributed aperture we set the field to be constant in the aperture region, zero outside the aperture, and compute the directivity using the described procedure.

Appendix C - Dimensions of the Fabricated Hologram Fed by a Printed-Yagi Source

The geometry and dimensions of the antenna are described in Figures C.1-C.4, with all dimensions in mm. Figure C.3 is a detailed view of the top dipole arm in the printed-Yagi where a quarter-wave transformer was used to connect to the dipole and the microstrip line. The fourteen circular strips have the same centre coordinate located at the centre of the dipole, as shown in Figure C.3. The radius of the strips is listed in Table C.1. The substrate thickness is 0.508mm, and $\varepsilon_r = 3.38$.

Table C.1 - Radius of hologram strips

Strip number	Radius [mm]
1	14.6
2	24
3	33.4
4	42.8
5	52.2
6	61.5
7	70.9
8	80.3
9	89.7
10	99.1
11	108.5
12	117.9
13	127.3
14	136.7

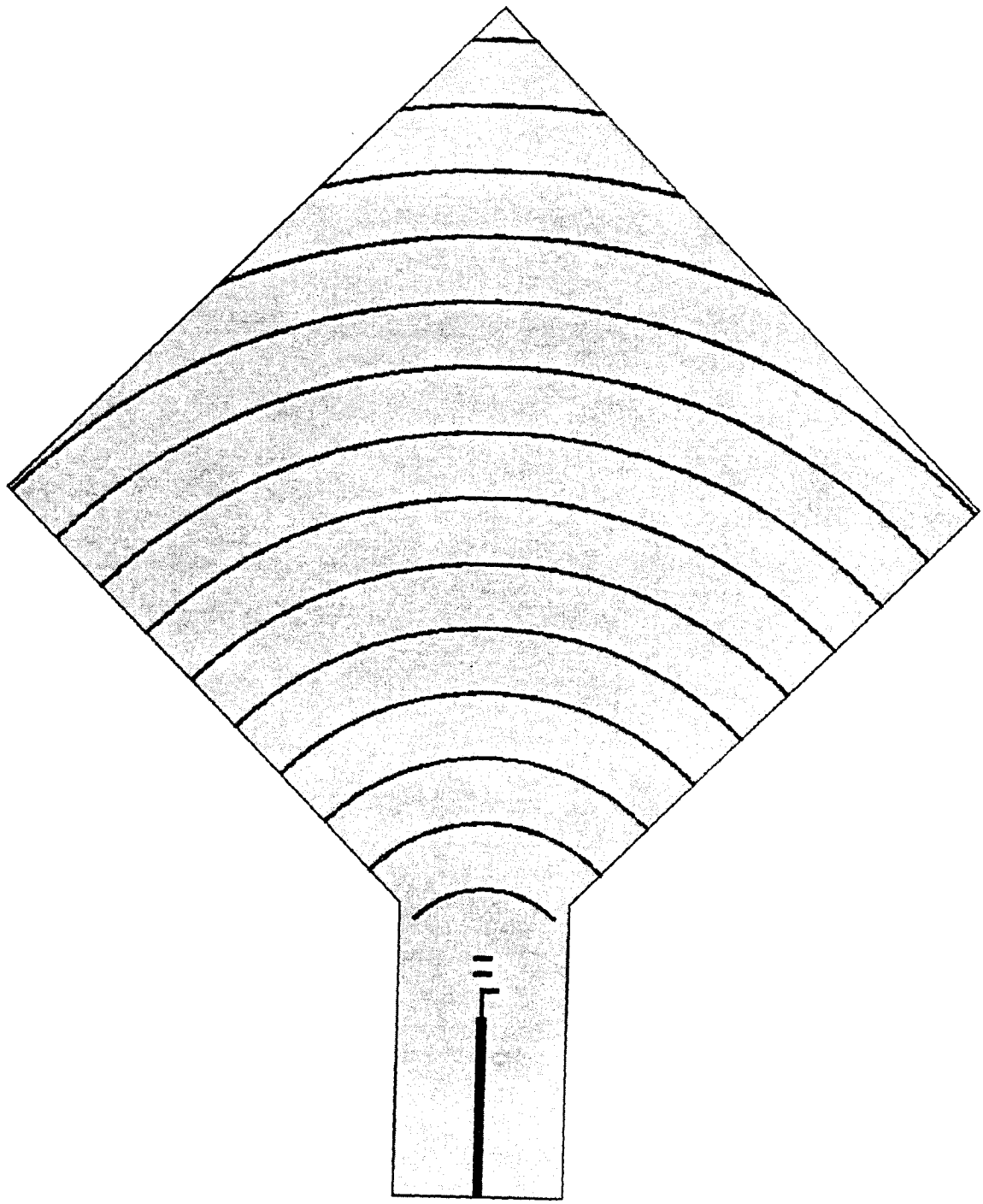

Figure C.1 - Experimental $10\lambda_o \times 10\lambda_o$ holographic antenna fed by printed-Yagi source

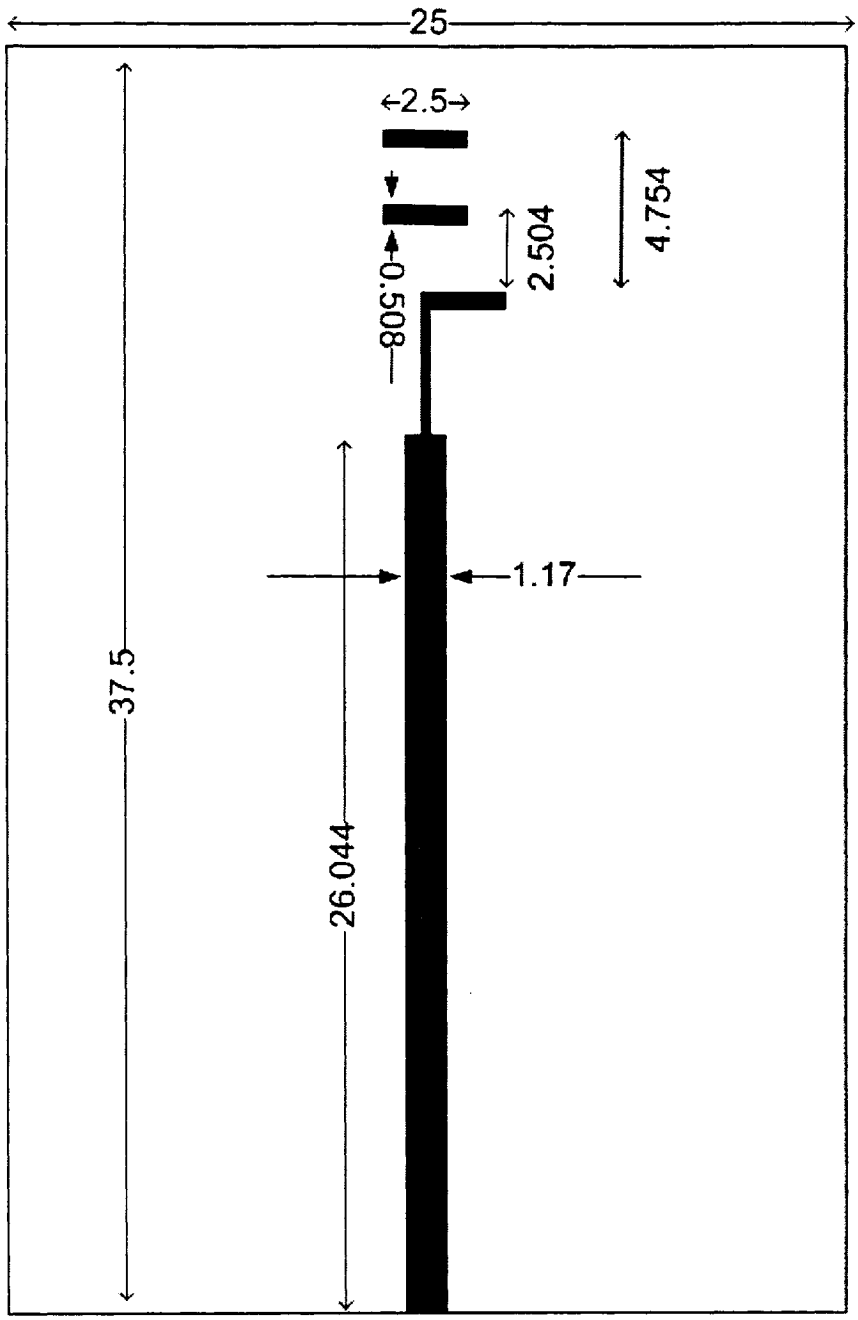

Figure C.2 - Top side of printed-Yagi source

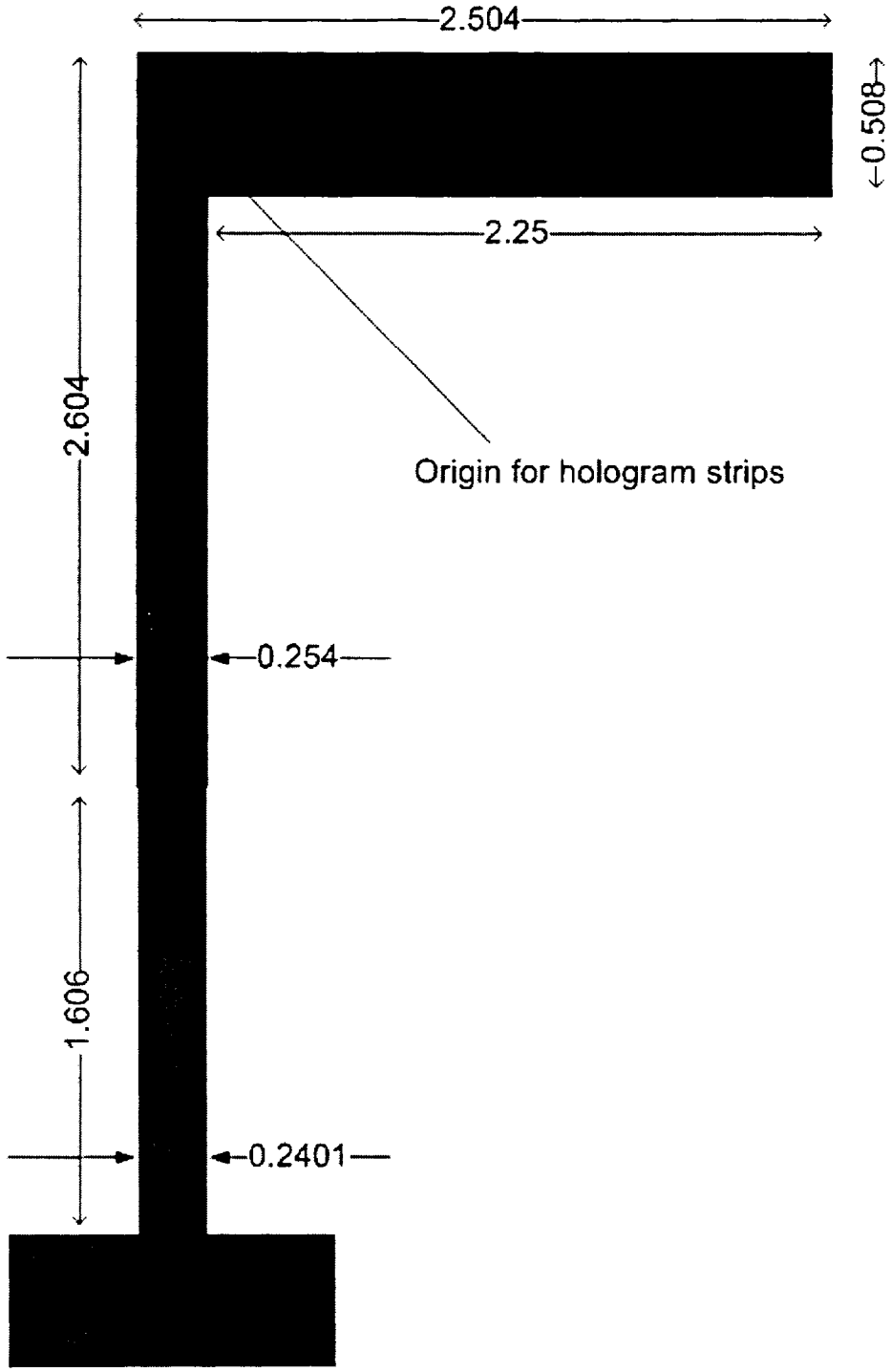

Figure C.3 - Detailed view of the top side of printed-Yagi source

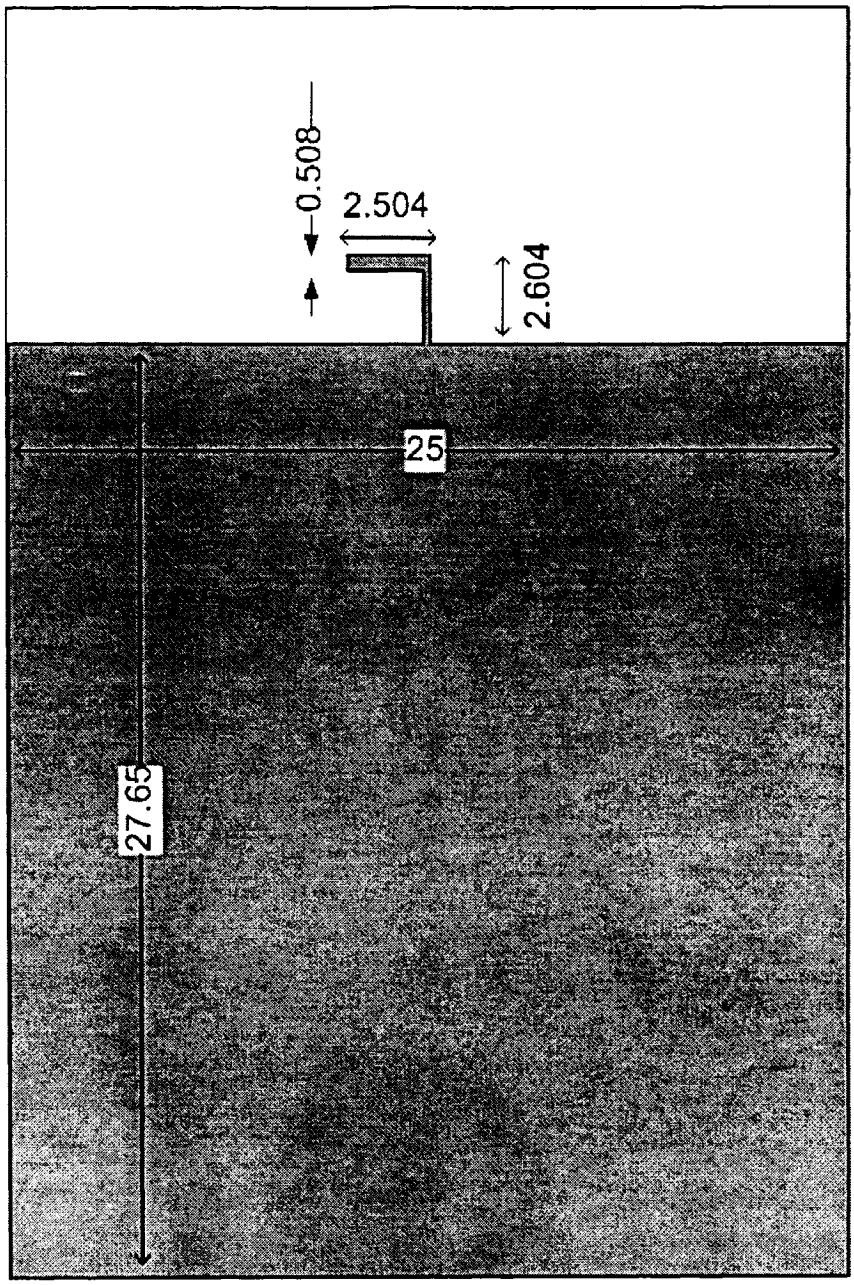

Figure C.4 - Bottom side of printed-Yagi source

References

[1] J.W. Goodman, *Introduction to Fourier optics*, New York: McGraw-Hill, 1996

[2] K. Iizuka, M. Mizusawa, S. Urasaki, and H. Ushigome, "Volume-type holographic antenna", *IEEE Transactions on Antennas and Propagation*, Volume 23, Issue 6, Nov 1975, pp. 807 - 810

[3] K. Levis, "Ka-Band Holographic Antennas", *M.A. Sc thesis*, University of Ottawa, Ottawa, ON, Canada, 1999

[4] K. Levis, A. Ittipiboon, A. Petosa, L. Roy, and P. Berini, "Ka-band dipole holographic antennas", *IEE Proceedings - Microwaves, Antennas and Propagation*, Volume 148, Issue 2, April 2001, pp. 129 - 132

[5] P. Sooriyadevan, "The Electromagnetic Modelling and Optimization of Planar Holographic Antennas", *M.A. Sc thesis*, University of Ottawa, Ottawa, ON, Canada, 2004

[6] S.R. Thingvold, A. Ittipiboon, A. Sebak, and A. Petosa, "Holographic antenna efficiency", *IEEE Antennas and Propagation Society International Symposium 2003*, Volume 3, pp. 721 - 724

[7] A. Petosa, S. Thirakoune, K. Levis, and A. Ittipiboon, "Microwave holographic antenna with integrated printed dipole feed", *Electronics Letters*, Volume 40, Issue 19, Sept. 2004, pp. 1162 - 1163

[8] M. ElSherbiny, A.E. Fathy, A. Rosen, G. Ayers, and S.M. Perlow, "Holographic antenna concept, analysis, and parameters", *IEEE Transactions on Antennas and Propagation*,

Volume 52, Issue 3, March 2004, pp. 830 - 839

[9] D. Sievenpiper, J. Colburn, B. Fong, J. Ottusch and J. Visher, "Holographic artificial impedance surfaces for conformal antennas", presented at *IEEE Antennas and Propagation Society International Symposium 2005*, Washington, D.C., U.S.A., 2005

[10] X. Yuan, R.F. Harrington, and S.S. Lee, "Electromagnetic scattering by a dielectric cylinder partially covered by conductors", *Journal of Electromagnetic Waves and Applications*, Volume 2, Number 1, 1987, pp. 21 - 44

[11] D.A. McNamara, "The Moment Method in Engineering Electromagnetics", ELG7100D Course Notes, University of Ottawa, 2004

[12] R. H. Clarke and J. Brown, *Diffraction Theory and Antennas*, Chichester, England: E. Horwood, 1980

[13] A. Petosa, "Antenna and Arrays", ELEC5607 Course Notes, Carleton University, 2003

[14] G. Saxby, *Manual of Practical Holography*, Oxford, England: Focal Press, 1991

[15] D.M. Pozar, *Microwave Engineering*, New York: Wiley, 1998

[16] R.S. Elliott, *Antenna Theory and Design*, Hoboken, N.J.: Wiley, 2003

[17] G. Zheng, A.A. Kishk, A.W. Glisson, and A.B. Yakovlev, "Simplified feed for modified printed Yagi antenna", *Electronics Letters*, Volume 40, Issue 8, April 2004, pp. 464 - 466

[18] C. Balanis, *Antenna Theory: Analysis and Design*, New York: Wiley, 1997

[19] F.T. Ulaby, *Fundamentals of Applied Electromagnetics*, Upper Saddle River, N.J: Prentice Hall, 2001

[20] B. R. Brown and A. W. Lohmann, "Computer generated holograms," in *The Engineering uses of holography,* E. R. Robertson and J. M. Harvey, Cambridge, England: University Press, 1970, pp. 77 - 92

[21] E. Levine, G.M. Malamud, S. Shtrikman, and D. Treves, " A study of microstrip array antennas with the feed network", IEEE Transactions on Antennas and Propagation, Volume 37, Issue 4, April 1989, pp. 426 - 433

[22] HFSS (High-Frequency Structure Simulator) is a product of Ansoft Inc. located in Pittsburgh, Pennsylvania, USA, www.ansoft.com. It employs a three-dimensional vector finite element formulation.

[23] IE3D is a product of Zeland Inc. located in Fremont, California, USA, www.zeland.com. It employs a moment method formulation that allows infinitely large dielectric layers.

[24] EMPIRE is a product of IMST Inc. located in Kamp-Lintfort, Germany, www.imst.com. It employs a three-dimensional finite-difference time-domain formulation.

[25] Y. Qian, W.R. Deal, N. Kaneda, and T. Itoh, "Microstrip-fed quasi-Yagi antenna with broadband characteristics", *Electronics Letters*, Volume 34, Issue 23, Nov. 1998, pp. 2194 – 2196

[26] P. Kovesi (pk@cs.uwa.edu.au), R. Gaddi (gaddi@rice.edu), MATLAB code on "2D Frequency Domain Filtering and the 2D DFT", http://www.owlnet.rice.edu/~elec301/Projects01/image_filt/matlab.html

[27] S. Koptenko, MATLAB code on "Local min, max, nearest neighbour", http://www.mathworks.com/matlabcentral/fileexchange/loadFile.do?objectId=3170&objectType=file